PREPARING FOR NEXT-GENERATION GALAXY SURVEYS

by

Rongpu Zhou

BS, University of Electronic Science and Technology of China, 2013

Submitted to the Graduate Faculty of

the Dietrich School of Arts and Sciences in partial fulfillment

of the requirements for the degree of

Doctor of Philosophy

University of Pittsburgh

2019

UNIVERSITY OF PITTSBURGH

DIETRICH SCHOOL OF ARTS AND SCIENCES

This dissertation was presented

by

Rongpu Zhou

It was defended on

July 2nd 2019

and approved by

Dr. Jeffrey A. Newman, Department of Physics and Astronomy, University of Pittsburgh

Dr. Ayres Freitas, Department of Physics and Astronomy, University of Pittsburgh

Dr. Rachel Mandelbaum, Department of Physics, Carnegie Mellon University

Dr. Michael Wood-Vasey, Department of Physics and Astronomy, University of Pittsburgh

Dr. Andrew R. Zentner, Department of Physics and Astronomy, University of Pittsburgh

Dissertation Director: Dr. Jeffrey A. Newman, Department of Physics and Astronomy,

University of Pittsburgh

PREPARING FOR NEXT-GENERATION GALAXY SURVEYS

Rongpu Zhou, PhD

University of Pittsburgh, 2019

In the 1920s, Edwin Hubble discovered that the Milky Way is merely one of countless galaxies in the Universe, and the relative velocities of these galaxies indicate that the Universe is expanding. Developments in the ensuing decades have solidly established galaxy surveys as a crucial probe of cosmology. In this thesis, I describe my work related to preparations for the next generation of galaxy surveys.

In the first part of the thesis, we present catalogs of calibrated photometry and spectroscopic redshifts in the Extended Groth Strip, intended for studies of photometric redshifts (photo-z's). The data includes *ugriz* photometry from CFHTLS and Y-band photometry from the Subaru Suprime camera, as well as spectroscopic redshifts from the DEEP2, DEEP3 and 3D-HST surveys. These catalogs incorporate corrections to produce effectively matched-aperture photometry across all bands. We test this catalog with a simple machine learning-based photometric redshift algorithm based upon Random Forest regression, and find that the corrected aperture photometry leads to significant improvement in photo-z accuracy compared to the original SExtractor catalogs from CFHTLS and Subaru. The deep *ugrizY* photometry and spectroscopic redshifts are well-suited for empirical tests of photometric redshift algorithms for LSST.

In the second part of the thesis, we model the redshift-dependent clustering of a DESI-like LRG sample in the halo occupation distribution (HOD) framework using photometric redshifts (photo-z's). The LRG sample contains 2.7 million objects over a 5655 square degree area and spans the redshift range of $0.4 < z < 0.9$. Highly accurate photo-z's are computed using DECam and WISE photometry. We measure the galaxy clustering with the projected

correlation function, rather than the angular correlation function, to make optimal use of the photo-z's. We find that there is little evolution in the host halo properties except at the high-redshift end. The bias evolution is mostly consistent with the simple prescription of constant clustering amplitude. We discuss a number of methodological improvements developed as part of this work and how they can be applied to future surveys.

TABLE OF CONTENTS

LIST OF TABLES

LIST OF FIGURES

LIST OF EQUATIONS

1   INTRODUCTION

The past century has seen tremendous advances in our knowledge of the Universe. Einstein's general theory of relativity has been extremely successful in describing astrophysical systems from the Solar System to black holes. Equally successful is the Standard Model of physics that describes the fundamental particles and their interactions. Combined with observational evidence, we are now able to describe much of history of the Universe, and make the remarkable quantitative connection between the epoch of recombination, when the Universe was less than a million years old as observed through the cosmic microwave background (CMB), to the Universe billions of years later as observed in the light of galaxies. However, our gains in knowledge have only revealed that there are even larger pieces missing — the current model of cosmology has two components that do not fit into our current knowledge of physics: dark matter and dark energy.

Hypothesized as early as the 1930s by Fritz Zwicky, dark matter was first invoked to explain the velocity dispersions of galaxy clusters and later to explain the rotation curves of spiral galaxies, and it has since become a necessary ingredient for explaining other observational phenomena, including the power spectrum of CMB temperature fluctuations, galaxy clustering and gravitational lensing. From astronomical probes, we now know that dark matter is "cold" — nonrelativistic to allow for the formation of structures that we see today — and it constitutes roughly 85% of all matter. Yet the nature of dark matter remains elusive. Searches are ongoing for candidates of the dark matter particle, such the weakly interacting massive particles (WIMPs). Collider experiments attempt to produce and detect dark matter particles. Direct detection experiments attempt to measure the signal from the collision between dark matter particles and baryonic matter. Indirect detection experiments attempt to observe the annihilation products of dark matter particles, e.g., by observing

gamma rays emitted from the Galactic center and Milky Way satellites. Astronomical surveys — observations of some (typically large) population of objects rather than a specific target — in the optical and near-infrared would in many ways complement the direct and indirect searches, e.g., with measurements of the density and relative velocity of local dark matter distribution, and with discoveries of satellite galaxies.

An even more mysterious component in the standard cosmological model is dark energy, evoked to explain the accelerated expansion of the late-time Universe. Through various cosmological probes such as Type Ia supernovae (which made the first convincing discovery), CMB and the large-scale structure, we now know that dark energy contributes roughly 70% of the Universe's energy density today. Nevertheless, much of its phenomenology, e.g., whether it is a cosmological constant or some time-varying energy density, remains unknown.

As better observational instruments are developed and higher statistical constraining power is achieved, we are on track to making more accurate measurements to reveal the nature of these mysterious components. One powerful probe in cosmology is the study of the large-scale structure of matter that is traced by galaxies. In this thesis, I will describe my work related to two of the leading next-generation galaxy surveys which will study cosmology using this large-scale structure: the Large Synoptic Survey Telescope (LSST) and the Dark Energy Spectroscopic Instrument (DESI). There is a wide range of sciences that the two instruments will be able to study. We present below a brief summary of some of the aspects that are relevant to this thesis.

1.1   PHOTOMETRIC REDSHIFTS IN THE ERA OF LSST

Imaging observations form the basis of astronomy. Astronomical objects are catalogued and their angular position, brightness and shape measured based on imaging data, thus enabling further imaging or spectroscopic observations. The last two decades has seen a number of large imaging surveys in the optical and near-infrared that either map a large fraction of the sky, such as SDSS (York, 2000), Pan-STARRS (Chambers et al., 2016), and DES (Collaboration et al., 2016), or achieves great imaging depth, such as CFHTLS (Hudelot

et al., 2012) and HSC (Miyazaki et al., 2012). As the most powerful next-generation ground-based imaging telescope, LSST will obtain unprecedented depth and coverage of the optical and near-infrared sky.

The imaging data from LSST will enable precise measurements on the growth of structure and the distance-redshift relation using several cosmological probes which will provide vastly improved cosmological constraints. In fact, the current generation of imaging surveys has already been able measure certain cosmological parameters with error bars comparable to the Planck CMB measurements. One such example is the first year constraints from the Dark Energy Survey (Collaboration et al., 2018a), achieved through the joint modeling of different growth of structure measurements, namely measurements of galaxy clustering and weak gravitational lensing. Constraints on the distance-redshift relation, which is directly affected by dark energy, will be provided by Type Ia supernova measurements as well as photometric baryon acoustic oscillation (BAO) measurements (spectroscopic measurement of the latter is described in section 1.2).

All of the aforementioned cosmological probes require galaxy redshifts in their analysis. The redshift measures the apparent Doppler shift of galaxies which is (mostly) due to the expansion of the Universe, and it is defined as

$$z \equiv \frac{\lambda_{obs} - \lambda_{emit}}{\lambda_{emit}}. \tag{1.1}$$

It is convenient to also define two other quantities: the scale factor a which measures the relative expansion of the Universe (with its current value set to $a = 1$ it is related to the redshift by $a = 1/(1 + z)$); the other quantity is the comoving distance χ which measures the distance between two points on a grid that expands with the Universe and therefore it remains constant. The physical distance is the product of the scale factor and the comoving distance.

The redshift is directly related to the comoving distance through the distance-redshift relation:

$$\chi(z) = c \int_0^z \frac{\mathrm{d}z'}{H(z')}, \tag{1.2}$$

where c is the speed of light and H is the expansion rate (defined below). Therefore, the redshift not only provides distance information if one assumes a specific mapping between

distance and redshift, but it can also be used to measure the distance-redshift relation, which is specified by the cosmological model, if we have measurements of absolute or even relative distances (e.g., by measuring the brightness of Type Ia supernovae).

In General Relativity, the expansion rate obeys

$$H^2(a) \equiv \left(\frac{\dot{a}}{a}\right)^2 = \frac{8\pi G\rho}{3} - \frac{k}{a^2} + \frac{\Lambda}{3}, \tag{1.3}$$

where $a = 1/(1 + z)$ is the scale factor, ρ is the energy density, k is the curvature and Λ is the cosmological constant. In a flat Universe with a cosmological constant as only the dark energy component, the expansion rate is given by

$$H(z) = H_0 \left[\Omega_\Lambda + \Omega_{\mathrm{m}}(1 + z)^3 + \Omega_{\mathrm{r}}(1 + z)^4\right]^{1/2}, \tag{1.4}$$

where Ω_Λ, Ω_{m} and Ω_{r} are the present-day density parameters of dark energy, matter and radiation, respectively. Of course dark energy does not have to be a cosmological constant; a more general form of dark energy is characterized by the equation of state

$$w = P/\rho, \tag{1.5}$$

where P is the pressure. For a cosmological constant we have $w = -1$. For a non-constant equation of state, the energy density evolves as

$$\rho(a) \propto \exp\left[3 \int_a^1 \frac{da'}{a'} \left(1 + w\left(a'\right)\right)\right]. \tag{1.6}$$

The Dark Energy Task Force (DETF, Albrecht et al. 2006) adopted a simple parametrization of $w(a)$ for the convenience of comparing the constraining power of different surveys

$$w(a) = w_0 + (1 - a)w_a, \tag{1.7}$$

and defined the figure of merit (FoM) as a measure of the combined precision on w_0 and w_a — a larger FoM corresponds to smaller uncertainties on w_0 and w_a. It is expected that LSST will achieve a FoM of > 500 by combining its cosmological probes; this is about 10 times that of the previous generation ("Stage-II") surveys.

The redshift is therefore a crucial observable in cosmology. However, imaging data,

which is two dimensional in nature, can only provide redshift estimates using the multi-band photometry, which is effectively a very low-resolution spectroscopy (only 6 passbands/data points for LSST). Although the resulting redshift estimates, known as photometric redshifts (or photo-z's), are less accurate than redshifts from spectroscopy, the sheer size of the photometric sample and their much lower cost per object than spectroscopic redshifts compensates for this inaccuracy in many applications (especially those that rely on imaging data such as lensing measurements). Cosmological analyses with photometric data are typically performed by measuring the angular correlation of galaxy properties (e.g., position or shape) in bins of photo-z's so that the result is less sensitive to individual photo-z uncertainties (although we argue in chapter 3 that, if accurate photo-z's are available, galaxy clustering measurements are best performed in photometric redshift space).

LSST is designed with photometric redshifts in mind: the overall system throughput (i.e., sensitivity as a function of wavelength) and the six filters ($ugrizy$) allow for accurate redshift estimates of red galaxies out to $z < 1.4$ by locating the 4000Å break (at z=1.4 the break transitions into the y band; at that point it becomes poorly constrained). The large sample size and more accurate photo-z's from LSST will not only improve current measurements but also enable studies in areas that previously relied solely on spectroscopic redshifts, such as the galaxy-halo connection. Nevertheless, the smaller sample variance and higher photometric signal-to-noise ratio (S/N) in the era of LSST would require better photo-z algorithms and calibration methods in order to realize the full potential of the dataset.

To test photo-z algorithms for LSST, data with photometry in LSST-like filters and accurate redshifts is needed. Such data can be either from real observations or simulations. Simulations have the advantage of generating large catalogs with arbitrarily deep photometry, but they have yet to be able to produce realistic galaxy colors. Therefore, definitive tests of photo-z algorithms would require observed galaxy photometry. Chapter 2 describes a new observational dataset that we have developed to serve as a testbed for photo-z algorithms specifically for LSST.

1.2 DARK ENERGY CONSTRAINTS FROM DESI

Due to the aforementioned limitations of imaging surveys, more accurate maps of the large-scale structure require spectroscopic observations. Examples of large spectroscopic surveys in the last two decades are: 2dFGS (Colless et al., 2003), SDSS (York, 2000), DEEP2 (Newman et al., 2013), etc. Data from spectroscopic observations have numerous uses, but one particular measurement that spectroscopic surveys are best fitted to perform is that of the BAO signature.

The BAO consisted of acoustic waves in the primordial plasma that were frozen at recombination. It is perhaps useful to understand BAO in an idealized picture: imagine there is a single point of overdensity in the primordial plasma of the early Universe; the overdensity expanded due to the pressure in the plasma, and the expanding sound wave froze at the time of recombination, forming a spherical shell of baryon overdensity. Of course, the pattern from single points of overdensities does not exists; instead there is a continuous distribution of density fluctuations which convolves with that pattern, leading to a statistical tendency to find excess density about 150 Mpc from the original overdensity. This characteristic scale, i.e., the acoustic scale, is the distance that the sound waves traveled before recombination, and it is given by

$$r_s = \int_0^{t_*} \frac{c_s dt}{a(t)},$$ (1.8)

where c_s is the sound speed, which is is simply related to the baryon density ρ_b and radiation density ρ_γ by

$$c_s = \frac{c}{\sqrt{3\left(1 + \frac{3\rho_b}{4\rho_\gamma}\right)}}.$$ (1.9)

After recombination, the acoustic imprint expands with the Universe, and therefore it is fixed in comoving coordinates. The imprint can be detected both from the CMB and from the large-scale structure of the late-time Universe. While the imprint on the CMB is only seen at one point in time ($z \sim 1100$), the imprint on the large-scale structure of matter traced by galaxies can be measured as a function of time. Therefore the BAO signature measured from galaxies serves as a standard ruler across cosmic time, enabling us to measure the distance-redshift relation (equation 1.2) and the expansion history of the Universe which is

now dominated by dark energy.

It is worth noting that the acoustic pattern in the CMB is purely the result of baryon over/under-densities at the time of recombination, and therefore we are looking at cross-sections of the spherical shells; on the other hand, the dark matter does not participate in the wave propagation and remains concentrated at the original point of overdensity, and eventually the gravitational attraction causes the two components to mix, resulting in over-densities both at the site of the original overdensity and at the distance of the acoustic scale. For this reason, the first detections of the BAO signature in galaxies (e.g., Eisenstein et al. 2005) at the expected acoustic scale of 150 Mpc not only provided a standard ruler for cosmology, but the detection itself is direct evidence that dark matter exists.

Compared with other probes of the distance-redshift relation, BAO is a very robust measurement with relatively few systematics uncertainties for the following reasons: 1) simple physics is involved in calculating the acoustic scale; 2) the acoustic scale is derived from the peak location in the correlation function, and it is insensitive to the "broadband" clustering signal which is more prone to systematics; 3) the BAO peak is at a relatively large scale and therefore insensitive to non-linear effects; 4) it relies on angular positions, which are relatively simple to measure, on scales much larger than any systematics in those measurements, and on redshifts, which in spectroscopic samples have few systematics on these scales.

Building on the success of previous cosmological redshift surveys (SDSS Tegmark et al. 2006, 2dGRS Cole et al. 2005, BOSS Alam et al. 2017, WiggleZ Parkinson et al. 2012, etc.), the Dark Energy Spectroscopic Instrument will perform the most ambitious galaxy redshift survey to date which will start in 2020. One of the main science goals of DESI is to measure the apparent scale of the BAO as a function of redshift, by observing galaxies to $z = 1.7$ and quasars to $z = 3.5$ over 14,000 square degrees of the sky, and provide accurate (sub-percent- and percent-level) distance measurements. DESI is expected to achieve a DETF FoM of 133 from galaxy BAO measurements alone, which is more than a factor of 3 better than FoM of all previous generation (Stage-III) galaxy BAO measurements combined, and there can potentially be another factor of 5 improvement by combining with measurements of Ly-α BAO and broadband power spectrum to small scales if the small-scale clustering can be accurately modeled.

Unlike in imaging surveys where everything in the instrument's field of view is observed, in a spectroscopic survey like DESI only a finite number — set by the number of available fibers — of objects can be observed in each exposure, and the spectroscopic targets need to be selected beforehand. It is obviously desirable to select targets that can maximize the BAO S/N, and for this purpose the targets need to be well understood. In particular, by modeling the galaxy-(dark matter) halo connection, one can directly link small-scale clustering measurements to large-scale clustering, and estimate the samples's large-scale structure bias — the relative clustering amplitude compared to the underlying matter distribution — which is directly related to the efficiency of BAO measurements.

One important class of targets in DESI is the luminous red galaxies (LRGs), which are in the redshift range of $0.4 < z < 1.0$. Although there have been studies of lower redshift or lower density LRG samples from previous spectroscopic surveys, the clustering properties of DESI LRGs have yet to be examined. Chapter 3 describes the small-scale clustering analysis of the DESI-like LRG sample with an alternative approach that relies solely on photometric data. With the knowledge of the galaxies' clustering properties, one can produce accurate mock galaxies that can be used in DESI analyses, e.g., for estimating the covariances between clustering measurements at different scales. Although it is not yet feasible to produce large mock galaxy catalogs from physical models such as hydrodynamical simulations, empirical models such as the halo occupation distribution model, which we adopted for our study, can accurately match the small-scale clustering measurements and provide estimates of the host halo mass distribution, which is directly related to the sample's large-scale clustering properties and important for BAO analysis.

Although this is outside the scope this thesis, it is worth mentioning that the next generation of galaxy surveys will enable investigations in cosmology and particle physics beyond dark matter and dark energy. Here we list three important examples.

It is believed that the primordial perturbations that seeded the structure formation in the Universe are the result of inflation — a brief period of exponential expansion in the early Universe. This period of rapid expansion naturally produces the smooth and flat Universe that we observe. By measuring the broadband power spectrum with galaxy surveys, we can constrain the parameters of inflationary models. The simplest models of inflation

predict that the primordial density fluctuations are nearly Gaussian distributed. By measuring the galaxy clustering on very large scales, we can put constraints on the amount of primordial non-Gaussianity, and potentially could rule out many inflationary models (Dalal et al., 2008; Matarrese & Verde, 2008). DESI and LSST are expected to put constraints on non-Gaussianity comparable to, if not better than, CMB experiments (Font-Ribera et al., 2014; Carbone et al., 2008).

Another aspect that galaxy surveys are able to probe is the mass of neutrinos. Neutrino oscillation measurements provide constraints on the squared mass differences of the neutrino mass eigenstates, but the best constraints on the sum of neutrino masses are from cosmological observations. Massive neutrinos smooth out the large-scale structures, an effect that can be measured from weak lensing and clustering observations. Data from DESI and LSST will enable the measurement of the absolute mass scale for neutrinos (Font-Ribera et al., 2014; Kitching et al., 2008).

Last but not least, data from galaxy surveys enable tests of General Relativity. General Relativity predicts the growth rate of structure as a function of time. In particular, in GR the growth rate can be predicted directly from the expansion history. By measuring the growth rate through weak lensing and peculiar velocity measurements, we can potentially distinguish between GR and modified gravity theories (Reyes et al., 2010); these alternative gravity theories can potentially provide an alternative explanation for the accelerated expansion of the Universe (Dvali et al., 2000; Carroll et al., 2004).

2 PHOTOMETRIC REDSHIFT TESTBED FOR LSST

Note: Much of this chapter is taken from a paper that has recently been accepted by Monthly Notices of the Royal Astronomical Society. A preprint version of this paper is on arXiv at https://arxiv.org/abs/1903.08174. Many of people have contributed to this work, and they are: Michael C. Cooper, Jeffrey A. Newman, Matthew L. N. Ashby, James Aird, Christopher J. Conselice, Marc Davis, Aaron A. Dutton, S. M. Faber, Jerome J. Fang, G. G. Fazio, Puragra Guhathakurta, Dale Kocevski, David C. Koo, Kirpal Nandra, Andrew C. Phillips, David J. Rosario, Edward F. Schlafly, Jonathan R. Trump, Benjamin Weiner, Christopher N. A. Willmer, and Renbin Yan.

2.1 INTRODUCTION

The Large Synoptic Survey Telescope (LSST Science Collaboration et al., 2009; Ivezic et al., 2009) will rely on photometric redshifts to achieve many of its science goals. For ten years, LSST will survey the sky in six filters to a depth unprecedented over such a wide area. The resulting dataset should provide important clues to the nature of dark matter and dark energy, detailed information on the structure of the Milky Way, a census of near-earth objects in the Solar System, and a wealth of information on variable and transient phenomena. In this paper, we present catalogs with robust spectroscopic redshift measurements and well-calibrated photometry in the Extended Groth Strip (EGS) with filter coverage and depths similar to the LSST *ugrizy* system. The LSST Science Requirements Document[1] specifies that for galaxies with $i < 25$ the LSST data should be capable of delivering a root mean

---

[1] www.lsst.org/scientists/publications/science-requirements-document

10

square (RMS) error in redshift smaller than $0.02(1 + z)$ with a rate of $> 3\sigma$ outliers below 10%. The dataset we have assembled will be useful for assessing if current photometric redshift algorithms can meet these requirements, and for improving them if not.

A previous paper, Matthews et al. (2013), matched redshifts from the DEEP2 Galaxy Redshift Survey (Newman et al., 2013) to photometry from the Canada-France-Hawaii Telescope Legacy Survey (CFHTLS Hudelot et al. 2012) and the Sloan Digital Sky Survey (SDSS Gunn et al. 1998; Alam et al. 2015). This works builds on that effort by adding DEEP3 (Cooper et al., 2011, 2012) and 3D-HST (Brammer et al., 2012; Momcheva et al., 2016) redshifts and Y-band photometry, and using Pan-STARRS (Chambers et al., 2016; Magnier et al., 2016) instead of SDSS for photometric calibration. We also have developed a method for calculating corrected aperture photometry from the CFHTLS catalogs, and we perform tests with a simple photometric redshift algorithm to demonstrate the superiority of this photometry for measuring galaxy colors.

The structure of this paper is as follows. Section 2.2 describes the datasets that we used to produce the final catalogs. We use spectroscopic redshifts from the DEEP2 and DEEP3 surveys, as well as grism redshifts from 3D-HST. The photometry in the *ugriz* bands is from CFHTLS. Additionally, Y-band imaging was obtained from SuprimeCam at the Subaru telescope (Miyazaki et al., 2002); photometry based on these images was derived using SExtractor (Bertin & Arnouts, 1996). In section 2.3 we describe the methods used to bring the CFHTLS, Subaru Y-band, and Pan-STARRS1 catalogs to a common astrometric system, based on those employed by Matthews et al. (2013). We describe our photometric zero-point calibration methods in section 2.4 and the techniques used to produce corrected aperture photometry in section 2.5. In section 2.6 we describe the resulting matched catalogs, which are being released in concert with this paper. In section 2.7 we present tests of these catalogs using photometric redshifts measured via Random Forest regression. We provide a summary in section 2.8.

2.2   DATASETS

In this section, we describe the spectroscopic and imaging datasets used to construct the catalogs presented in this paper.

2.2.1   Spectroscopy

The first spectroscopic sample included in our catalogs comes from the DEEP2 Galaxy Redshift Survey, which is a magnitude-limited spectroscopic survey performed using the DEIMOS spectrograph at the Keck 2 telescope. Galaxy spectra were observed in four fields, with targets lying in the magnitude range $R_{AB} < 24.1$. Field 1 (corresponding to the EGS) applied no redshift pre-selection, though objects expected to be at higher redshift received greater weight in targeting. In the remaining 3 fields, DEEP2 targeted only objects expected to be in the redshift range of $z > 0.75$. Only Field 1 is used for this paper. Details of DEEP2 are given in Newman et al. (2013).

The second spectroscopic sample included constitutes the public data release of spectra from the DEEP3 Galaxy Redshift Survey (Cooper et al., 2011, 2012), which was was primarily intended to enlarge the DEEP2 survey within the EGS field to take advantage of the wealth of multiwavelength information available there. This release is distributed at `http://deep.ps.uci.edu/deep3/home.html`. For details on DEEP3, we refer the reader to the appendix of the preprint on arXiv: `https://arxiv.org/abs/1903.08174`.

We also incorporate grism redshift data from the 3D-HST survey (Brammer et al., 2012; Momcheva et al., 2016), which measures redshift down to $JH_{IR} = 26$. The 3D-HST sample reaches higher redshifts than DEEP2 or DEEP3. The 3D-HST grism redshifts are derived using a combination of grism spectra and photometric data, and proper selection is needed to ensure a set of robust redshifts. The selection criteria used are described in section 2.7.

2.2.2   Photometry in *ugriz* bands

For the ***ugriz*** bands, we used the CFHTLS-T0007 (Hudelot et al., 2012) catalogs of photometry from CFHT/MegaCam. We utilize data from the CFHTLS Deep field D3 as

well as the seven pointings in the Wide field W3 which overlap with DEEP2/3 and 3D-HST. The list of pointings may be found in Table 2. The CFHTLS Wide field sample reaches 5σ depths of $u \sim 24.7$, $g \sim 25.4$, $r \sim 24.8$, $i \sim 24.3$, and $z \sim 23.5$. The CFHTLS Deep data reaches 5σ depths of $u \sim 27.1$, $g \sim 27.5$, $r \sim 27.2$, $i \sim 26.9$, $i_2 \sim 26.6$, and $z \sim 25.8$, where i_2 is the replacement filter for the i-band filter. This filter was named y in the CFHTLS catalogs, but within this paper and in our catalogs we refer to this filter as i_2 to avoid confusion with the y-band in the LSST $ugrizy$ filter system. The default photometry from CFHTLS is the Kron-like elliptical aperture magnitude MAG_AUTO. We also have calculated a set of corrected aperture magnitudes as described below, which we designate as MAG_APERCOR in catalogs. See section 2.5 for details of the aperture correction procedure applied.

We have utilized an internal version of the Pan-STARRS1 (PS1) catalog (Chambers et al., 2016; Magnier et al., 2016) to calibrate the photometric zero-points for the $griz$ and Y bands. For the CFHTLS u-band we have used the Deep field photometry as the standard against which we calibrate the Wide field data, as described in section 2.4.3.

2.2.3 Y-band data

In addition to the $ugriz$ bands which are included in CFHTLS, LSST will obtain data in the y band. To obtain photometry of comparable depth in a similar filter, we used the Y-band filter available for Suprime-Cam on the Subaru telescope (Miyazaki et al., 2002) over the course of two nights to cover a portion of the DEEP2 EGS field. The wavelength coverage of this filter is slightly redder and narrower than the LSST y-band filter, but it is otherwise similar. The Y-band observations consist of two pointings centered on RA = $14^h17^m58.2^s$, Dec = $+52°36'4.0''$ and RA = $14^h22^m28.0^s$, Dec = $+53°24'58.0''$, with exposure times of 234 min and 9 min, respectively. The unequal exposure times were not planned, but rather a result of the onset of poor weather conditions. The 5σ depth of the two pointings are 25.0 and 23.4 mag, respectively, and the seeing full width at half maximum (FWHM) values were $0.662''$ and $0.632''$, respectively. A mosaic was created using the Subaru/Suprime SDFRED2 pipeline (Ouchi et al., 2004). The initial astrometry for the mosaic was determined using Astrometry.net (Lang et al., 2010). We then used SExtractor (Bertin & Arnouts, 1996) to detect sources and obtain a photometric catalog. Slightly different SExtractor

parameters were used for the two pointings to account for differences in depth and seeing. The parameters are listed in Appendix A. An initial "guess" of the image zero-point was used for SExtractor. We determine a more accurate zero-point later in the calibration procedure as described in section 2.4. A subset of the detected sources were visually inspected to optimize the parameters, enabling us to minimize false detections and to ensure that nearby and overlapping sources are de-blended properly.

SExtractor requires a weight map for processing. To create the weight map, we set the BACK_SIZE parameter to 16, and the resulting BACKGROUND_RMS check image was used as the weight map (in other words, the RMS of the background evaluated over 16 pixel boxes was used as a weight map). To avoid false detections near the image boundary, objects within 15 pixels of the image boundary were not used. The astrometry was further corrected by cross-matching to SDSS (cf. section 2.3). Besides the default MAG_AUTO photometry, we also produced aperture photometry (MAG_APER) with aperture diameters ranging from 9 pixels to 56 pixels in 1 pixel spacing (the pixel size of SuprimeCam is $0.2''$). The MAG_APER photometry and half-light radius were used to calculate the corrected aperture magnitudes as described in section 2.5.

The sky coverage of the datasets incorporated in this work is shown in Fig. 1.

2.3   ASTROMETRIC CORRECTION

To avoid false matching between catalogs, we applied astrometric corrections to CFHTLS, the Y-band catalog, and PS1 to make them each match the SDSS coordinate system before cross-matching the catalogs. The astrometric offsets required varied spatially for each of these datasets. There was no significant offset between DEEP2/3 positions (which were previously remapped to match SDSS coordinates) and SDSS. For 3D-HST, a constant RA and Dec offset were needed to match SDSS but no spatial variation in offsets was needed.

In order to derive astrometric corrections for the CFHTLS, Subaru Y-band, and PS1 catalogs to match SDSS, we have applied the same methodology as described in Matthews et al. (2013). In this paper we give only a brief outline of these techniques; we refer the reader
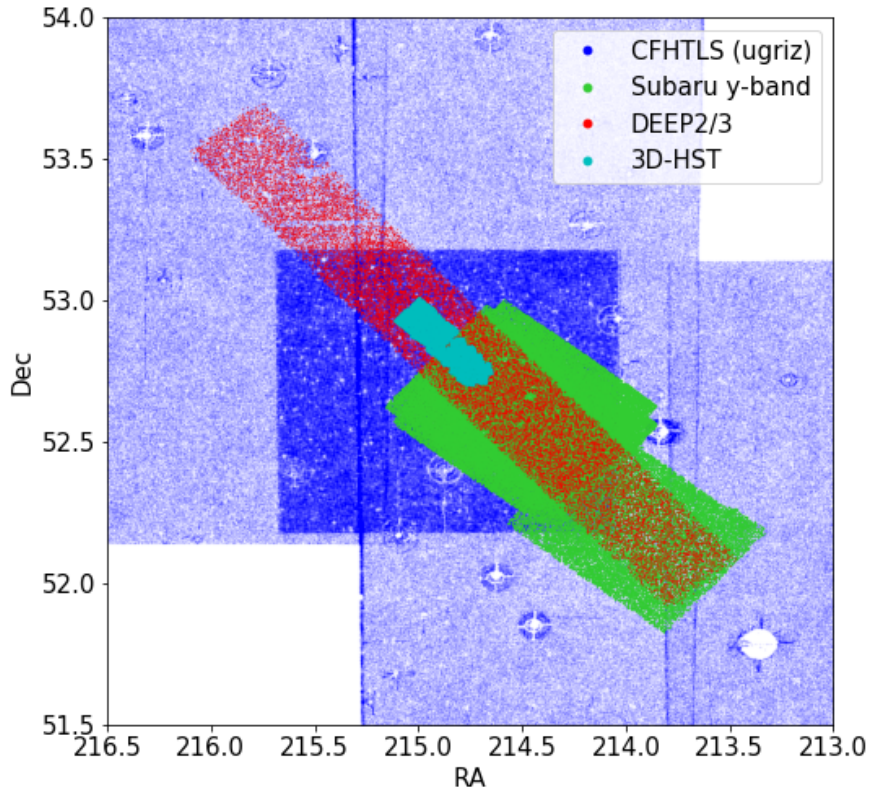
Figure 1: Sky coverage of the catalogs used in this paper (Pan-STARRS1 and SDSS are not shown as they cover the entire region). The region covered by DEEP2 and DEEP3 is shown in red, 3D-HST is in cyan, the CFHTLS imaging pointings included in our catalogs are shown in blue, and the two rectangular pointings of Subaru Y-band imaging are shown in green (the deeper of the two pointings partially overlaps with 3D-HST).

to this prior work for details. We describe the correction of CFHTLS for sake of example.

The correction is done separately for each pointing from CFHTLS. First we cross-match CFHTLS to SDSS with a search radius of $1.0''$. If more than one match is found, the nearest match is kept. The differences in RA and Dec (ΔRA and ΔDec) are calculated for every matched object. The matched objects are binned according to their RA and Dec, with a bin size of $1.2' \times 1.2'$. This bin size was chosen because smaller bins did not significantly reduce the residuals and could lead to problems with over-fitting. Within each bin, the mean value of the ΔRA and ΔDec are calculated using the robust Hodges-Lehmann estimator (Hodges & Lehmann, 1963). For bins that have fewer than 3 objects, values from the neighboring bins are used. A 3×3 boxcar average is performed to smooth ΔRA and ΔDec, and we perform bivariate spline interpolation on the smoothed ΔRA and ΔDec grid to obtain the functions ΔRA(RA, Dec) and ΔDec(RA, Dec). For each object in the CFHTLS catalogs we then evaluate ΔRA(RA, Dec) and ΔDec(RA, Dec) to determine the offsets at its position, and subtract them from the CFHTLS coordinates. The same method is used to correct the astrometry of PS1 and the Y-band catalog, with the only difference being the bin sizes used ($4' \times 4'$ and $1.7' \times 1.7'$, respectively, for PS1 and Subaru). Table 1 lists the mean and standard deviation of ΔRA and ΔDec for each catalog before and after these corrections.

2.4 PHOTOMETRIC ZERO-POINT CALIBRATION

The CFHTLS photometry is in the AB system but has systematic zero-point offsets that must be corrected. We also need to determine the Y-band zero-point. PS1 has $grizy$ photometry that is well-calibrated (Magnier et al., 2016), so it is well-suited to use as a standard for improving the calibration of most bands used in this work. The calibration of CFHTLS u-band must be handled differently, however, since this filter is not observed by PS1. Our methods for u-band calibration are described in section 2.4.3.

2.4.1 Pan-STARRS1 catalog

The PS1 catalog contains columns corresponding to the mean flux, median flux and flux error in each band for all objects. For convenience we convert the mean flux and flux error

Table 1: The mean and RMS of $\mathrm{RA_{CFHTLS}} - \mathrm{RA_{SDSS}}$, $\mathrm{RA_{Subaru}} - \mathrm{RA_{SDSS}}$ and $\mathrm{RA_{PS1}} - \mathrm{RA_{SDSS}}$. The values before correction are listed as plain text and the values after correction are in *italic* font. The astrometric corrections applied are described in section 2.3.

Pointing	$\mathrm{RA} - \mathrm{RA_{SDSS}}('')$		$\mathrm{dec} - \mathrm{dec_{SDSS}}('')$	
	mean	σ	mean	σ
CFHTLS D3	0.071	0.303	-0.023	0.180
	0.003	*0.267*	*0.002*	*0.155*
CFHTLS W3-0-1	0.107	0.286	0.016	0.157
	0.002	*0.257*	*0.000*	*0.150*
CFHTLS W3-1-2	0.058	0.271	0.042	0.163
	0.002	*0.258*	*0.001*	*0.152*
CFHTLS W3-0-3	0.125	0.281	-0.011	0.155
	0.004	*0.243*	*-0.001*	*0.148*
CFHTLS W3+1-2	0.075	0.269	-0.027	0.155
	0.001	*0.252*	*0.000*	*0.147*
CFHTLS W3-0-2	0.107	0.284	-0.007	0.158
	0.001	*0.259*	*0.000*	*0.151*
CFHTLS W3+1-1	0.094	0.266	0.007	0.150
	0.002	*0.243*	*0.000*	*0.146*
CFHTLS W3-1-3	0.033	0.252	-0.003	0.157
	0.003	*0.244*	*0.000*	*0.147*
Subaru Y-band	-0.042	0.285	-0.165	0.296
	-0.001	*0.259*	*0.000*	*0.151*
PS1	0.020	0.285	-0.022	0.171
	-0.001	*0.264*	*0.000*	*0.153*

to AB magnitude and magnitude error via standard error propagation. To eliminate false detections, we require that an object has at least three "good" detections (nmag_ok≥1) in the six bands. The PS1 photometry has been found to have small zero-point offsets compared to the standard AB system (Scolnic et al., 2015); we have shifted the PS1 *grizy* magnitudes by +20, +33, +24, +28, and +11 mmag (*griz* offsets from Table 3 of Scolnic et al. 2015; *y*-band offset from private communication from Dan Scolnic), respectively, to match to the AB system.

2.4.2 Zero-point calibration of *grizY* bands

The filter throughputs and overall system responses vary between different telescopes even for the same nominal band, so in general the measured fluxes of the same source should differ between catalogs. However, if the filter responses are sufficiently similar and the source spectrum is nearly flat over the filter wavelength range, the brightness measured from the two telescopes should be approximately the same, as the color measured between any two instruments/filters should be zero for a flat spectrum source (by the definition of the AB system). Such flat-spectrum sources can be approximated by observed objects with zero color in the AB system; the magnitudes measured from two telescopes should be the same for these objects if all photometry is properly calibrated to AB. Based on this idea, we calculated the zero-point offset between PS1 and other photometry by performing a linear fit of magnitude difference as a function of color for stars that are found in a given pair of catalogs:

$$g_c - g_p = a_{0,g} + a_{1,g} * (g_p - r_p), \tag{2.1a}$$

$$r_c - r_p = a_{0,r} + a_{1,r} * (r_p - i_p), \tag{2.1b}$$

$$i_c - i_p = a_{0,i} + a_{1,i} * (i_p - z_p), \tag{2.1c}$$

$$i2_c - i_p = a_{0,i} + a_{1,i} * (i2_p - z_p), \tag{2.1d}$$

$$z_c - z_p = a_{0,z} + a_{1,z} * (i_p - z_p), \tag{2.1e}$$

$$Y_s - y_p = a_{0,y} + a_{1,y} * (z_p - y_p), \tag{2.1f}$$

where $a_{0,m}$ is the zero-point offset, and the subscripts c, s, and p stand for CFHTLS, Subaru and PS1, respectively. As noted previously, the variable $i2$ in equation 2.1d represents the magnitude from the replacement filter for the CFHTLS i-band, which was slightly different from the original i-band filter. It is labeled as the y-band in CFHTLS catalogs, but we relabel it $i2$ here to avoid confusion with the Subaru Y-band.

In order to perform these fits, we have cross-matched the PS1 catalog to CFHTLS and Subaru with a search radius of 1.0 arcsec. To avoid objects with large photometric errors in PS1, we require the PS1 magnitude errors to be smaller than 0.05 mag in both bands used for a given fit. Only stars that are not saturated or masked are used for calculating the offsets. For $griz$ bands, we require the "flag" value in the CFHTLS catalog be 0 ("star" and "not saturated or masked") and the SExtractor flag in each band to be smaller than 3, providing an additional rejection of saturated objects.

To select stars for the Y-band, we used the star/galaxy classifier "CLASS_STAR" from SExtractor, selecting those objects with CLASS_STAR > 0.983. There are a number of objects with much larger size that are misclassified as stars, and we removed them by applying a cut on the half-light radius: $r < 0.44''$ for the deep pointing and $r < 0.41''$ for the shallow pointing. We also removed saturated objects by requiring the SExtractor flag be smaller than 3 and applying a cut on MAG_AUTO to reject the brightest objects, corresponding to **MAG_AUTO > 17.0** for the deep pointing and **MAG_AUTO > 15.0** for the shallow pointing.

To avoid influence from outliers, we applied robust linear fitting using the Python package "statsmodels" and used Huber's T as an M-estimator with the tuning constant $t = $ **2MAD**, where MAD is the median absolute deviation between the data and the fit. The zero-point calculation is done separately for each pointing in the CFHTLS Wide field, and separately for the two Y-band pointings. Fig. 2 shows the linear fit of equations 2.1a to 2.1f using the MAG_AUTO photometry for the CFHTLS Deep field and the Subaru deep pointing. The coefficients from the linear fits are listed in Table 2 for CFHTLS and Table 3 for the Subaru Y-band. The a_0 in Table 3 corresponds to the offset between the initial zero-point value for the Y-band image and the zero-point of PS1.

So far we have assumed that the zero-point offset is uniform in each pointing. That might not be the case, and we also tried correcting for any spatial variations of the zero-point offset.
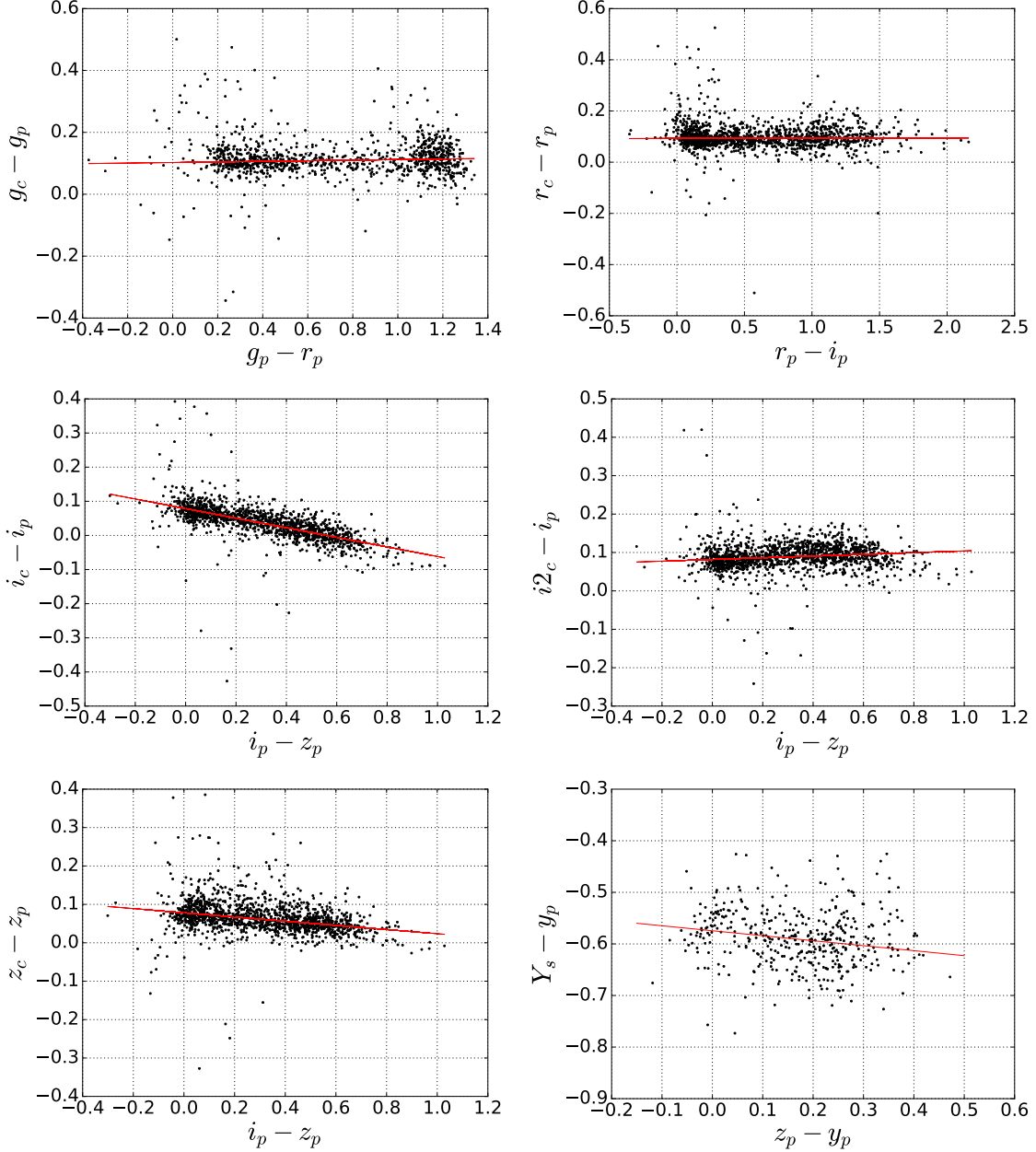
Figure 2: Linear fitting for calculating the zero-point offsets. Panels (a-e) show difference in magnitude between CFHTLS Deep field D3 (subscript c) and PS1 (subscript p) plotted as a function of color. (f) shows the same plot for Subaru Y-band (subscript s) from the deep pointing. Only stars are used. The red lines are the linear fits described by equations 2.1a to 2.1f. The intercepts correspond to the zero-point offsets between the two systems, and are listed in Tables 2 and 3.

Table 2: Coefficients in equations 2.1a to 2.1f for CFHTLS. The coefficient a_0 corresponds to the zero-point offset between CFHTLS and Pan-STARRS, and is subtracted from the CFHTLS magnitudes to obtain calibrated values.

Pointing	Method	g band		r band		i band		$i2$ band		z band	
		a_0	a_1	a_0	a_1	a_0	a_1	a_0	a_1	a_0	a_1
D3	MAG_AUTO	0.055	0.004	0.038	0.000	0.039	-0.128	0.044	0.029	0.038	-0.048
	MAG_APERCOR	0.017	0.005	0.000	0.001	0.004	-0.145	0.010	0.013	-0.002	-0.062
W3-0-1	MAG_AUTO	0.074	0.024	0.042	0.024	0.023	-0.110	-	-	0.035	-0.029
	MAG_APERCOR	0.048	-0.007	0.002	0.012	-0.008	-0.143	-	-	0.001	-0.064
W3-1-2	MAG_AUTO	0.081	0.015	0.036	0.011	0.042	-0.122	-	-	0.062	-0.036
	MAG_APERCOR	0.039	-0.001	0.011	0.001	0.000	-0.150	-	-	0.012	-0.067
W3-0-3	MAG_AUTO	0.071	0.006	0.036	0.005	0.032	-0.128	-	-	0.061	-0.036
	MAG_APERCOR	0.033	0.000	-0.004	-0.002	-0.001	-0.158	-	-	0.006	-0.061
W3+1-2	MAG_AUTO	0.062	-0.005	0.064	-0.002	0.025	-0.124	-	-	0.053	-0.040
	MAG_APERCOR	0.032	-0.007	0.020	-0.010	-0.006	-0.143	-	-	0.006	-0.061
W3-0-2	MAG_AUTO	0.053	0.012	0.067	0.017	0.030	-0.127	-	-	0.060	-0.031
	MAG_APERCOR	0.019	0.010	0.027	0.001	0.001	-0.149	-	-	0.013	-0.068
W3+1-1	MAG_AUTO	0.067	0.008	0.055	0.005	0.018	-0.119	-	-	0.058	-0.010
	MAG_APERCOR	0.031	0.000	0.015	-0.004	-0.003	-0.144	-	-	0.003	-0.060
W3-1-3	MAG_AUTO	0.065	0.000	0.056	0.001	0.025	-0.112	-	-	0.027	-0.031
	MAG_APERCOR	0.028	-0.006	0.015	-0.009	-0.013	-0.142	-	-	-0.016	-0.060

Table 3: Coefficients in equation 2.1f for Subaru Y-band photometry. The coefficient a_0 corresponds to the zero-point offset between initial zero-point value for the Y-band image and PS1. These offsets are subtracted from the Y-band magnitude to obtain calibrated values.

Pointing	Method	a_0	a_1
Deep	MAG_AUTO	-0.584	-0.097
	MAG_APERCOR	-0.646	-0.101
Shallow	MAG_AUTO	-0.653	-0.145
	MAG_APERCOR	-0.695	-0.142

21

To do this, we used a fixed value of the slope a_1 from the previous fit, and calculated the zero-point offset a_0 for each matching star. For example, the g-band offset for the j-th object is calculated as follows:

$$a_{j,0,g} = g_{j,c} - g_{j,p} - a_{1,g} * (g_{j,p} - r_{j,p}).\qquad(2.2)$$

After obtaining the zero-point offsets for each object, we obtained the spatial variation of the zero-point offset $a_{0,m}(\text{RA}, \text{Dec})$ by fitting the zero-point offset to a 2nd order bivariate polynomial of RA and Dec. Then we obtained the calibrated magnitudes: $m' = m - a_{0,m}(\text{RA}, \text{Dec})$. To test if the spatial correction actually improves the photometry, we calculated the median absolute deviation (MAD) of $a_{0,m}$ before and after spatial zero-point correction. Here we randomly select 75% of all objects to calculate the bivariate polynomial fit, and apply the correction on the other 25%. We repeat this procedure many times to find the statistical distribution of the difference in MAD before and after correction. For corrections to be statistically significant, we require that MAD should be smaller after correction at least 95% of the time. Only one pointing in CFHTLS met this requirement in one band (z-band). Thus we conclude that there is no significant improvement by applying spatially varying zero-point corrections, so uniform corrections were applied instead.

2.4.3   Calibration of the u-band

Because there is no u-band in PS1, the zero-point calibration of CFHTLS u-band is done differently. We tried using SDSS u-band as the standard photometry, but we encountered difficulties with this approach. First, the SDSS u-band is significantly bluer (by ~ 270Å) than the CFHTLS u-band; as a result the slope a_1 is large and our assumptions are less valid. Secondly, there are not many stars near zero color in $u - g$, and the stars that do have colors near zero exhibit large scatter. What is worse, SDSS photometry is not exactly in the AB system. For the u-band, it is estimated that $u_{SDSS} = u_{AB} + 0.04$ mag with uncertainties at the 0.01 to 0.02 mag level[2]. Because of these problems, we have instead assumed that the CFHTLS Deep field u-band is well calibrated based on the tests done for the SNLS survey (Hudelot et al., 2012), and calibrate the u-band zero-point of Wide field pointings by

---

[2]http://www.sdss.org/dr12/algorithms/fluxcal/#SDSStoAB

requiring that their $u-g$ vs. $g-r$ stellar locus matches that from the Deep field. According to Hudelot et al. (2012), the calibration accuracy is at the 2% level in the u-band for the Deep field. Although this uncertainty in the absolute calibration remains, the procedure we have followed ensures that all the pointings at least have a uniform zero-point offset from the AB system, ensuring consistent photometry for calculating photometric redshifts.

Because not all of the CFHTLS Wide pointings overlap with the CFHTLS Deep pointing, direct calibration of the u-band by cross-matching Wide and Deep objects is not feasible. Thus we resort to an indirect calibration approach. Specifically, if all pointings are calibrated in the u, g and r bands, their $u-g$ vs. $g-r$ stellar loci should be the same. Since g and r are already calibrated, the only shift in the stellar locus should be in the $u-g$ direction, and correspond to variations in the u-band zero-point. To tie the u-band zero-point of Wide field pointings to the Deep field, we therefore need to find the relative shift in the $u-g$ direction between the stellar loci in the Deep field and a Wide field pointing.

To do this, we first selected stars in the range $0.4 < g-r < 0.8$ and $u-g > 0.7$, where the stellar locus is roughly a straight line (the second cut removes outliers that are much bluer in the $g-r$ color range). The colors of the selected stars in the Deep field were fitted to a linear function. With the same color cuts, we fitted the stars in the wide field pointings with a slope fixed at the Deep field value, so that the only variable is the intercept. Fig. 3 shows the $u-g$ vs. $g-r$ stellar loci and linear fits for the Deep field and one of the Wide field pointings. The differences in the intercept between the Wide field pointings and the Deep field are the u-band zero-point offsets, and they are listed in Table 4.

2.4.4 Correction for dust extinction

The original CFHTLS $ugri(i2)z$ photometry is not corrected for Galactic extinction, nor are the PS1 magnitudes used for the photometric zero-point calibration. After zero-point calibration, we applied extinction corrections to the $ugri(i2)z$ and Y-band photometry. We followed the procedure described in Schlafly & Finkbeiner (2011), and calculated $A_b/E(B-V)_{\mathrm{SFD}}$, where A_b is the total extinction in a specific band and $E(B-V)_{\mathrm{SFD}}$ is the SFD reddening value (Schlegel et al., 1998). We assumed a Fitzpatrick (1999) extinction law with $R_V = 3.1$ and used the total transmission curves of each filter for the calculation.

Table 4: The u-band zero-point offsets of the Wide field pointings relative to the Deep field. These offsets are subtracted from the Wide field u-band magnitude to obtain calibrated values.

Pointing	W3-0-1	W3-1-2	W3-0-3	W3+1-2	W3-0-2	W3+1-1	W3-1-3
MAG_AUTO	0.03	0.03	0.02	0.12	0.01	0.08	0.01
MAG_APERCOR	0.06	0.04	0.02	0.02	-0.02	0.03	0.00
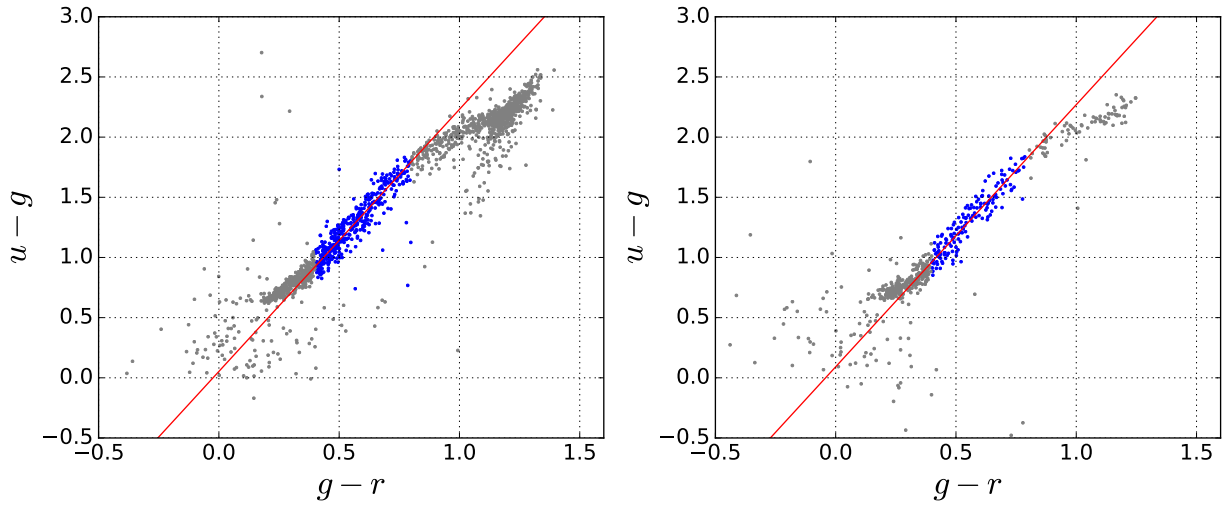
Figure 3: Stellar loci of $u - g$ vs. $g - r$, using MAG_AUTO photometry. Left panel: stellar locus and linear fit of the Deep field. The red line shows a linear fit to the points in blue. The gray points are not used for the fit. The slope of the fit is used for the Wide field pointings. Right panel: Wide field pointing W3-0-1; the red line has the same slope as in Deep field, and the difference in the intercept corresponds to the zero-point offset.

Table 5: The values of $A_b/E(B-V)_{\mathrm{SFD}}$ in each band listed here were calculated using the procedure described in Schlafly & Finkbeiner (2011). The median A_b values are calculated for the set of DEEP2 and DEEP3 objects with spectroscopy.

Band	u	g	r	i	$i2$	z	y
$A_b/E(B-V)_{\mathrm{SFD}}$	4.010	3.191	2.249	1.647	1.683	1.295	1.039
Median A_b	0.038	0.031	0.022	0.016	0.016	0.012	0.010

With $A_b/E(B-V)_{\mathrm{SFD}}$, we calculated A_b using $E(B-V)_{\mathrm{SFD}}$ from the SFD dust map and applied corrections. Although the DEEP2/3 footprint is relatively small, there is a small spatial variation in $E(B-V)$ across the field, ranging from 0.006 to 0.022 with a median of 0.010. Thus we correct for this spatial variation using the SFD map. Table 5 shows these $A_b/E(B-V)_{\mathrm{SFD}}$ values and median A_b for each band.

2.5 CORRECTED APERTURE PHOTOMETRY

The MAG_AUTO from SExtractor is commonly used as the default photometry in extragalactic astronomy, and it is provided in our dataset. However it is not optimal for photometric redshift calculation for several reasons. First, it uses a relatively large aperture in order to capture most of the flux from the source, but larger apertures also lead to larger background noise. Secondly, even though a large aperture is used, it still cannot capture all the flux — in our analysis typically ~95% of the total flux of a point source is captured by MAG_AUTO. Thirdly, the fraction of flux captured by MAG_AUTO might be different for objects with different sizes or images with different point spread functions (PSF's). To address these problems, we developed a method to calculate the corrected aperture photometry for both point sources and extended objects. This method utilized the aperture magnitudes at different apertures provided within the public CFHTLS catalogs, and therefore it did not require any reprocessing of the CFHTLS images. The corrected aperture magnitude is la-

beled "MAG_APERCOR" in our catalogs. The MAG_APERCOR photometry is calibrated the same way as MAG_AUTO (as described in section 2.4), and its zero-point offsets are listed in Table 2, 3 and 4.

Here we summarize the techniques used for calculating "MAG_APERCOR". Details can be found in Appendix B. Our methods are similar to the aperture correction method described in Gawiser et al. (2006). In that work, it is assumed that all objects have a Gaussian light profile with a width calculated from the half-light radius. However, actual light profiles typically have more extended "wings" - i.e., more flux at large radius - than Gaussian profiles do. In our work, instead of a Gaussian profile, we have used the more flexible Moffat profile (cf. equation B.1), which has two free parameters, though we still assume that all objects have circularly symmetric light profiles that only depend on the half-light radius. This method essentially measures the flux in a small aperture ($r_0 = 0.93''$ for *ugriz* and $r_0 = 0.9''$ for *Y*-band) and extrapolates to infinity using the Moffat profile, the parameters of which are obtained by fitting the curve of growth (the fraction of included flux as a function of aperture radius). The aperture corrections for stars and galaxies are determined slightly differently, and the *Y*-band is also treated differently since *Y*-band imaging is not available for all objects. The steps of the aperture correction for *galaxies* in band *b* (which could be any band except *Y*) in pointing *x* are as follows:

1. Bin the objects in pointing *x* by their *r*-band half-light radius (FLUX_RADIUS from SExtractor);
2. For each *r*-band radius bin, find the averaged *b*-band curve of growth and fit the Moffat profile to that curve;
3. From the resulting best-fit parameters, obtain the correction factor
   ApCorr = Flux(∞)/Flux(r_0) for each radius bin;
4. Interpolate and extrapolate the relation between the correction factor ApCorr and the mean *r*-band half-light radius $R_{1/2,r}$ to obtain the continuous function ApCorr$_{x,b}(R_{1/2,r})$;
5. Use ApCorr$_{x,b}(R_{1/2,r})$ and the aperture magnitude of aperture radius r_0 to obtain the corrected aperture magnitude.

For stars, the procedure is the same except that they are not binned by radius, since the stars should effectively all have the same light profile set by the PSF; as a result, they are

all placed in a bin together.

Although we can reduce background noise by choosing a small aperture, any errors in half-light radius will propagate into the total photometric error via the correction factor, and this can be a big problem for bands that have low S/N. For this reason, instead of using the SExtractor radius measurement in each band to assign the correction factor, we calculate the correction factor as a function of r-band half-light radius. In this way we can obtain u-band MAG_APERCOR photometry even for objects with no valid radius measurement in the u-band. Although the absolute photometry can be affected by any r-band radius error, the colors are not affected as much because all bands use the same r-band radius for aperture correction and thus the magnitudes are all biased in the same direction. The one exception is the Y-band, for which we use the Y-band half-light radius to determine aperture corrections, as in some cases r measurements may not be available or may be noisy. The use of a matched radius makes MAG_APERCOR well-suited for calculating photometric redshifts. A comparison of the photo-z performance using MAG_AUTO and MAG_APERCOR is presented in section 2.7.

2.6   COMBINED CATALOGS

We cross-matched the CFHTLS, Subaru Y-band catalog and DEEP2/3 catalogs using a search radius of $1''$. CFHTLS Wide field pointings were first combined into a single catalog. For objects that appear in multiple pointings, we only kept the values from the objects that have the smallest r-band MAG_APER error. Then the Wide field combined catalog was combined with the Deep field, keeping only the Deep field value if there is overlap. The combined CFHTLS catalog was then matched to the Subaru Y-band catalog. This final combined catalog is matched to the DEEP2/3 catalog, and all DEEP2/3 objects and columns are kept, with additional columns from CFHTLS and Subaru Y-band added. DEEP2/3 provides a quality flag, "zquality". Objects with secure redshifts can be selected by requiring zquality ≥ 3 (see Newman et al. 2013).

Similarly, we produced a 3D-HST grism redshift catalog containing photometry from

CFHTLS *ugriz* and Subaru *Y*-band, as well as DEEP2/3 redshifts where available. To select objects with accurate grism redshifts, we require that either of the following criteria is met:
1.

```
((z_grism_u68-z_grism_l68)/(z_phot_u68-z_phot_l68)<0.1)
& ((z_grism_u68 - z_grism_l68) < 0.01)
& (z_best_s != 0)
& (use_phot == 1)
& (z_max_grism > z_phot_l95)
& (z_max_grism < z_phot_u95)
& (z_max_grism > 0.6)
OR
2.
(z_grism_err < 0.025)
& (use_zgrism == 1),
```

where all names are quantities provided in the 3D-HST catalog. We have compared the grism redshifts selected using the above criteria with DEEP2/3 redshifts; the normalized median absolute deviation between the spectroscopic and grism redshifts of the resulting sample is < 0.3%, and the fractions of objects with larger than $0.10(1 + z)$ or larger than $0.02(1 + z)$ redshift difference are 3% and 11%, respectively. For convenience, we added a flag "use_zgrism1" to the catalog, and objects that meet the above criteria are assigned the flag value 1; otherwise this flag value will be 0.

Before cross-matching, the CFHTLS Deep and Wide catalogs include 603852 and 1415859 objects, respectively, and the *Y*-band catalog includes 94014 objects. The combined DEEP2/3 catalog from the aforementioned cross-matching procedures includes 8479 objects with *ugrizY* photometry and secure DEEP2/3 redshifts, and the combined 3D-HST catalog provides an additional 741 objects with accurate grism redshifts. Fig. 4 shows the distribution of *r*-band magnitude (MAG_APERCOR) and redshift for objects with *ugrizY* photometry and secure redshift measurements.

The columns in the catalogs are structured in the following way: the first columns listed are those from the relevant spectroscopic/grism catalog; then the columns from CFHTLS
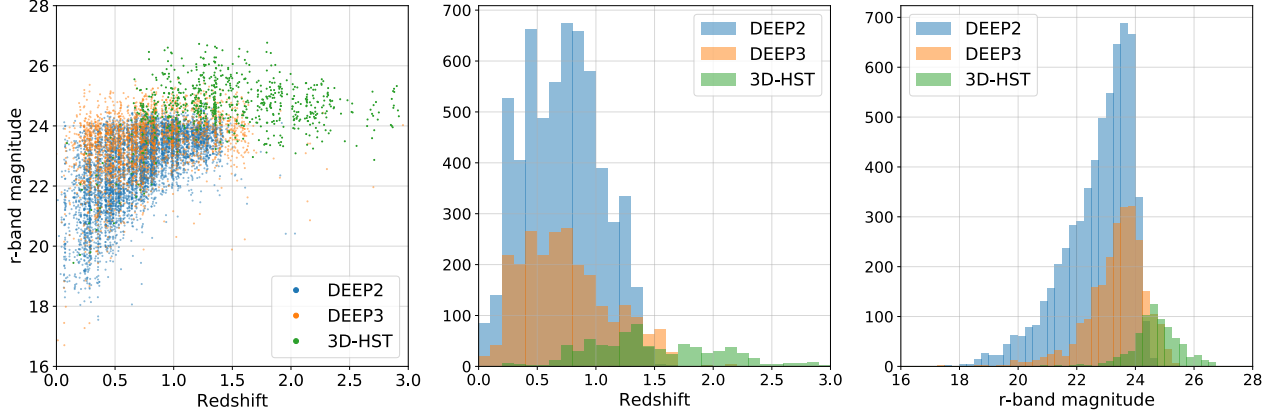
Figure 4: Left panel: r-band magnitude vs. redshift for objects in DEEP2, DEEP3 and 3D-HST with $ugrizY$ photometry. If an object appears in both DEEP2/3 and 3D-HST, only the DEEP2/3 object is plotted. The large-scale structure is clearly visible. The middle panel and the right panel show the redshift distributions and the r-band magnitude distributions, respectively.

Table 6: Description of some of the principal columns included in our matched catalogs. The last three columns are DEEP2/3 values added to the 3D-HST catalog.

Column Name	Description
u, g, ...	MAG_AUTO magnitude in u-band, g-band, ...
uerr, gerr, ...	MAG_AUTO magnitude error in u-band, g-band, ...
u_apercor, g_apercor, ...	MAG_APERCOR magnitude in u-band, g-band, ...
uerr_aper, gerr_aper, ...	MAG_APERCOR magnitude error from image noise in u-band, g-band, ...
uerr_apercor, gerr_apercor, ...	MAG_APERCOR magnitude error from correction uncertainty in u-band, g-band, ...
r_radius_arcsec	r-band half-light radius in arcsec
y_radius_arcsec	Y-band half-light radius in arcsec
cfhtls_source	source of the $ugri(i2)z$ photometry: 0 = Deep field; 1 = Wide field; -99 = not observed
subaru_source	source of the Y-band photometry: 0 = deep pointing; 1 = shallow pointing; -99 = not observed
ra_deep2, dec_deep2	right ascension and declination from DEEP2/3
ra_cfhtls, dec_cfhtls	right ascension and declination from CFHTLS after astrometric correction
ra_subaru, dec_subaru	right ascension and declination from the Subaru Y-band data after astrometric correction
sfd_ebv	E(B-V) from Schlegel, Finkbeiner, and Davis (1998) dust map
zhelio	(In DEEP2/3 catalog) DEEP2/3 heliocentric redshift
zquality	(In DEEP2/3 catalog) DEEP2/3 redshift quality flag
use_zgrism1	(In 3D-HST catalog) our grism redshift quality flag: 0 = less accurate; 1 = accurate
z_max_grism	(In 3D-HST catalog) 3D-HST grism redshift
z_deep2	(In 3D-HST catalog) DEEP2/3 heliocentric redshift
z_err_deep2	(In 3D-HST catalog) DEEP2/3 redshift error
zquality_deep2	(In 3D-HST catalog) DEEP2/3 redshift quality flag

with MAG_APERCOR and its errors are provided; and finally the Y-band columns are given. In the 3D-HST catalog, we also include columns of DEEP2/3 redshift and other values. Description of the DEEP2/3 columns can be found at http://deep.ps.uci.edu/deep3/ztags.html and are described in Newman et al. (2013). Description of the 3D-HST columns can be found in Table 5 of Momcheva et al. (2016). Description of the CFHTLS columns can be found at http://terapix.iap.fr/cplt/T0007/doc/T0007-docsu22.html. The Y-band columns follow the same naming convention as CFHTLS. Note that the "y" variant of the CFHTLS i-band is relabeled $i2$ in our catalogs to limit confusion. In the catalogs, 99 indicates non-detection and -99 indicates the object/quantity is not observed. Columns of principal interest are described in Table 6.

MAG_APERCOR has two sources of error: image noise and uncertainty in aperture correction. We note that errors in colors cannot be obtained by simply adding up the two kinds of errors in quadrature due to covariances between how magnitudes were determined in each band; color errors will be smaller than one would expect if measurements in each filter were assumed to be independent. More details of how to use the errors in MAG_APERCOR can be found in Appendix B.

We also provide the photometry-only catalogs of CFHTLS Wide, CFHTLS Deep and Y-band. These catalogs contain calibrated MAG_AUTO and MAG_APERCOR photometry, but are not matched to any other dataset.

All the catalogs are publicly available at http://d-scholarship.pitt.edu/36064/.

2.7   PHOTOMETRIC REDSHIFT TESTS

In this section, we describe the photo-z tests performed on the catalogs. In general, there are two classes of method for calculating the photometric redshifts. One is the template-fitting method, in which the redshift is obtained from the best fit to the photometry (in the chi-squared sense) determined using known template SEDs. The other is the empirical method, in which a dataset with spectroscopic redshifts is used to train an empirical relation between photometry and redshift (typically via machine learning algorithms), and the

empirical relation is then applied to new photometric data to estimate the redshift. Here we use a machine learning algorithm called random forest regression (Breiman, 2001) which is included in the Python package *Scikit-learn* (Pedregosa et al., 2011). Random forest is an ensemble learning method based on decision trees. A simple decision tree is trained by minimizing the sum of squared errors, and it tends to fit the noise in the data (i.e., over-fitting). The over-fitting results in reduced accuracy when the algorithm applied to new data. Random forest addresses this problem in two ways. First, a large number of new samples are created by bootstrapping the original training sample, and separate decision trees are trained using each sample. Secondly, instead of all the features (colors in our case), a random subset of the features may be used at each tree split to reduce the correlation between the trees. Although over-fitting can occur in individual trees, the effect is reduced by using subsets of features and averaged out by combining the predictions from all the trees. In our analysis using a subset of features did not significantly improve the results, and thus all available features were used at each split.

Both DEEP2/3 and 3D-HST data were employed to train and assess the performance of the algorithm. The selection of DEEP2/3 and 3D-HST redshifts is described in section 2.6. For objects that appear in both DEEP2/3 and 3D-HST, the DEEP2/3 redshift values are used. To avoid training and testing on the same dataset, we applied the K-fold cross-validation method: the dataset is first randomly divided into 5 subsets. Then one subset is selected as the testing set and the other 4 subsets are combined as a training set for optimizing the random forest, and this procedure is repeated 5 times so that the entire dataset has been used as the testing set in the end. The estimated photometric redshift derived for a given object when it was in the testing set is then compared with the spectroscopic/grism redshift (from now on simply spectroscopic redshift or z_{spec} for convenience) and the redshift difference $\Delta z = z_{phot} - z_{spec}$ is calculated. Two quantities are used to evaluate the photo-z performance here: the normalized median absolute deviation $\sigma_{\mathrm{NMAD}} = 1.48\,\mathrm{MAD}$, where $\mathrm{MAD} = \mathrm{median}(|\Delta z|/(1 + z_{spec}))$, and the outlier fraction η which is defined as the fraction of objects with $|\Delta z| > 0.15/(1 + z_{\mathrm{spec}})$.

For consistent S/N in the photometry, the CFHTLS Wide field and Deep field are tested separately, and in both cases the Y-band photometry from both the deep and shallow pointing

are used. Valid photometry in all six bands ($ugrizY$) is required. We have tested the photometric redshift performance for both MAG_AUTO and MAG_APERCOR photometry. The five colors $u - g$, $g - r$, $r - i$, $i - z$, $z - y$ and i-band magnitude are used as the input.

Fig. 5 shows the photo-z results using the CFHTLS Wide field photometry, and Fig. 6 shows the results with CFHTLS Deep field photometry. We find that using the MAG_APER-COR photometry, we achieve photo-z accuracy $\sigma_{\mathrm{NMAD}} = 0.018$ and outlier fraction of 4.7% in the CFHTLS Deep field, and $\sigma_{\mathrm{NMAD}} = 0.039$ and 6.3% outliers in the CFHTLS Wide field. This represents a significant improvement over MAG_AUTO: σ_{NMAD} is reduced by 28% in CFHTLS Wide and 27% in CFHTLS Deep, and there is also a significant reduction in the outlier fraction. The scatter in Δz is larger at $z_{\mathrm{spec}} > 1.4$ for both MAG_AUTO and MAG_APERCOR photometry and in both the Deep and Wide areas. This is due to both the small number of training objects in this redshift range, as well as the lack of available features (e.g., the 4000Å break) in the optical.

As an additional validation of the MAG_APERCOR photometry, we have performed similar photo-z tests using the CFHTLS photometry from the 3D-HST photometric catalogs (Skelton et al. 2014). In that work, the objects were detected with HST imaging, and forced photometry of these objects were performed on the CFHTLS Deep $ugriz$ images with an aperture of $1.2''$. We performed photo-z tests using the $ugriz$ photometry from Skelton et al. (2014) and redshifts from DEEP2/3 and 3D-HST, and for comparison we ran the same test using the CFHTLS Deep MAG_AUTO and MAG_APERCOR photometry in $ugriz$ bands for the same objects. We find that the Skelton et al. (2014) $ugriz$ photo-z's have very similar accuracy to the MAG_APERCOR photo-z's, with the former having 2% smaller σ_{NMAD} and 17% fewer outliers. Both significantly outperform the MAG_AUTO photo-z's, with the Skelton et al. (2014) $ugriz$ photo-z's having 37% smaller σ_{NMAD} and 47% fewer outliers than MAG_AUTO.

The CFHTLS Deep field and the Subaru Y-band have depth similar to LSST 10-year data. Therefore this test also demonstrates that in the magnitude and redshift range of DEEP2/3, at least, it is possible for LSST to achieve the goal of $0.03(1 + z)$ photo-z accuracy as specified by the Science Requirements Document of the LSST Dark Energy Science Collaboration (Collaboration et al., 2018b).
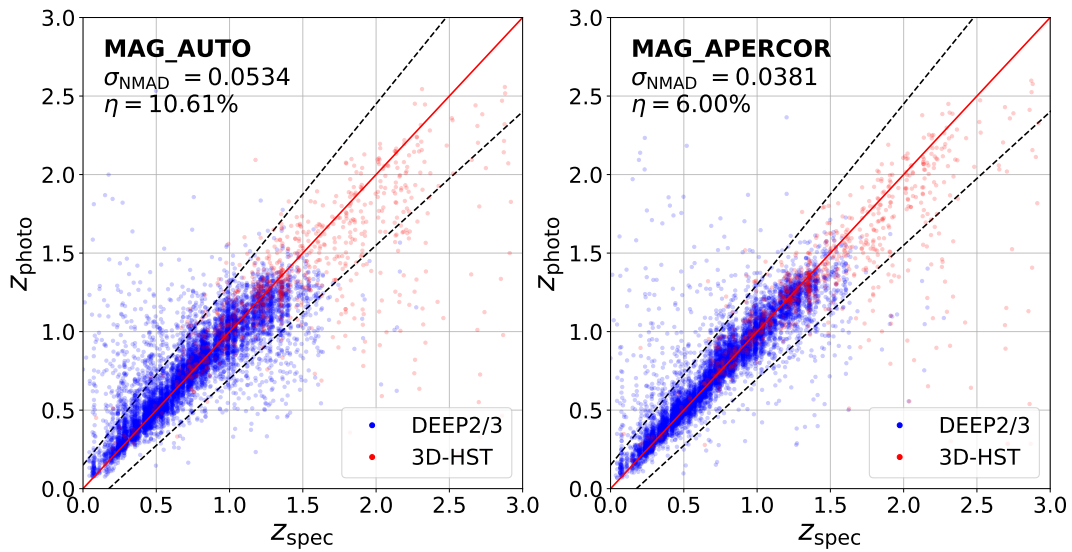
Figure 5: Photometric redshift vs. spectroscopic or grism redshift using CFHTLS Wide field *ugriz* and Subaru *Y*-band photometry. The red solid line corresponds to $z_{\mathrm{photo}} = z_{\mathrm{spec}}$. The dashed lines mark the boundary separating the outliers. The MAG_APERCOR photometry produces photo-z's with significantly better accuracy than MAG_AUTO.
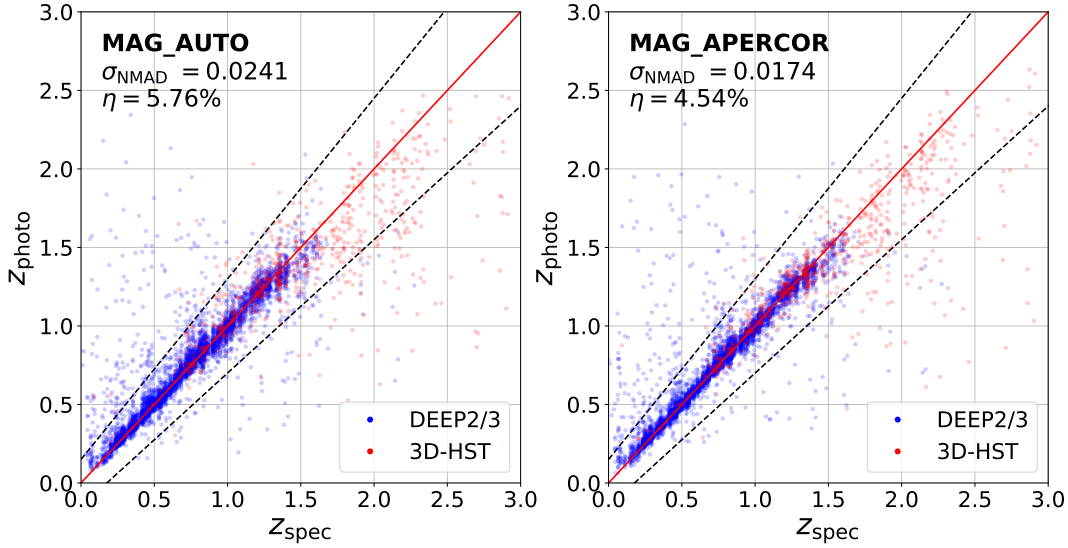
Figure 6: Same as Fig. 5, but using CFHTLS Deep field photometry instead.

2.8 SUMMARY

In this work we have presented a set of new catalogs with improved $ugrizY$ photometry and spectroscopic or grism redshifts in the Extended Groth Strip. We calibrated CFHTLS $ugriz$ photometry and Subaru Y-band photometry and also produced corrected aperture magnitudes. We combined the $ugrizY$ photometry with DEEP2/3 and 3D-HST redshifts. The $ugrizY$ photometry has depth similar to the LSST 10-year stack, and the catalogs will be useful for LSST photo-z tests. All data is publicly available.

We have implemented a random forest photo-z algorithm on our dataset, and found the photo-z accuracy to be $\sim 2\%$ or better for the available spectroscopic sample in the deepest region, where the photometry has LSST-like depth. We also found significant improvement in photo-z accuracy from the corrected aperture magnitude, indicating that our corrections provide a real improvement in the measurement of galaxy colors (as they tighten the color-redshift relation).

3 THE CLUSTERING OF DESI-LIKE LUMINOUS RED GALAXIES USING PHOTOMETRIC REDSHIFTS

3.1 INTRODUCTION

The selection of spectroscopic targets is an important part of the preparations for DESI. To optimize the selection of DESI galaxy targets, it is important to understand the properties of these galaxies. An important class of DESI targets is luminous red galaxies (LRGs). The high large-scale structure bias of the LRGs make them ideal tracers for the underlying matter distribution, and therefore important for measuring the baryon acoustic oscillation (BAO) signal. Although similar sets of LRGs have been observed in other programs, these samples are either at lower redshifts or are much sparser than the DESI LRG sample. The clustering properties of the DESI LRG sample has not been studied in detail to date.

In this paper we the present small-scale ($<\sim 20h^{-1}\mathrm{Mpc}$) galaxy clustering analysis of a set of LRGs that are selected from DESI imaging data in the redshift range of $0.4 < z < \sim 0.9$.

The sample selection is motivated by and intended to mimic the DESI LRG selection. We compute accurate photometric redshifts (photo-z's) and error estimates using the DECaLS $g/r/z$ and WISE $W1/W2$ imaging data, and we use the photo-z's to measure the projected correlation functions in five redshift bins. We interpret the results in the halo occupation distribution (HOD) framework, and we incorporate photo-z errors and their uncertainties in this analysis.

This paper is organized as follows. We describe the data and the LRG sample in section 3.2. We describe the photometric redshifts in section 3.3. We describe the clustering measurements in section 3.4 and modeling of the measurements in section 3.5. We discuss the results and conclude in section 3.6 and 3.7.

3.2   DATA

We use the publicly available imaging catalogs from the Dark Energy Camera Legacy Survey (DECaLS, Dey et al. 2019) DR7 for both sample selection and photometric redshift estimation. DECaLS is one of the DESI imaging surveys, and it provides imaging in $g/r/z$ bands with median 5σ depth of 23.72/23.27/22.22 for the fiducial DESI galaxy target (galaxy with an exponential disk profile with half-light radius of 0.45″). The source catalogs are constructed using the software package `the Tractor`[1] for source detection and photometry, and they also include WISE forced photometry in the 3.4 micron ($W1$) and 4.6 micron ($W2$) bands.

3.2.1   Sample selection

In the final DESI imaging dataset, each object on average is covered by 3 exposures in each of the three optical bands, and to ensure adequate depth and minimize the impact of cosmic rays we require that each object have at least 2 exposures in each optical band. We remove objects contaminated by nearby bright stars by applying masks as described

---

[1]http://thetractor.org

in section 3.2.2, and we avoid regions of high stellar density by removing the area within $|b| < 25.0$ (where b is the Galactic latitude).

To facilitate the process of dividing the footprint for jackknife resampling (see section 3.4.3), small "islands" of isolated coverage and areas the survey boundaries are removed. This is done by first dividing the footprint into Healpix pixels of area ~ 0.21 square degrees each (corresponding to $N_{side} = 128$). The pixels at the survey boundaries are removed, and then islands consisting of fewer than 100 pixels are also removed.

The photometry is corrected for Galactic extinction using the Galactic transmission values in the DR7 catalog. The LRG sample is selected with the following color and magnitude cuts:

$$(z - W1) > 0.8 \times (r - z) - 0.6 \tag{3.1a}$$

$$z < 20.41 \tag{3.1b}$$

$$r - z > (z - 17.18)/2 \tag{3.1c}$$

$$r - z > 0.9 \tag{3.1d}$$

$$(r - z > 1.15) \text{ OR } (g - r > 1.65) \tag{3.1e}$$

The cuts are shown in Fig. 7.

Equation 3.1a acts as a stellar-rejection cut, similar to the one presented in Prakash et al. (2016). It is shown in the left panel of Fig. 7. This selection relies on the fact that galaxies with old stellar populations have spectra which exhibit a peak at 1.6 micron (sometimes referred to as the "1.6 micron bump"); at higher redshift this bump causes an increased flux in the WISE W1 (3.4 micron) band. Therefore we can easily separate stars from redshifted galaxies with the $z - W1$ color. This cut allows us to achieve less than 1% stellar contamination in our sample, as verified using the much deeper and better-seeing HSC data (Aihara et al., 2018).

Equation 3.1b is an apparent magnitude limit for the sample, which is similar to that expected for DESI LRGs (cf. DESI Collaboration et al. 2016). Equation 3.1c is a "sliding" color-magnitude cut that imposes a redshift-dependent luminosity threshold on the sample, selecting the most luminous galaxies across the redshift range. The magnitude limit and

sliding cut are shown in the middle panel of Fig. 7.

This sliding cut is combined with the cuts in equations 3.1d and 3.1e, which are shown in the right panel of Fig. 7, to remove low-redshift ($z < \sim 0.4$) galaxies and select intrinsically red galaxies. These selection cuts yield roughly uniform comoving number density in the redshift range of $0.4 < z < \sim 0.8$.

3.2.2   Bright star masks

Objects near bright stars are likely to have inaccurate flux measurements due to contamination. Such contamination causes many objects to be selected as LRGs although their true fluxes do not satisfy the selection cuts. The inaccuracies in the WISE PSF modeling in DR7 make the bright star contamination a significant source of imaging systematics for the LRG sample. Another issue is that extremely bright stars produce imaging artifacts such as ghosts and diffraction spikes which are poorly modeled. Such artifacts in the optical imaging, which is used for source detection, causes spurious sources. Therefore we apply masks surrounding the positions of bright stars for both optical and WISE imaging when constructing the LRG sample.

Three different sets of masks are used. First, we use the "bright-star-in-blob" column in the catalog. As defined in the DR7 catalog, a blob is a "contiguous region of pixels above a detection threshold and neighboring pixels" [2] , and an object is flagged if it is in the same blob as a Tycho-2 star (Høg et al., 2000). Second, we use an updated version [3] of the unWISE masks from Meisner et al. (2017) to remove areas around bright stars in AllWISE (Cutri et al., 2013) and 2MASS (Skrutskie et al., 2006). Third, we develop and apply a set of WISE masks that include fainter AllWISE stars that are not in the unWISE masks but still cause significant contamination. The third set of masks is specifically optimized for the LRGs. More about the WISE masks can be found in Appendix C. The three sets of masks combined remove $\sim 12\%$ of the objects from the LRG sample but only $\sim 4\%$ of the total area; it is clear that most of the sources masked do not truly belong in the sample.

In addition to the bright star masks, we also remove regions that are affected by very

---

[2]http://legacysurvey.org/dr7/description/#glossary
[3]http://catalog.unwise.me/catalogs.html
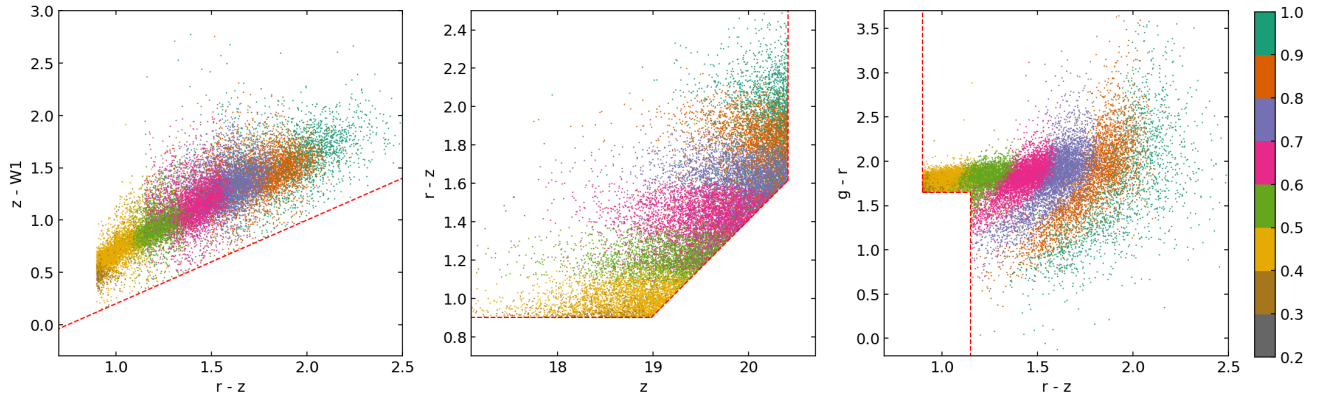
Figure 7: Color-color and color-magnitude diagrams for 20,000 objects randomly selected from the LRG sample. The points are color-coded according to their photometric redshifts (see section 3.3). The dashed lines represent the selection boundaries listed in equations 3.1a to 3.1e. The first panels shows the stellar-rejection cut using $z - W1$ color. The second panel shows the sliding color-magnitude cut and the z-band magnitude cut. The third panels shows the cuts that remove low-redshift ($z < \sim 0.4$) objects.
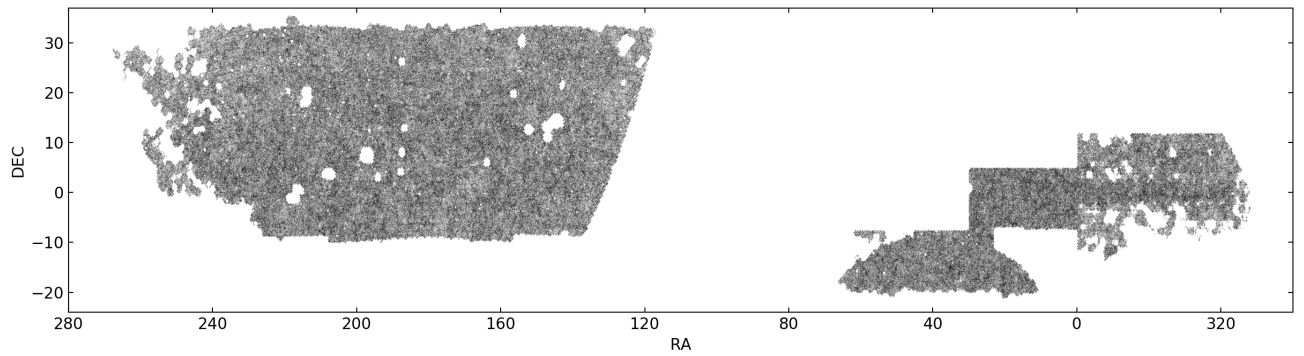
Figure 8: Sky coverage of the final LRG sample that is used in the clustering analysis. The grayscale represents the surface density. The "holes" in the NGC footprint and parts of the SGC footprint have been removed from the sample due to contamination from very bright stars or other known imaging artifacts.

39

bright stars or other imaging artifacts. We identify such regions by examining areas with a high density of LRGs that have very large (> 0.05) estimated photo-z errors. Since real LRGs typically have much smaller photo-z errors, these objects are mostly either spurious sources or real sources that are not included in the photo-z training such as stars and quasars; however, only the former are likely to be highly concentrated on the sky (e.g., around very bright stars). Such concentrations are identified efficiently with the DBSCAN routine in scikit-learn (Pedregosa et al., 2011) and the corresponding Healpix pixels are flagged as bad regions.

The final LRG sample has 2.74 million objects spanning 5655 square degrees. Fig. 8 shows the sky distribution.

3.2.3 Randoms

The calculation of correlation functions requires uniformly distributed random points with the same survey geometry as the LRG sample. We use the publicly available random catalog for DECaLS DR7 [4]. The same number of exposure requirements, footprint cuts, and bright star masks are applied on the randoms as are used in constructing the LRG sample.

3.3   PHOTOMETRIC REDSHIFTS

We compute photometric redshifts using the random forest regression method (Breiman, 2001), a machine learning (ML) algorithm based on decision trees. For our dataset, the ML methods have several advantages over template-fitting methods: there are abundant spectroscopic observations of galaxies covering the magnitude and color space of the LRG sample that can be used for training, and in this regime ML methods consistently outperform template-fitting methods; ML methods can trivially incorporate non-photometry information such as galaxy shapes, which we exploit here; and ML methods do not require physical and representative SED templates, which are not trivial to obtain especially for

---

[4]http://legacysurvey.org/dr7/files/

the wavelength range of the WISE pass-bands. Among the numerous ML methods, random forest provides good performance and is very computationally efficient, so we use it here.

3.3.1 Imaging data

We include r-band magnitude as well as $g - r$, $r - z$, $z - W1$ and $W1 - W2$ colors as inputs. The photometry has been corrected for Galactic extinction. Soo et al. (2018) showed that while morphological information only provides mild improvements in photo-z accuracy when full $ugriz$ photometry is available, the improvement is substantial when only grz photometry is available. Motivated by that result, we include as inputs three morphological parameters: half-light radius, axis ratio (ratio between semi-minor and semi-major axes), and a "model weight" that characterizes whether a galaxy is better fit by an exponential profile or a de Vaucouleurs, similar to the definition in Soo et al. (2018):

$$p = \frac{d\chi^2_{deV}}{d\chi^2_{deV} + d\chi^2_{exp}};$$ (3.2)

where $d\chi^2$ is the difference in χ^2 between the model fit and no source. The inclusion of the three morphological parameters reduces the photo-z scatter (NMAD) by $\sim 19\%$ and the 10% outlier fraction by $\sim 42\%$ for objects with $z_{mag} < 21$ in the training set.

3.3.2 Redshift "truth" dataset

For machine learning photo-z methods, redshift "truth" values are needed for the training process. Various redshift surveys overlap with the DECaLS footprint, and we compile a redshift truth dataset using spectroscopic and many-band photometric redshifts from ten different surveys.

3.3.2.1 2dFLenS The 2-degree Field Lensing Survey (Blake et al., 2016) is a spectroscopic survey performed at the Anglo-Australian Telescope, with a magnitude limited sample of $17 < r < 19.5$ and an LRG sample. We apply the following quality cuts to this sample:

$$(Q == 4) \text{ AND } (z > 0),$$ (3.3)

where Q is the quality flag.

3.3.2.2 AGES The AGN and Galaxy Evolution Survey (Kochanek et al., 2012) is a spectroscopic survey performed with the Hectospec instrument at the MMT telescope. Targets were selected with optical and IR imaging down to $I \simeq 20$ (Vega magnitude). Only objects from the galaxy targets are used, and we required $z > 0$.

3.3.2.3 COSMOS2015 photo-z's The COSMOS20105 catalog (Laigle et al., 2016) is a photometric redshift catalog covering the 2deg^2 COSMOS field. To select objects with accurate photo-z's, we apply the following quality cuts, motivated by the cuts applied in Tanaka et al. (2018):

1. FLAG_PETER is false (no bad photometry)
2. TYPE == 0 (only galaxies)
3. (ZPDF_H68 − ZPDF_L68)/(1 + z) < 0.02 (limit photo-z errors to 1%)
4. (CHI2_BEST < CHIS) AND (CHI2_BEST/NBFILT < 5) (fits are reasonable and better than stellar alternatives)
5. ZP_2 < 0 (no secondary peaks)
6. MASS_MED > 7.5 (stellar mass recovery successful)
7. DEC > 1.46 (removing some apparent imaging artifacts near the lower boundary)
8. z > 0.006 (remove the lowest redshift bin)
9. z < 3 (redshift upper limit)

3.3.2.4 DEEP2 DEEP2 (Newman et al., 2013) is a spectroscopic redshift survey performed with the DEIMOS instrument on the Keck telescope. Targets were selected down to $R_{AB} = 24.1$ with color cuts to exclude $z < 0.7$ galaxies in 3 of the 4 fields surveyed. We require that $z > 0$ and the quality flag ZQUALITY ≥ 3.

3.3.2.5 GAMA DR3 The Galaxy And Mass Assembly (GAMA) survey (Baldry et al., 2018) is a spectroscopic survey performed at the Anglo-Australian Telescope with magnitude

limited target selection down to $r \simeq 20$. We require that the quality flag nQ == 4 and $z > 0.002$.

3.3.2.6 OzDES OzDES is a spectroscopic follow-up survey (Childress et al., 2017) of the DES (Collaboration et al., 2016) supernova fields performed at the Anglo-Australian Telescope. Various types of targets were selected, such as supernova hosts, AGNs and LRGs. For our purposes, we only use objects that were targeted as "LRG", "bright galaxy", "ELG", "photo-z", "RedMaGiC" or "cluster galaxy". We also require that the quality flag Q == 4 and $z > 0$.

3.3.2.7 SDSS DR14 We use spectroscopic redshifts from Sloan Digital Sky Survey (SDSS) DR14 (Abolfathi et al., 2018), including the SDSS Main Galaxy Sample (Strauss et al., 2002), Baryon Oscillation Spectroscopic Survey (BOSS) sample (Dawson et al., 2013), and the Extended Baryon Oscillation Spectroscopic Survey (eBOSS) sample (Dawson et al., 2016). To select objects with accurate photo-z's, we apply the following quality cuts:

1. **ZWARNING** == 0 (no known problems)

2. **CLASS** == **GALAXY** (classified as galaxy)

3. $z > 0.0003$ (remove spurious galaxies at very low redshift)

3.3.2.8 VIPERS The VIMOS Public Extragalactic Redshift Survey (Scodeggio et al., 2018) is a spectroscopic survey performed at the ESO VLT. The sample is magnitude limited to $i = 22.5$ with color cuts to exclue $z < 0.5$ galaxies. To ensure redshift quality, we require $3.4 \leq$ **zflg** < 5 where **zflg** is the quality flag, and $z > 0$.

3.3.2.9 VVDS The VIMOS VLT Deep Survey (Le Fevre et al., 2013) is a spectroscopic survey performed at the ESO VLT. The sample is i-band selected, down to $i = 22.5$ in the wide field and $i \simeq 24$ in the deeper field. We require that the quality flag **ZFLAGS** == 4 and $z > 0$.

3.3.2.10 WiggleZ The WiggleZ Dark Energy Survey (Parkinson et al., 2012) is a spectroscopic survey performed at the Anglo-Australian Telescope that aims to measure the baryon acoustic oscillations (BAO) signal with emission-line galaxies. We require that the quality flag $Q == 4$ or 5, and we also require $z > 0$.

3.3.3 Combined truth dataset and downsampling

The redshift catalogs are cross-matched to DECaLS with a search radius of $1''$. Fig. 9 shows the redshift distribution of the cross-matched redshift truth dataset. Table 7 lists the number of objects from each survey.

Most of the truth objects are from four surveys: SDSS, BOSS, GAMA and WiggleZ. These surveys either apply specific color selections (BOSS, WiggleZ) or are limited to shallow magnitudes (SDSS Main Galaxy Sample, GAMA). This causes sharp peaks in the redshift distribution and discontinuities in color and magnitude space. To make the training sample more uniform and also to speed up computation, objects from these four surveys are downsampled. Downsampling is based on the object density in the 2-dimensional space of r-band magnitude vs. redshift, with a bin size of $\Delta z = 0.01$ and $\Delta r_{\mathrm{mag}} = 0.01$. For regions in the r_{mag}-redshift space where the density (number of objects in each r_{mag}-redshift bin) is higher than a specific threshold, the objects in that regions are randomly downsampled so that the density is reduced to the threshold level. This way we reduce the overall number of galaxies while preserving a good sampling of galaxies over the full range of luminosity, in particular retaining the most luminous galaxies, many of which are LRGs. The thresholds are 400, 400, 70 and 20 for SDSS, BOSS, GAMA and WiggleZ respectively. The redshift distribution of the downsampled truth dataset is shown in Fig. 9. Hereafter, we refer to the downsampled truth catalog simply as the truth catalog.

3.3.4 Random forest method

We compute photo-z's using the random forest regression routine in Scikit-Learn (Pedregosa et al., 2011). As we have described previously, we use the following eight parameters as input: r-band magnitude, $g - r$, $r - z$, $z - W1$ and $W1 - W2$ colors, half-light radius, axis
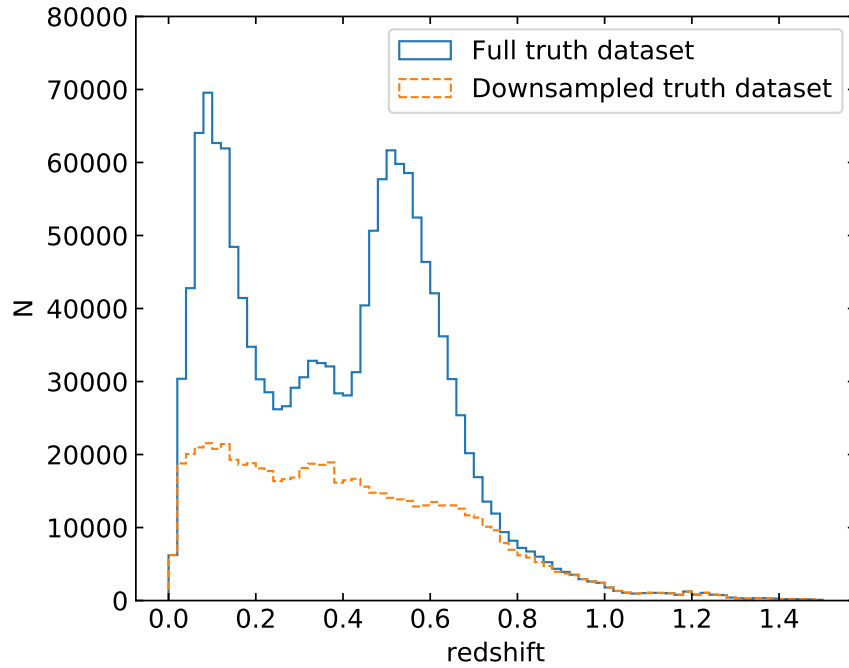
Figure 9: Redshift distribution of the redshift truth dataset. N(z) is the total number of objects in each $\Delta z = 0.02$ bin. The peaks at $z = 0.1$ and $z = 0.5$ in the full set are attributed to the SDSS Main Galaxy Sample and BOSS, respectively, both of which are downsampled significantly to avoid biasing the output photo-z's to favor these redshifts.

Table 7: Number of objects from each redshift survey that are cross-matched to DECaLS.

Survey	Full dataset	Downsampled dataset
BOSS	678370	224345
SDSS	449386	186666
WiggleZ	122907	47334
GAMA	109790	55990
COSMOS2015	53973	53972
VIPERS	44175	44175
eBOSS	23549	23549
DEEP2	15994	15994
AGES	11235	11235
2dFLenS	8102	8102
VVDS	5490	5490
OzDES	1407	1407

ratio and shape probability. For the random forest, we set the number minimum number of samples required to split an internal node at 25, which allows us to assign weights to the training objects.

The redshift and magnitude distributions of the photo-z training sample are not uniform due to the various selections of the spectroscopic surveys. In the presence of photometric errors, the gradients in the color and magnitude distributions cause objects in higher density regions in the multi-dimensional color/magnitude space to be scattered into lower density regions. Therefore in the neighborhood of each point in the color/magnitude space, it is more likely to find objects from higher density locations, and since colors and magnitudes are correlated with redshift (which is why photo-z algorithms work), this causes the photo-z estimates to be biased towards the redshifts of objects in higher density regions in the parameter space. Such bias is particularly significant at the high-redshift end of the redshift distribution, where the photo-z estimates are consistently biased low. To mitigate this bias, we assign weights to each training object based on its redshift: the weight is proportional to the inverse of the number of training objects at that redshift (with a cut-off value to prevent excessively large weights). As a result, objects at very low or very high redshifts are assigned larger weights than other objects.

We randomly select 90% of the truth dataset for training, and reserve the other 10% for testing purposes. To estimate the photo-z error for each object, we perturb the photometry by adding to the observed flux in each band a random value from Gaussian distribution whose standard deviation is set by the photometric error. This is similar to Kind & Brunner (2013), although in that work the photometry of the training sample, rather than the target sample, is perturbed. For each of the 50 individual trees in the random forest that we generated, we repeat the perturbation 20 times. The mean and standard deviation of the resulting 1000 (50×20) redshift estimates are used as the photo-z and photo-z error, respectively. Note that the photometric noise is only added when computing the final photo-z's used for clustering analysis; the random forest is trained with the original unperturbed photometry.

3.3.5 Photo-z performance for LRGs

Here we describe the photo-z performance for our LRG sample. For the photo-z performance of the overall spectroscopic training sample, see Appendix D.

To assess the photo-z quality of the LRG sample, we cross-match the LRG sample to the truth catalogs in the multi-dimensional space of r-band magnitude and $g - r$, $r - z$, $z - W1$ and $W1 - W2$ colors; redshift information is not used in the matching. Each LRG is matched to the single nearest neighbor in the truth catalog, and we count the number of LRGs that each truth object is matched to. We use this number as the weight for the photo-z vs. spec-z plot in Fig. 10. We quantify the photo-z accuracy using the normalized median absolute deviation (NMAD), defined as $\sigma_{\mathrm{NMAD}} = 1.48 \times \mathrm{median}(|\Delta z|/(1 + z_{\mathrm{spec}}))$ where $\Delta z = z_{\mathrm{phot}} - z_{\mathrm{spec}}$. This is a robust estimator of scatter as it is not sensitive to outliers. We also measure the fraction of outliers defined as objects with $|\Delta z| > 0.1 \times (1 + z_{\mathrm{spec}})$. From the weighted spec-z objects, we estimate that the average photo-z scatter σ_{NMAD} for the LRG sample is 0.021 and the outlier rate is 1%. The weighted spec-z objects are also used for estimating the comoving number density which we use as an observable in our HOD modeling (see section 3.5).

3.3.5.1 Photo-z error estimates Our photo-z error estimation assumes that the photo-z errors are solely due to the photometric errors, and that the photometric error estimates are accurate. This ignores the effect of incompleteness in the training data and the uncertainties in the morphological values.

We validate the photo-z errors using objects with spectroscopic redshifts. Fig. 11 shows how well the real photo-z errors can be approximated by a Gaussian distribution with a width equal to the estimated photo-z error. We find that the real photo-z errors are roughly consistent with a Gaussian distribution, but the photo-z errors are generally overestimated by a factor which depends on the redshift range. Because we do not have representative spectroscopic data to estimate this scaling factor accurately, we treat it as nuisance parameter in the HOD modeling (see section 3.5.2).
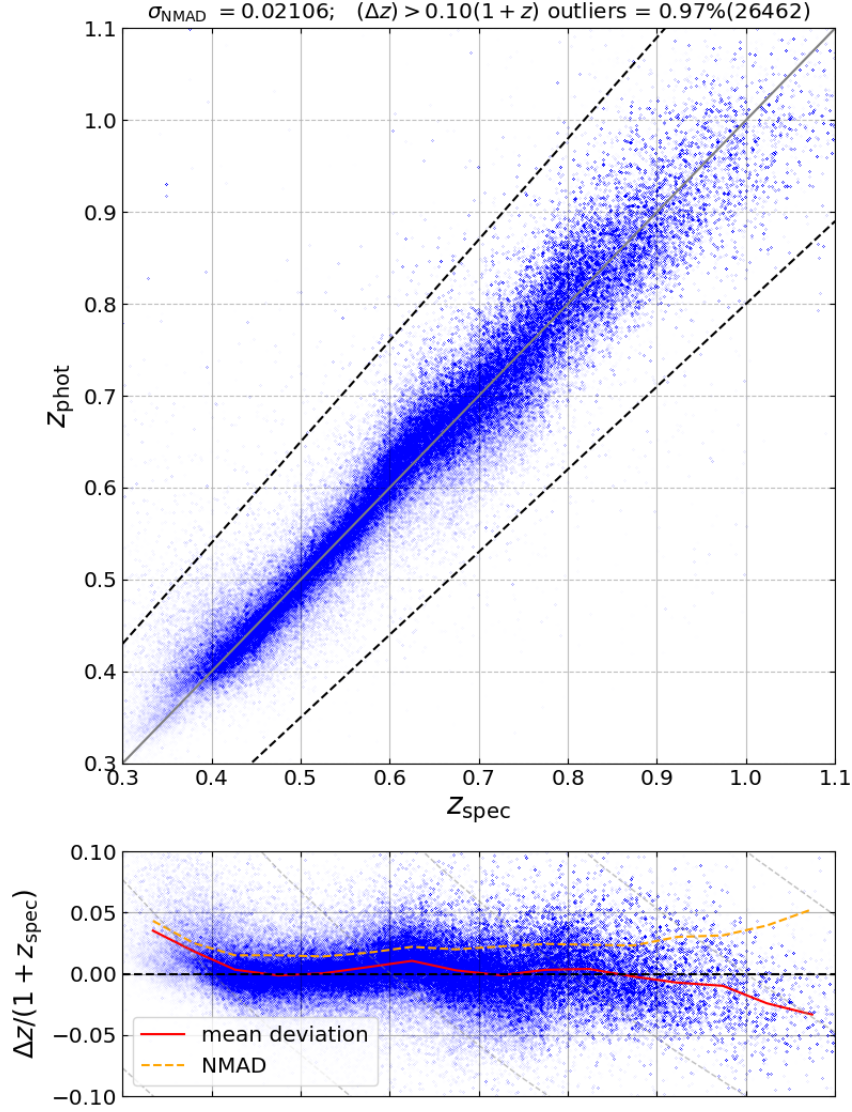
Figure 10: Top panel: Photo-z vs. spec-z for truth objects that are weighted to approximate the photo-z performance of the LRG sample. Lower panel: photo-z offset (in $\Delta z/(1 + z_{\mathrm{spec}})$ vs. spec-z; the red solid line and the yellow dashed line are the Hodges-Lehmann mean and NMAD, respectively, of the photo-z offset in bins of spec-z. The photo-z's are mostly well constrained with few outliers for this sample.
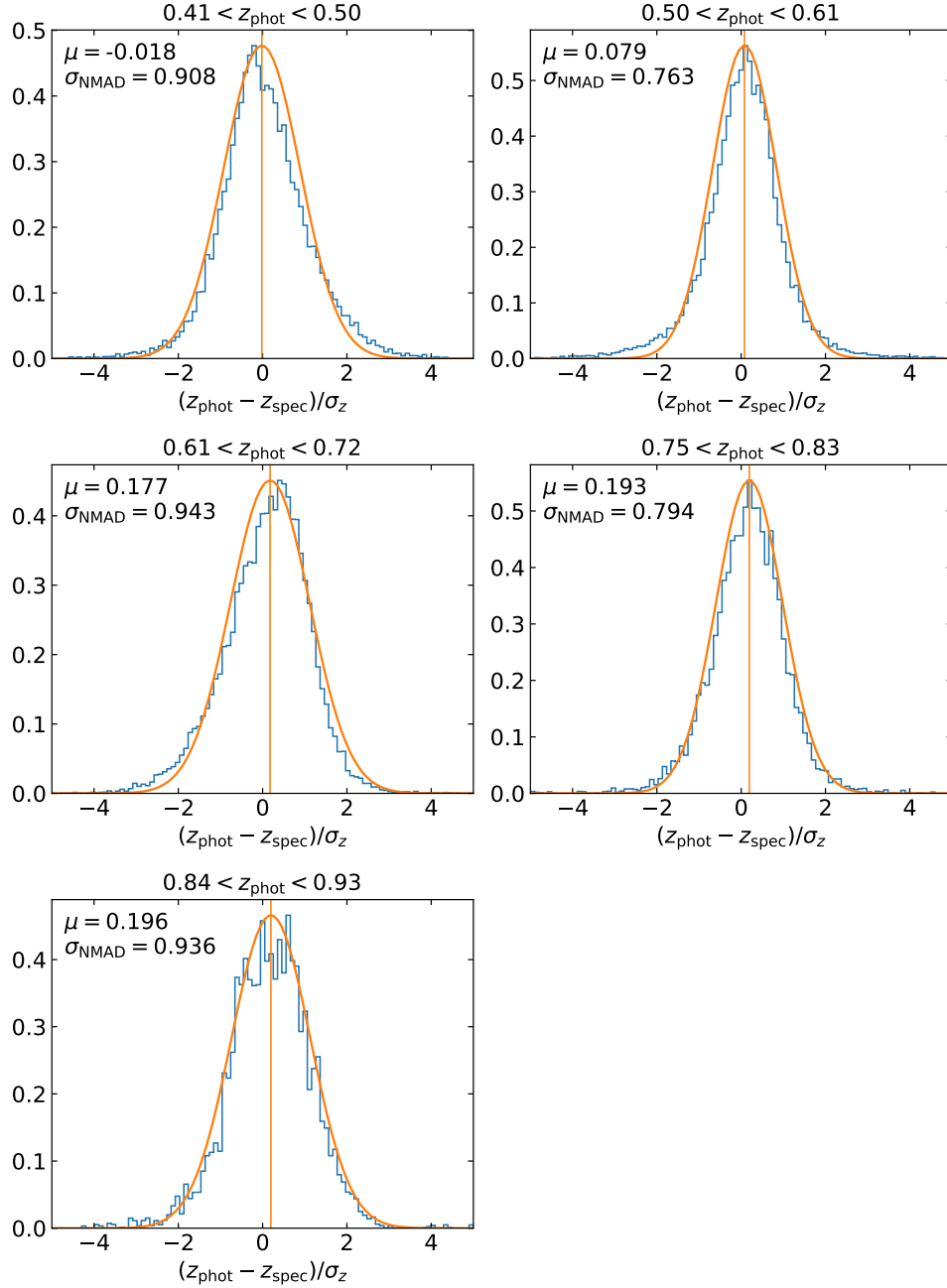
Figure 11: The distribution of $(z_{phot} - z_{spec})/\sigma_z$, where σ_z is the estimated photo-z error, in different redshift bins. Here μ (vertical line) and σ_{NMAD} (1-σ width of the curve) are the median and the normalized normalized median absolute deviation of the distribution, respectively, and the smooth curves show the corresponding Gaussian distributions. A non-zero μ value indicates that the photo-z's are biased, and any deviation of σ_{NMAD} from unity indicates over- or under-estimation of the photo-z errors. The fact that σ_{NMAD} values are consistently less than unity indicates that the our photo-z errors are over-estimated.

50

Table 8: The redshift bins. The second column lists the redshifts of the snapshots of the N-body simulation. The third column lists the comoving number densities in units of $h^3\mathrm{Mpc}^{-3}$; these values are used in the HOD fitting with 10% assumed Gaussian uncertainty.

Redshift	z_sim	$n(z)$
$0.41 < z_\mathrm{phot} < 0.50$	0.4573	6.32×10^{-4}
$0.50 < z_\mathrm{phot} < 0.61$	0.5574	6.16×10^{-4}
$0.61 < z_\mathrm{phot} < 0.72$	0.6644	6.15×10^{-4}
$0.75 < z_\mathrm{phot} < 0.83$	0.7787	4.41×10^{-4}
$0.84 < z_\mathrm{phot} < 0.93$	0.8594	2.14×10^{-4}

3.4   CLUSTERING MEASUREMENTS

3.4.1   Redshift bins

In order to study the redshift dependence of the sample properties, we divide the LRG sample into four photometric redshift bins of width $\Delta z \simeq 0.1$, covering the ranges [0.41, 0.5], [0.5, 0.61], [0.61, 0.72], [0.75, 0.83], [0.84, 0.93]. These bins have been chosen such that they are centered at the redshifts of the snapshots of the halo catalogs from the N-body simulation (see section 3.5). Fig. 12 shows the estimated comoving number density vs. redshift for the LRG sample; the shaded regions represent the redshift ranges for each bin. The volume-averaged comoving number densities for each bin are listed in Table 8. The densities estimated from photo-z's are consistent with the estimates from weighted spec-z's. Densities estimated using spec-z's weighted as described in section 3.3.5 are used in modeling.

Fig. 14 shows the redshift distribution (surface density) for each redshift bin estimated by convolving the photo-z's with their photo-z error.
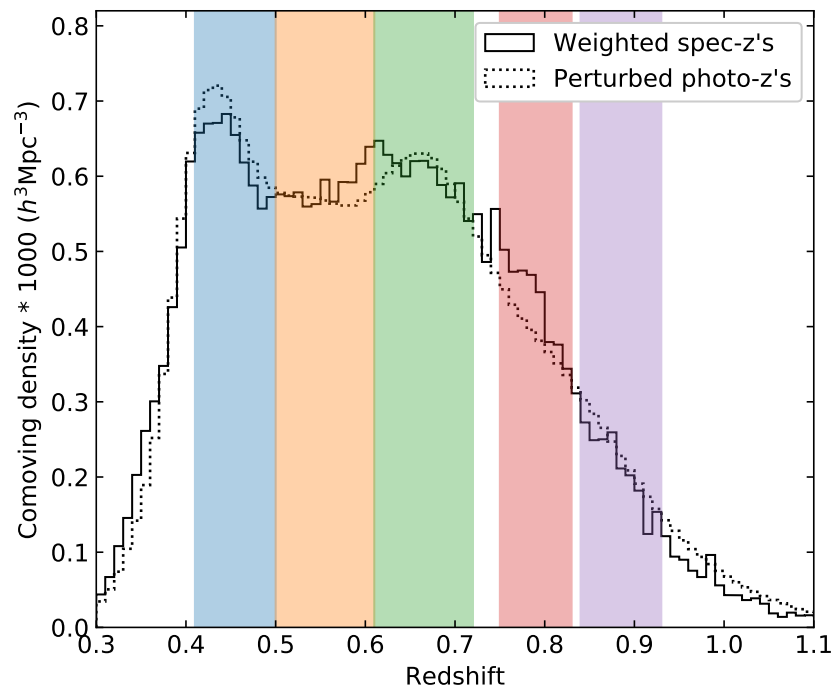
Figure 12: Redshift-dependent comoving number density of the LRG sample. The dashed line shows the densities estimated with photo-z's convolved by the estimated photo-z error. The solid line shows the densities estimated from the weighted spec-z's described in 3.3.5; these weighted spec-z' are also used for deriving the comoving number densities for the clustering analysis. The colored bands represent the redshift bins. The fact that the two lines are consistent with each other indicates that our comoving density estimates are relatively robust.

3.4.2 Projected correlation function

Ideally, one would like to measure the correlation function $\xi(r)$, the excess probability of finding a pair of galaxies separated by distance r, but the large uncertainty in radial distances precludes its direct measurement. For imaging datasets, it is common to measure instead the angular correlation function, typically in bins of photometric redshifts. However, in doing so the information on relative distances between galaxies contained in the photo-z's is not utilized. For spectroscopic datasets, due to the presence of redshift-space distortions, the small-scale clustering is usually measured with the projected correction function, effectively integrating out the effects of redshift-space distortions:

$$w_p(r_p) = \int_{-\pi_{max}}^{\pi_{max}} \xi(r_p, \pi) d\pi, \tag{3.4}$$

where $\xi(r_p, \pi)$ is the 3-D correlation function, r_p is the transverse distance and π is the line-of-sight distance.

Here, to make optimal use of the photo-z information, we measure the projected correction function (Equation 3.4), using distances derived from the photo-z's. We adopt a relatively large π_{max} of $150h^{-1}$Mpc to account for the large radial distance uncertainties from the photo-z's. This large π_{max} is comparable to the width of the redshift bins $(160-210h^{-1}$Mpc$)$. However, the photo-z errors cause many galaxy pairs to be lost due to one of the galaxies being outside of the redshift bin in a generic auto-correlation measurement, thus complicating the modeling and resulting in a lower clustering signal-to-noise. To address this issue, instead of counting pairs between a redshift bin and itself (i.e., measuring auto-correlation), we count pairs between galaxies in a redshift bin and objects in a wider bin centered at the same redshift. The second redshift bin extends the first bin by π_{max} in both directions so that for all galaxies in the first bin, all their pairs within π_{max} will be counted. More importantly, this "padded" auto-correlation approach decouples the clustering measurement from the boundary effects of the redshift bin, and thus it significantly simplifies the interpretation and modeling of the measured correlation function using simulations with periodic boundary conditions.

To compute this "padded" $w_p(r_p)$, we adopt the cross-correlation form of the Landy-Szalay

estimator (Landy & Szalay, 1993):

$$w_{\mathrm{p}}(r_{\mathrm{p}}) = 2\pi_{\max} \times \frac{(D_1 D_2 - D_1 R_2 - D_2 R_1 + R_1 R_2)}{R_1 R_2}, \tag{3.5}$$

where each term denotes the pair count between two samples; D_1 denotes the data in a redshift bin defined in section 3.4.1 and D_2 denotes the data in the wider redshift bin; and R_1 and R_2 denote sets of random points with the same angular and redshift distribution as D_1 and D_2, respectively. The redshifts of the randoms are randomly drawn from the redshifts of the data, so they have the same redshift distribution as the data, by construction. The measurement is done using the `TreeCorr` package (Jarvis et al., 2004). We tested this estimator on mocks that resemble our redshift bins, and we confirmed that it produces the same $w_{\mathrm{p}}(r_{\mathrm{p}})$ as that for mocks in a cubic volume with periodic boundary conditions using the simple auto-correlation estimator.

We measure $w_{\mathrm{p}}(r_{\mathrm{p}})$ in 12 logarithmically-spaced bins covering the range from $0.11h^{-1}\mathrm{Mpc}$ to $19.5h^{-1}\mathrm{Mpc}$ (comoving). We also made measurements at smaller and larger scales, but these measurements were not used for the modeling. Fig. 13 shows the measured projected correlation functions for the five redshift bins. The two bumps, corresponding to the one-halo (from galaxy pairs within the same dark matter halo) and two-halo (from galaxy pairs in two different halos) regimes of the correlation function, are clearly visible in all the redshift bins. It should be noted that the photo-z errors effectively smooth out sharp features in the radial direction, and as a result these $w_{\mathrm{p}}(r_{\mathrm{p}})$ measurements using photo-z's have lower amplitude than the intrinsic clustering signal that one can measure with spectroscopic redshifts.

As shown in Fig. 14, the sample in each redshift bin does not contain all the objects in that redshift range, and it also includes objects whose true redshift is in other bins.

3.4.3 Jackknife resampling and covariances

We compute the covariance matrices of correlation functions with jackknife resampling: we divide the footprint into N_{sub} subregions, and we resample the dataset with one of the subregions removed. There are a total of N_{sub} resampled datasets, and the correlation function
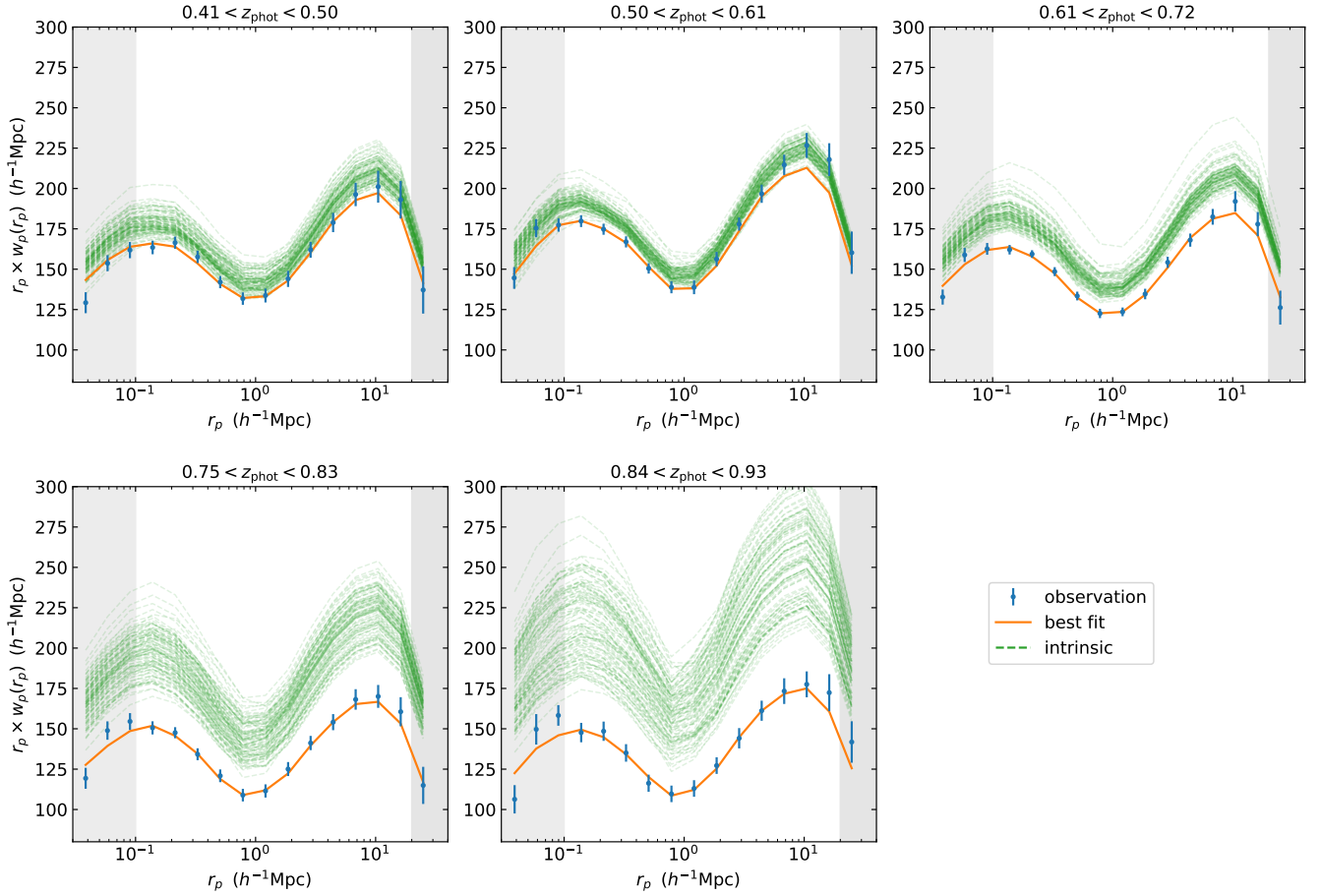
Figure 13: The projected correlation function multiplied by the transverse distance. The points are measurements with error bars from jackknife. The points in the gray shaded area are not used for modeling to avoid possible systematics. The orange curve is the best fit from HOD modeling. The green band is the [16th, 84th] percentile range of the intrinsic clustering signal, i.e., the clustering that would have been measured according to the fit parameters if perfect distance measurements (rather than photo-z's) were available. The larger uncertainty in the intrinsic clustering in the higher redshift bins is mostly due to the larger photo-z errors for them.
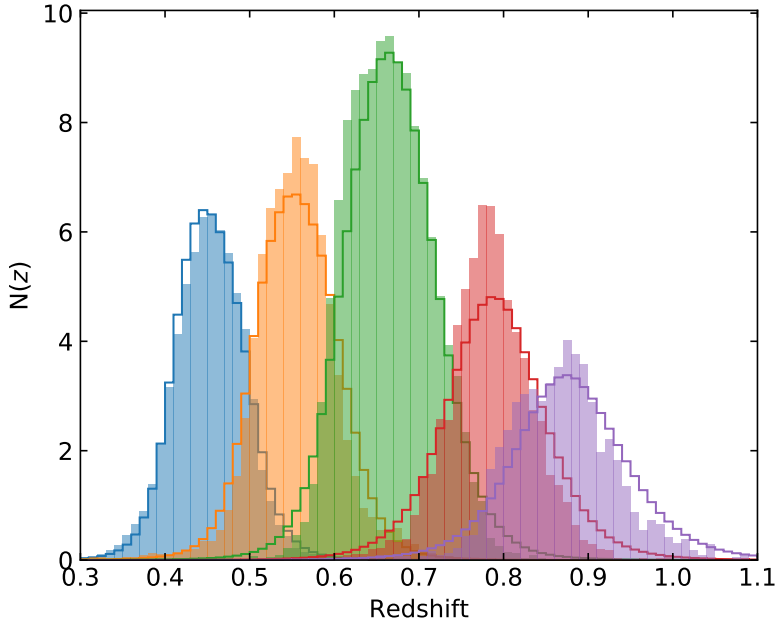
Figure 14: The estimated redshift distributions (surface density in redshift bins) of the LRG sample. The y-axis is the number of objects per square degree in the redshift bin of width 0.1. The filled histograms show the redshift distributions estimated from weighted spec-z objects. The unfilled histograms are distributions of stacked photo-z's that are convolved with photo-z errors. The samples in different redshift (photo-z) bins overlap due to photo-z errors. Note that (1) we use the original photo-z error estimates, which as seen in Fig. 11, are probably overestimated; and 2) simply stacking the photo-z probabilities produces broader redshift distributions than the mathematically correct procedure (Malz et al., in prep.).

is measured for each one. The covariance matrix is given by

$$\text{Cov}(w_i, w_j) = \frac{(N_{\text{sub}} - 1)}{N_{\text{sub}}} \sum_{l=1}^{N_{\text{sub}}} \left(w_i^l - \overline{w}_i\right) \left(w_j^l - \overline{w}_j\right), \tag{3.6}$$

where w_i^l is the projected correlation function at the i-th distance bin measured from the l-th jackknife sample, and $\overline{w}_i$ is the mean from all jackknife samples.

The DECaLS survey was not yet completed by DR7. This, combined with the masks and quality cuts, results in the irregular survey geometry, making it difficult to manually divide the footprint into compact subregions with equal areas. To solve this problem, we developed an automated routine. The relevant Python codes can be found online [5] . The routine involves three steps:

1. The objects (in our case randoms) in the survey footprint are divided into Healpix pixels. This significantly reduces the number of points and speeds computation;

2. Initial grouping of the Healpix pixels is performed using a clustering algorithm (specifically, we use k-means clustering; see Hartigan & Wong 1979) with the object count in each pixel as weights to account for fractional occupation of the pixels;

3. We randomly switch the group labels of boundary pixels and check if the changes improve a score that favors the uniformity of the areas of the subregions as well as their compactness. We repeat this step until the desired score is achieved.

Applying this procedure, we divide the footprint into 120 jackknife subregions of 47.1 square degrees each (within $\sim 2\%$ variation), shown in Fig. 15. The areas of the subregions are uniform to $\sim 1\%$. The area of the subregions is large enough to cover the entirety of angular scales of interest, and small enough to produce enough subregions to compute covariance matrices accurately. The size of each subregion is much larger than the largest angular scale of ~ 1 degree in the correlation function, therefore the jackknife resampling accounts for cosmic variance in addition to shot noise and imaging systematics.

---

[5] https://github.com/rongpu/pixel_partition
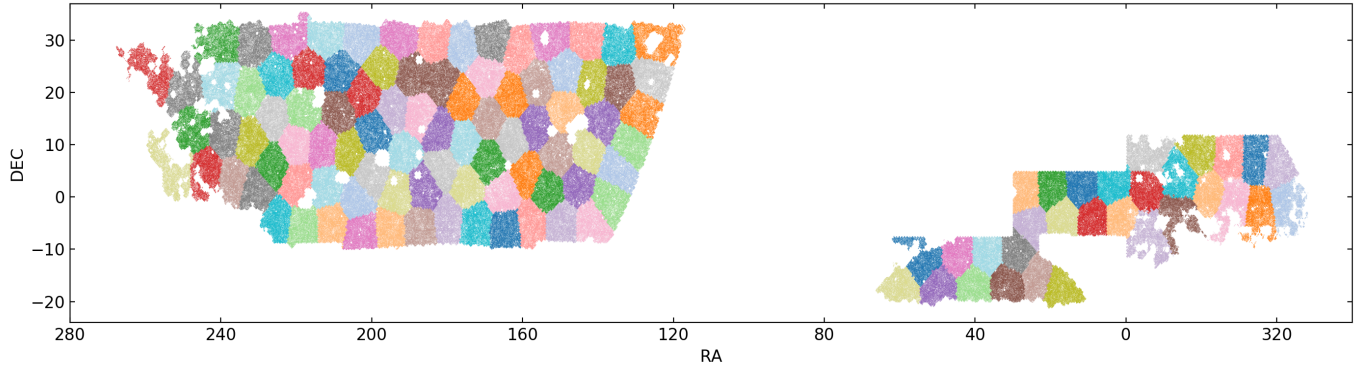
Figure 15: Sky distribution of the LRGs with color coding to show the 120 subregions for jackknife resampling. Note that nonadjacent "patches" with the same color are different subregions. Each subregion has the same area (within ∼ 2% variation) and is compact by design.

3.5 MODELING

In this section we present our analysis on galaxy-halo connection for the LRG sample using the HOD framework. The galaxy-halo connection determines the clustering properties of the galaxy sample, such as the large-scale bias — which is useful for forecasting DESI BAO constraints — and can be used for creating mock galaxy catalogs which can be used for estimating the covariances. In this work we fix the cosmological parameters and only allow the HOD parameters to vary, but in principle the method presented here can be incorporated into a more flexible modeling framework that constrains both cosmology and galaxy-halo connection parameters, and applied on data from future imaging surveys such as LSST.

3.5.1 HOD model

We model the clustering measurements in the HOD framework (e.g., see Berlind & Weinberg 2002 which also lists earlier literature on HOD; see also Wechsler & Tinker 2018 for a

more general review on galaxy-halo connection), which is widely used to model luminosity-threshold galaxy samples. In this framework, dark matter halos from N-body simulations are populated by central and satellite galaxies with a probabilistic prescription. In its basic form which we have adopted, the central galaxy probability (denoted by N_{cen}) and the mean number of satellite galaxies (denoted by N_{sat}) for a given a halo are determined solely by the halo mass. There are several slightly different mathematical prescriptions, and we adopt the one in Zentner et al. (2019); we briefly summarize it below.

The central galaxy probability is given by a step-like function

$$\langle N_{cen}|M_{vir}\rangle = \frac{1}{2}\left(1 + \mathrm{erf}\left[\frac{\log(M_{vir}) - \log(M_{min})}{\sigma_{\log M}}\right]\right), \tag{3.7}$$

where M_{vir} is the virial mass of the dark matter halo; M_{min} is the mass threshold above which halos are populated by central galaxies and $\sigma_{\log M}$ defines the smoothness of this transition;

The number of satellite galaxies in a halo follows the Poisson distribution with a mean given by a power law

$$\langle N_{sat}|M_{vir}\rangle = \left(\frac{M_{vir} - M_0}{M_1}\right)^\alpha, \tag{3.8}$$

where M_0, M_1 and α are free parameters of the HOD model. We impose that there are no satellite galaxies in halos with $M_{vir} < M_0$.

The spatial distribution of satellite galaxies follow the NFW profile (Navarro et al., 1997), with the scale radius R_s from the halo catalog. We ignore the effect of velocity dispersion on redshift since it is negligible compared to the photo-z error.

3.5.2 Mock galaxies

To constrain the HOD model parameters, we measure the clustering of mock galaxies generated from a set of HOD parameters and compare with our measurements from real LRGs. We use the halo catalog from the MultiDark Planck 2 (MDPL2) simulation (Klypin et al., 2016), which used Rockstar (Behroozi et al., 2013) to identify the halos. The MDPL2 simulation adopts Planck 2013 cosmology: $\Omega_m = 0.307115$, $\Omega_\Lambda = 1 - \Omega_m = 0.692885$, $\Omega_b = 0.048206$, $h = 0.6777$, $\sigma_8 = 0.823$, and $n_s = 0.96$. The size of the cubic simulation box is $1h^{-1}\mathrm{Gpc}$, and the mass resolution of $1.51 \times 10^9 h^{-1}M_\odot$. We designed the redshift bins of

the LRG sample so that they center at the redshifts of five snapshots of the simulation. The redshifts of the five snapshots are listed in Table 8. We use `halotools` (Hearin et al., 2017) for populating the halos with galaxies using the pre-defined Zheng et al. (2007) prescription (note that the $\langle N_{\mathrm{sat}} | M_{\mathrm{vir}} \rangle$ definition here is slightly different).

To emulate the effect of photo-z's on the clustering signal, we perturb the position of the galaxies along the line-of-sight direction, i.e., the direction along one of the axes of the simulation box. For each galaxy, this distance perturbation is drawn from a Gaussian distribution, the width of which is randomly drawn from the rescaled photo-z error estimates of the LRGs in the corresponding redshift bin. As discussed in section 3.3.5.1, the true photo-z errors differ from the estimated errors by a scaling factor S_z which we do not have good constraints on. Thus S_z is included in the model as a nuisance parameter. We use the `Corrfunc` software package (Sinha & Garrison, 2017) for measuring $w_{\mathrm{p}}(r_{\mathrm{p}})$ of the mock galaxies because it is better optimized for cubic boxes with periodic boundaries conditions.

3.5.3   MCMC sampling of parameters

The HOD model has five free parameters: $\log(M_{\mathrm{min}})$, $\sigma_{\log M}$, α, $\log(M_0)$, and $\log(M_1)$. Additionally, we have the nuisance parameter S_z to account for the uncertainties in the photo-z error estimation. We adopt flat priors for all these parameters, and the ranges for the priors are listed in Table 9. We set the lower limit of S_z at 0.6, which is much lower than values inferred from spectroscopic redshifts (see Fig. 11).

To obtain the posterior probability distributions of the HOD parameters, we perform Markov Chain Monte Carlo (MCMC) sampling using the emcee package (Foreman-Mackey et al., 2013). The likelihood function is $\mathcal{L} \propto e^{-\chi^2/2}$ and χ^2 is given by

$$\chi^2 = \Delta w_i \left[\mathrm{Cov}^{-1} \right]_{ij} \Delta w_j + \frac{\left(n^{\mathrm{meas}} - n^{\mathrm{mock}} \right)^2}{\sigma_n^2}, \tag{3.9}$$

where $\Delta w_i = w_p^{meas}(r_{\mathrm{p}}) - w_p^{mock}(r_{\mathrm{p}})$ is the difference between the measured projected correlation function and the one from the mocks at the i-th distance bin; Cov^{-1} is the inverse of the covariance matrix from jackknife (see section 3.4.3); n^{meas} and n^{mock} are the comoving number densities of the data and the mock, respectively; and σ_n is the uncertainty in the

60

Table 9: The ranges of the flat priors on model parameters.

Parameter	Prior Interval
$\log(M_{\mathrm{min}})$	[11.0, 14.0]
$\sigma_{\log M}$	[0.001, 1.5]
α	[0.0, 2.0]
$\log(M_0)$	[11.0, 14.0]
$\log(M_1)$	[11.5, 15.5]
S_z	[0.6, 1.4]

comoving number densities. The comoving number densities are estimated from the weighted spec-z objects as described in 3.3.5. We compare these density estimates with the densities estimated from the photo-z's, and the standard deviation of the differences in the five redshift bins is $\sim 7\%$. We adopt a larger density uncertainty of $\sigma_n = 10\%$ to account for any additional unknown systematics in the photo-z's.

3.6   RESULTS

The posterior distributions of the model parameters are shown in Fig. 16 and Fig. 17. The plots are made using a modified version of the `corner.py` software package (Foreman-Mackey, 2016). The mean, median and best-fit values of the parameters and the 16% and 84% percentiles are listed in Table 10. The first four redshift bins have very similar HOD parameters, indicating that the LRGs have similar host halo properties over the redshift range of $0.4 < z < 0.8$.

Fig. 18 shows the halo occupation functions. Fig. 19 shows the probability distributions of the host halo mass. In both figures, the solid lines are the best-fit results, and the dashed lines are for parameters randomly selected from the MCMC chains to show the possible range of halo occupations allowed by the data.
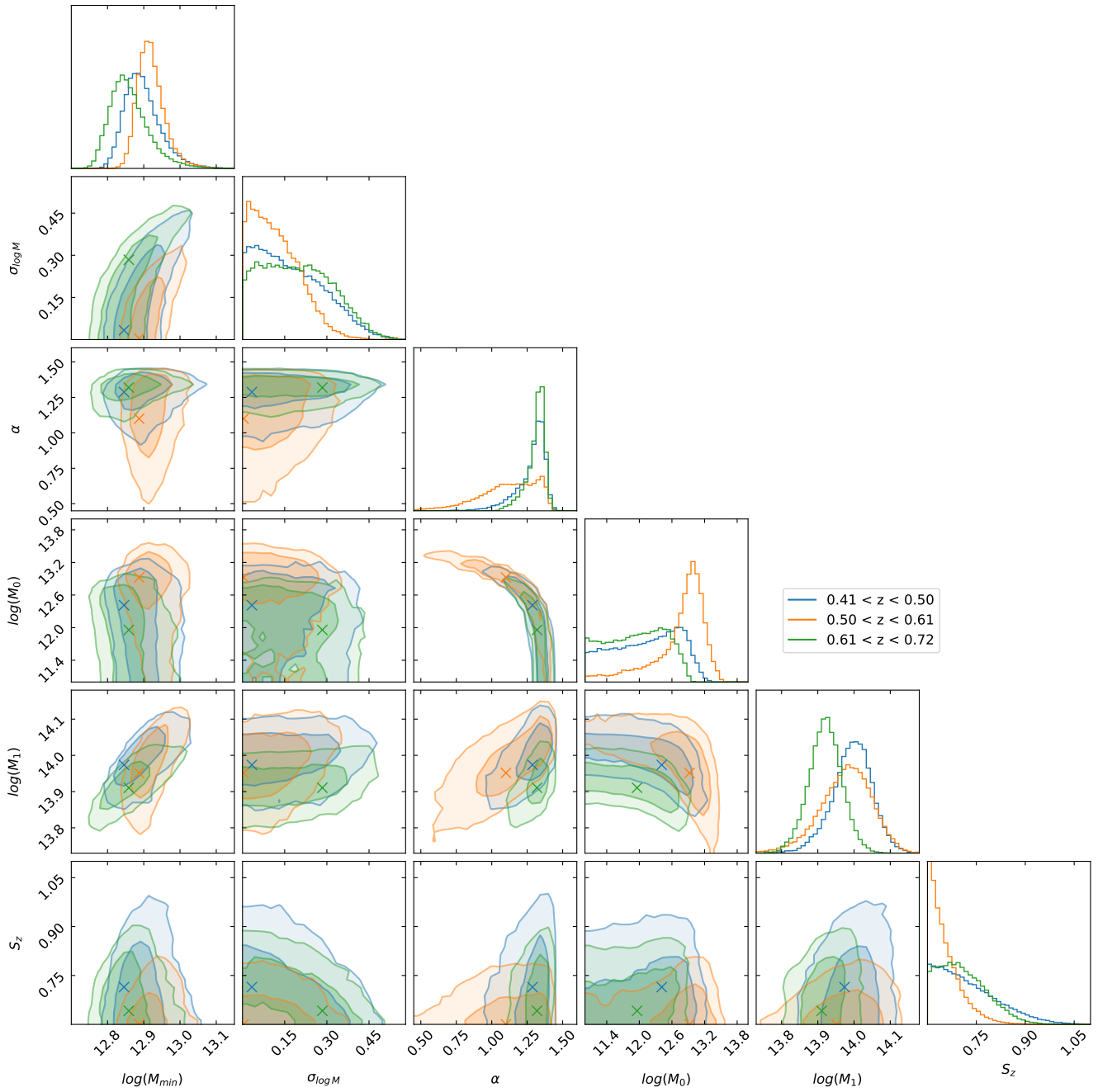
Figure 16: The one- and two-dimensional marginalized posterior probability distributions of the model parameters from MCMC for the first three redshift bins. The inner contour and outer contour are the 68% and 95% confidence regions, respectively. All parameters except S_z are HOD parameters; the parameter S_z is the scaling factor for the photo-z errors. The mass parameters are in units of $h^{-1}M_\odot$.
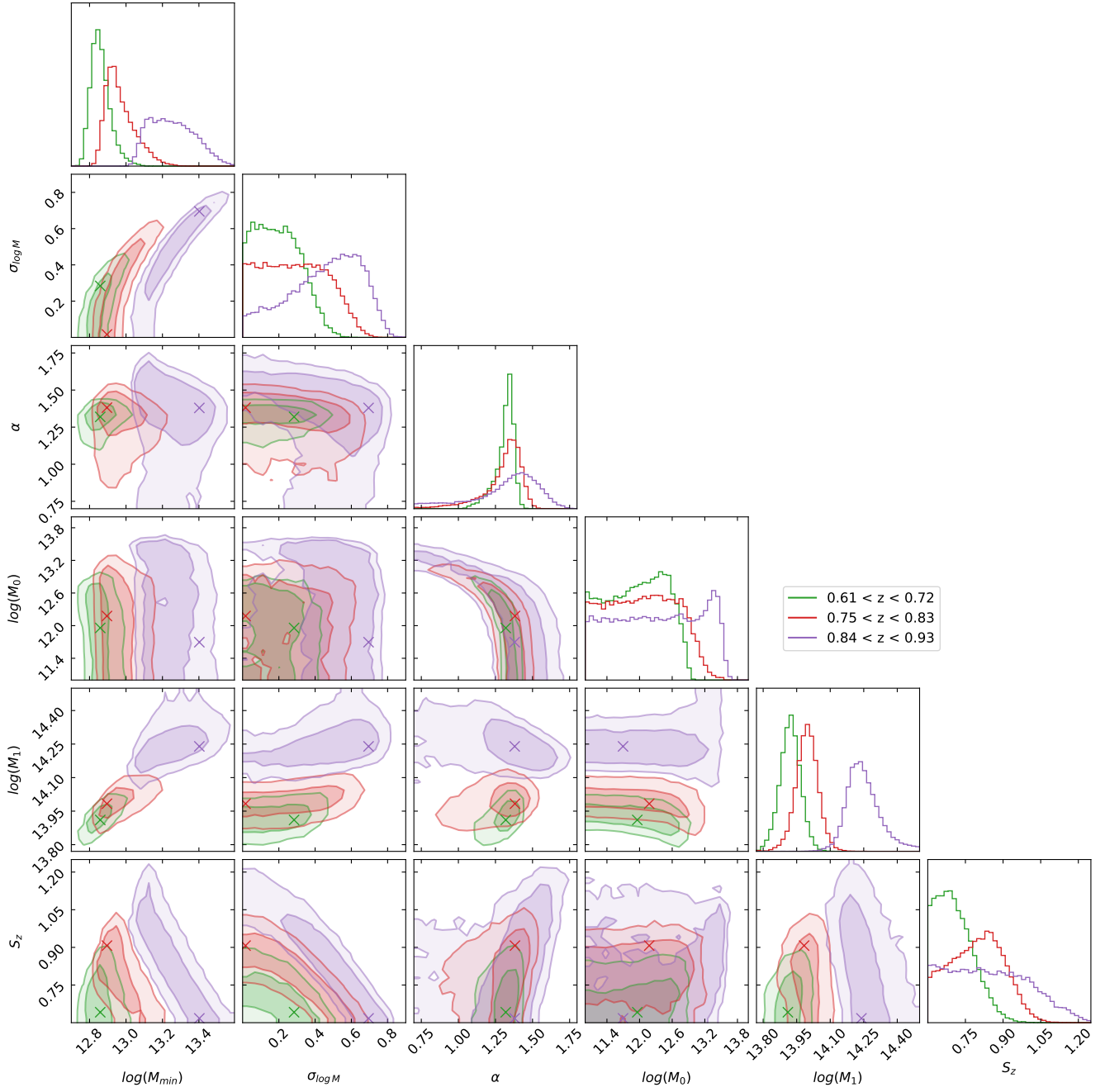
Figure 17: Same as Fig. 16, but for different redshift bins. We include the results of $0.61 < z < 0.72$ which is also shown in the previous plot as a reference.
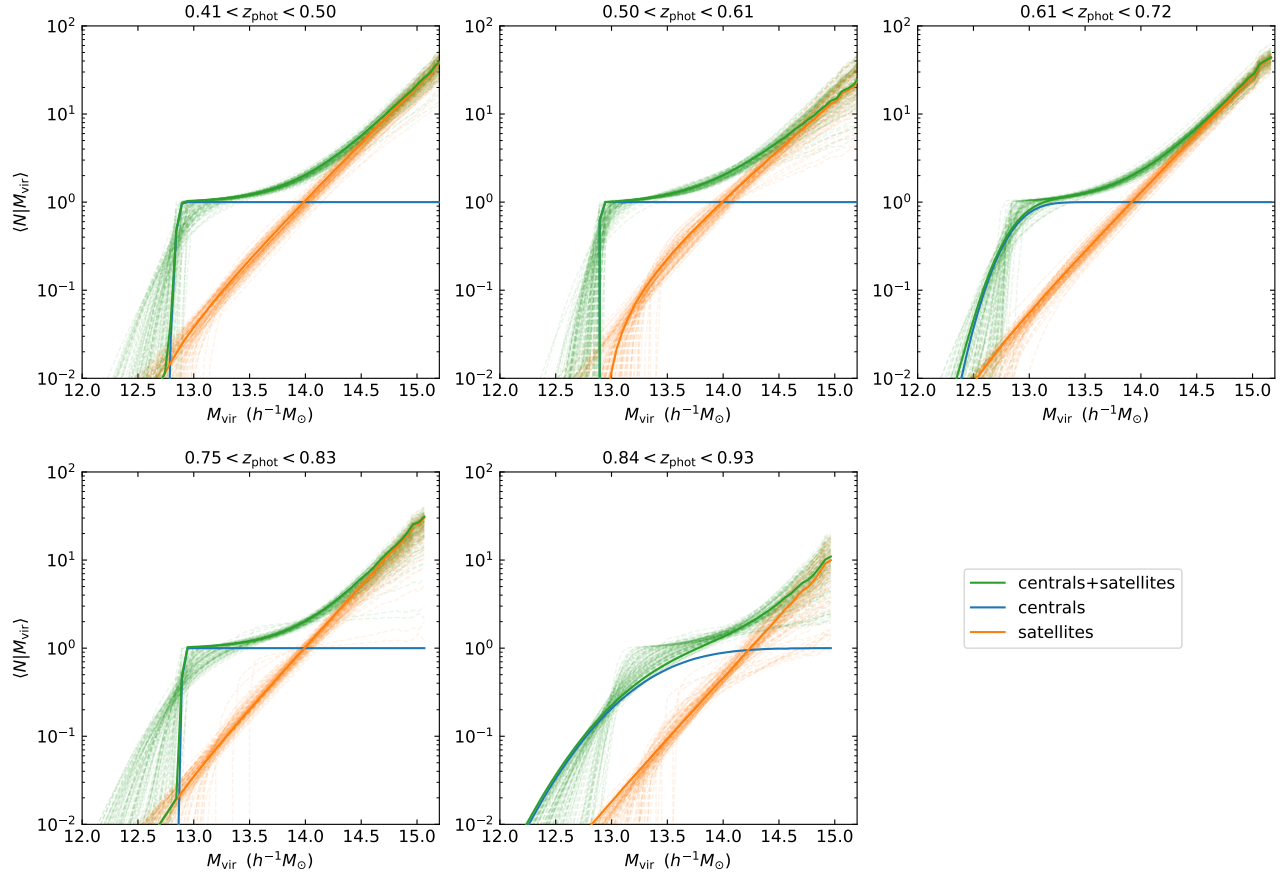
Figure 18: The halo occupations, i.e., the average number of galaxies that are hosted by a halo of a certain mass. The occupations of centrals, satellites and the full occupation are plotted separately. The solid lines are from the best-fit parameters. The dashed lines are from 100 sets of parameter randomly selected from the MCMC chain (only the satellite and full occupations are plotted for clarity).
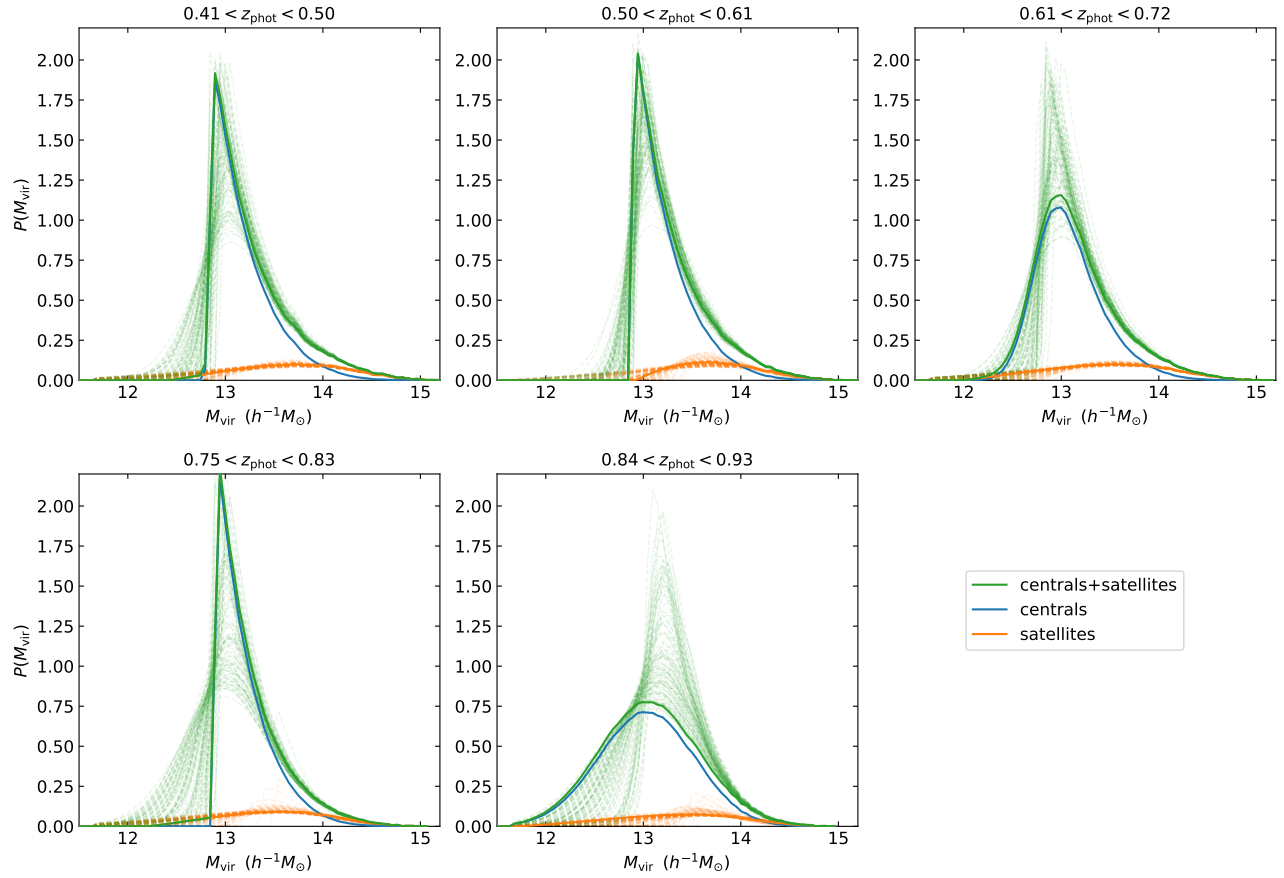
Figure 19: Similar to Fig. 18, but showing the distribution of host halo mass, with the solid lines showing the best-fit results and dashed lines showing parameters from the MCMC chain. The green curve shows the host halo mass distribution for all galaxies (centrals+satellites) normalized as the probability per $\log M$; the blue and orange curves show the central and satellite components.

The highest redshift sample has much larger contours on the model parameters than lower redshift samples. This could be due to a combination of several factors, including the larger photo-z errors at higher redshifts, a smaller sample size, and a broader redshift distribution that dilutes the clustering signal. Despite the larger errors, the differences in the model parameters between this and lower redshift samples are statistically significant. Such deviation is caused by the selection effect of the apparent magnitude limit (see the middle panel of Fig. 7): at redshifts higher than ~ 0.7, the luminosity-threshold established by the sliding cut is replaced by the apparent magnitude limit, and as a result more luminous galaxies are preferentially selected at higher redshift. This qualitative change of the sample at high redshift will need to be considered when analyzing and interpreting DESI spectroscopic data.

At lower redshifts where the photo-z errors are small, the HOD parameters are not sensitive to the photo-z error rescaling factor S_z, since most of the galaxies pairs are still within $\pi_{\mathrm{max}} = 150 h^{-1} \mathrm{Mpc}$ in the line-of-sight direction. At higher redshifts the photo-z errors are much larger, and the clustering signal from the mock galaxies is much more sensitive to the S_z, thus resulting in the strong correlation between some of the HOD parameters and S_z. Nevertheless, the value of S_z is poorly constrained by the data, although the posterior prefers $S_z < \sim 1$ at all redshift which is consistent with the results of the photo-z error validation with spectroscopic redshifts. There is strong degeneracy between S_z and galaxy bias, as shown in Fig. 20, which leads to large uncertainties in galaxy bias at high redshift. This degeneracy is expected, since stronger clustering signal could be due to a higher bias, or smaller photo-z errors.

Using the mock galaxies from the HOD fitting, we compute the large-scale bias for the LRGs. The galaxy bias is defined as

$$b = \left(\xi_{\mathrm{gal}} / \xi_{\mathrm{matter}} \right)^{1/2}, \tag{3.10}$$

where ξ_{gal} and ξ_{matter} are the two-point correlation functions of galaxies and matter, respectively. The galaxy bias is a function of scale, and at large scale it asymptotes to the large-scale bias value which we compute here. Hereafter we refer to the large-scale bias simply as the galaxy bias and denote as b. We obtain the galaxy bias by taking the mean of
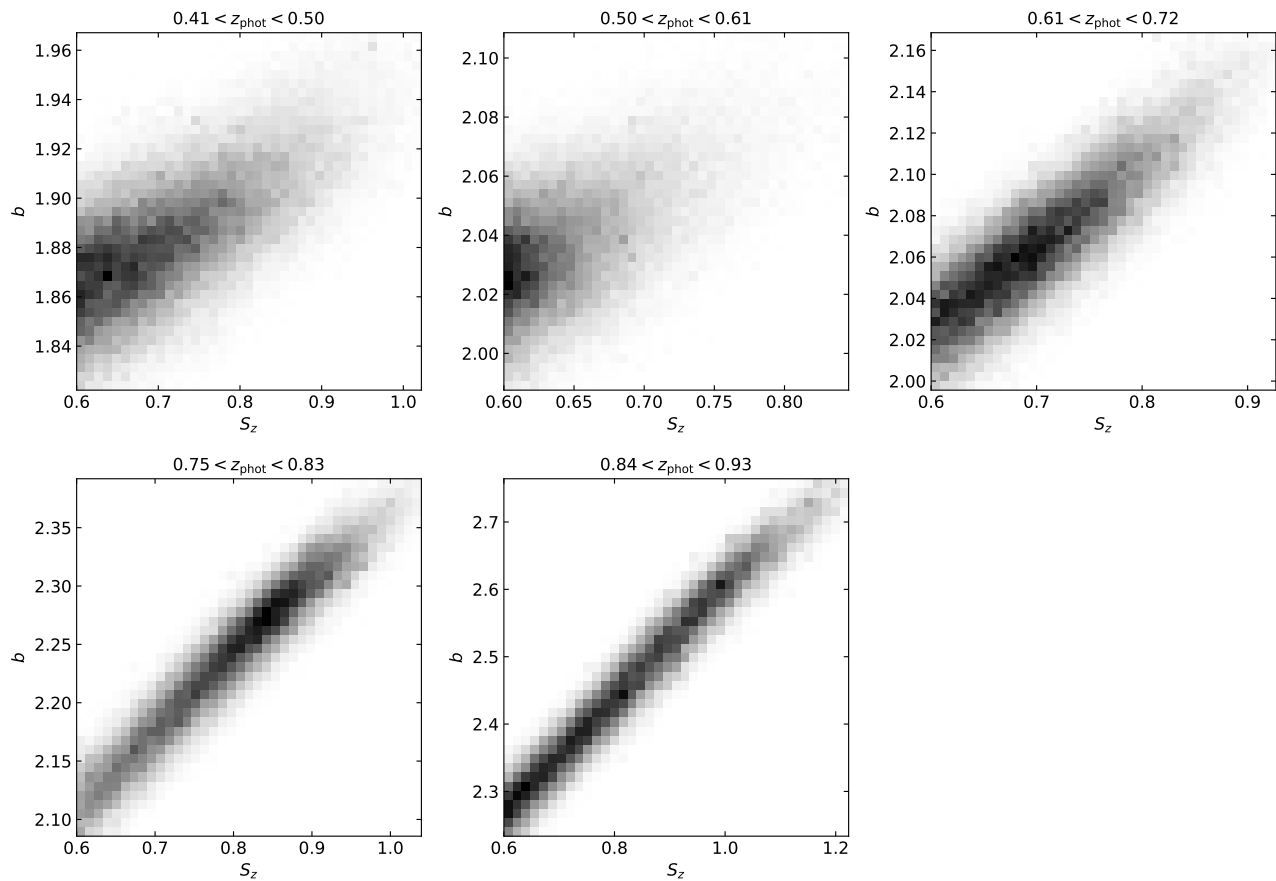
Figure 20: Two dimensional posterior distribution of galaxy bias vs. the photo-z error rescaling factor S_z at different redshifts. The correlations are much stronger at higher redshifts due to the overall larger photo-z errors that dilutes the clustering signal.

the bias of host halos weighted by the number of galaxies in each halo. To obtain the halo bias, we adopt the halo bias-halo mass relation from Tinker et al. (2010) implemented by the `Colossus` software package (Diemer, 2018). The evolution of galaxy bias with redshift, shown in Fig. 21, is consistent with the galaxy bias evolution of a sample with constant clustering amplitude, and it can be written as $b(z) = 1.5/D(z)$, where $D(z)$ is the linear growth factor. The factor 1.5 is slightly smaller than the factor 1.7 in the DESI Final Design Report (DESI Collaboration et al., 2016).

The BOSS CMASS sample (Dawson et al., 2013), which has a median redshift of $z \simeq 0.55$, was selected with similar luminosity-threshold cuts to yield roughly half the comoving number density of the our LRG sample. At $z = 0.55$, our galaxy bias estimates is consistent with $b \simeq 2.0$ from White et al. (2011) for the CMASS sample. The satellite fraction of our DESI-like LRGs is roughly 15%, compared to 10% for CMASS. The fact that there are much fewer satellite galaxies than central galaxies in LRG-like samples is a result of the selection cuts: only the most luminous galaxies are selected, and these luminous galaxies are much much more likely to be at the center of dark matter halos.

The literature on HOD analysis for comparable LRGs at higher redshifts is relatively scarce. The eBOSS survey targeted LRG in the redshift range of $0.6 < z < 0.9$ (Prakash et al., 2016), and Zhai et al. (2017) performed HOD analysis on the combined BOSS+eBOSS sample in this redshift range. However, the eBOSS LRG sample is significantly different from the our DESI-like LRGs in certain aspects: 1) the comoving number density of the DESI-like LRGs is more than 5 times that of the eBOSS LRGs, and 2) the eBOSS LRG selection does not contain luminosity-threshold cuts, resulting in a wider range of luminosity. Therefore one should not expect the two samples to have the same HOD or derived parameters. The galaxy bias of DESI-like LRGs at ∼ 0.7 (median redshift of eBOSS) is ∼ 2.15, compared to 2.3 for eBOSS LRGs. The DESI-like LRGs have a satellite fraction similar to the 13% for eBOSS LRGs.

The α parameter shows little variation with redshift and is slightly larger than unity, and this value is roughly consistent with SDSS (Zehavi et al., 2011; Zentner et al., 2019) and BOSS (White et al., 2011) results. It is significantly larger than Zhai et al. (2017) which estimates $\alpha \sim 0.4$, although this difference could be attributed to the aforementioned

differences in the sample selection. The DESI-like LRGs have much smaller scatter in the halo mass threshold (quantified by the $\sigma_{\log M}$ parameter) compared to eBOSS (which has $\sigma_{\log M} = 0.82$), which might be explained by the luminosity-threshold cut in our DESI-like LRG selection, although the strong correlation between $\sigma_{\log M}$ and the photo-z error rescaling factor suggests the possibility of biased $\sigma_{\log M}$ estimates due to additional photo-z systematics that is not account for by the rescaling factor.

Since the HOD model is probabilistic, even if the HOD parameters are fixed, each HOD realization yields a different set of mock galaxies and thus slightly different clustering statistics. This effectively adds a noise to the likelihood function in the MCMC. So long as this noise has mean of zero, it can be shown that as the number of steps becomes large the distribution of points in the chain should still converge to the correct posterior. However, this "realization noise" does cause the likelihoods associated with each step of the MCMC chain to have values which are biased high (or, equivalently, χ^2 to be biased low), since each "walker" is less likely to move away from a point whose likelihood was evaluated to be higher than average, and more likely to move away from one which fluctuated low. We show this bias in Appendix E. When the realization noise is significant (as here), one cannot directly use the likelihood values from the chain to find the best-fit point or to assess its χ^2; instead, it is necessary to average over repeated realizations of the same model parameters. This could be done at every step of the chain to reduce realization noise, but that is computationally expensive; instead, we adopt an alternative approach.

Specifically, we can exploit the fact that even though the likelihood value associated with each point in the chain is noisy and biased, the set of positions in parameter space that make up the chain do converge to the posterior distribution. As a result, the density of points in the chain is highest where the posterior probability is greatest, even when the likelihood values assigned to those points may be inaccurate. We therefore select a small set of steps from the chains which lie in the highest density region of the parameter space; this set is highly likely to contain the points in the chain closest to the best-fit parameters. We then compute the likelihood / χ^2 values for each of these sets of parameters, averaging over a large number of realizations; from this we can find the point in the chains which truly has the highest likelihood. We describe this procedure in more detail in Appendix E.
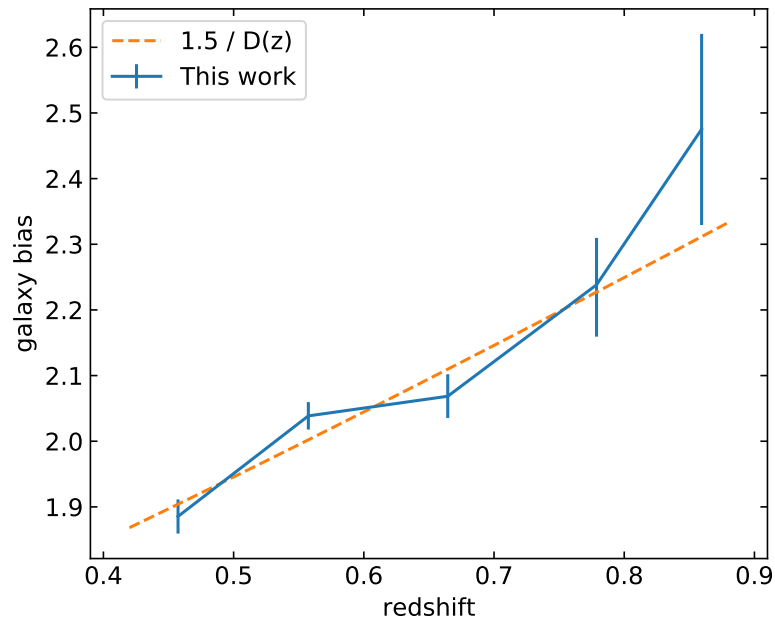
Figure 21: The evolution of galaxy bias. The error bars show the 16% and 84% percentiles. The trend is consistent with the bias evolution if assuming constant clustering amplitude, as shown in the dashed line.

Table 10: Results from the HOD fitting with MCMC for the five redshift bins. For each redshift bin, the first row lists the mean values and the 16th and 84th percentiles; the second row (in italics font) lists the median values; the third row (in bold font) lists the best-fit values in the six-dimensional HOD parameter space (these need not match the peak of each marginalized posterior distribution). The parameters $\log(M_{\mathrm{min}})$, $\sigma_{\log M}$, α, $\log(M_0)$ and $\log(M_1)$ are free parameters. The bias b and satellite fraction f_{sat} are derived parameters. We also list the χ^2 for the best-fit parameters and the corresponding one-sided p-value.

Redshift	$\log(M_{\mathrm{min}})$	$\sigma_{\log M}$	α	$\log(M_0)$	$\log(M_1)$	b	f_{sat}	χ^2 (p-value)
	$12.90^{+0.05}_{-0.05}$	$0.17^{+0.13}_{-0.13}$	$1.28^{+0.09}_{-0.10}$	$12.13^{+0.64}_{-0.71}$	$13.99^{+0.05}_{-0.05}$	$1.89^{+0.03}_{-0.03}$	$0.15^{+0.02}_{-0.02}$	
$0.41 < z_{\mathrm{phot}} < 0.50$	*12.89*	*0.16*	*1.31*	*12.19*	*14.00*	*1.88*	*0.15*	
	12.85	**0.03**	**1.29**	**12.41**	**13.97**	**1.89**	**0.15**	**4.57 (0.71)**
	$12.92^{+0.03}_{-0.04}$	$0.12^{+0.09}_{-0.09}$	$1.11^{+0.22}_{-0.21}$	$12.73^{+0.40}_{-0.46}$	$13.98^{+0.07}_{-0.07}$	$2.04^{+0.02}_{-0.02}$	$0.13^{+0.01}_{-0.01}$	
$0.50 < z_{\mathrm{phot}} < 0.61$	*12.92*	*0.11*	*1.14*	*12.88*	*13.98*	*2.04*	*0.13*	
	12.89	**0.00**	**1.10**	**12.92**	**13.95**	**2.04**	**0.13**	**9.87 (0.20)**
	$12.86^{+0.05}_{-0.05}$	$0.20^{+0.13}_{-0.13}$	$1.31^{+0.06}_{-0.06}$	$11.94^{+0.58}_{-0.62}$	$13.92^{+0.04}_{-0.04}$	$2.07^{+0.03}_{-0.03}$	$0.16^{+0.01}_{-0.01}$	
$0.61 < z_{\mathrm{phot}} < 0.72$	*12.85*	*0.19*	*1.33*	*11.97*	*13.92*	*2.07*	*0.16*	
	12.86	**0.28**	**1.32**	**11.96**	**13.91**	**2.04**	**0.16**	**6.86 (0.44)**
	$12.97^{+0.08}_{-0.08}$	$0.29^{+0.19}_{-0.20}$	$1.28^{+0.12}_{-0.12}$	$12.05^{+0.69}_{-0.71}$	$14.00^{+0.05}_{-0.05}$	$2.24^{+0.07}_{-0.08}$	$0.14^{+0.02}_{-0.02}$	
$0.75 < z_{\mathrm{phot}} < 0.83$	*12.95*	*0.28*	*1.33*	*12.06*	*14.00*	*2.24*	*0.14*	
	12.90	**0.02**	**1.38**	**12.18**	**13.98**	**2.31**	**0.14**	**3.29 (0.86)**
	$13.26^{+0.13}_{-0.13}$	$0.45^{+0.20}_{-0.22}$	$1.20^{+0.31}_{-0.42}$	$12.33^{+0.91}_{-0.90}$	$14.31^{+0.07}_{-0.12}$	$2.48^{+0.15}_{-0.15}$	$0.10^{+0.02}_{-0.02}$	
$0.84 < z_{\mathrm{phot}} < 0.93$	*13.24*	*0.48*	*1.34*	*12.34*	*14.25*	*2.47*	*0.10*	
	13.40	**0.70**	**1.38**	**11.70**	**14.24**	**2.28**	**0.10**	**6.65 (0.47)**

Table 10 lists the best-fit parameters and the corresponding averaged χ^2 values averaged over 1000 realizations. The table also lists the one-sided p-values corresponding to each χ^2 value; i.e., the probability of observing a χ^2 larger than the observed value purely by chance (if we find $p < 0.05$, the hypothesis that the best-fit HOD model matches the data should be rejected). We compute this p-value using the number of degrees of freedom $N_{\mathrm{dof}} = N_{\mathrm{data}} - N_{\mathrm{param}} = 13 - 6 = 7$, where N_{data} is the number of r_{p} bins plus one additional constraint from the comoving number density, and N_{param} is the number of free parameters. In every case, the HOD model returns a satisfactory fit.

3.7 DISCUSSION AND CONCLUSION

We have made a number of methodological improvements for galaxy clustering analysis with the HOD model using photo-z's. We have developed a method that divides the irregular survey footprint into uniform subregions that allowed us to apply the jackknife resampling technique on this dataset. Our methods of correlation measurements using the projected correlation function and the "cross-correlation" L-S estimator recover many galaxies pairs straddling the boundaries of the redshift bins, and prevent the counting of pairs which are too far apart in photo-z to have significant clustering but are still placed in the same redshift bin. Both effects boost the S/N in clustering measurements compared to a purely angular clustering analysis. The methods also allow for straightforward and consistent modeling by assigning photo-z errors from the estimated error distribution to the mock galaxies.

With these aforementioned improvements, we have demonstrated that it is possible to obtain good constraints on HOD parameters using only photometric data. Specifically, we have measured the clustering and performed HOD analysis for DESI LRG target galaxies. We have found that the LRGs are found only in massive halos (and especially so for high-z LRGs); this is expected since we're looking at massive and red galaxies and those are found only in the densest environments. We have also found that the host halo properties are very similar for all except the highest redshift bin. The galaxy bias steadily increases with redshift, increasing from $b \simeq 1.9$ at $z \simeq 0.45$ to $b \simeq 2.3$ at $z \simeq 0.9$. This trend can be approximated by

$b = 1.5/D(z)$, implying constant clustering amplitude over time. The fits prefer a relatively small scatter in the halo mass threshold, suggesting that the LRG selection is efficient in selecting galaxies only in massive dark matter halos. At high redshift, the host halos are significantly more massive; this is due to the selection effect of the apparently magnitude limit on the galaxy sample.

The results of this paper can be used to create improved mock galaxies for DESI. The upcoming spectroscopic data from DESI will eliminate the uncertainties from photo-z's and provide tests of our results, although there is the additional systematics from fiber collisions to be dealt with. The spectroscopic redshifts will also enable the accurate measurements of the rest-frame colors and luminosity, and it would be interesting to study the color and luminosity dependence of the galaxy clustering; results from such studies can provide important insights into the formation and evolution of these massive galaxies.

The overall methodology of HOD modeling with photo-z's presented here can be easily implemented with existing analysis codes such as `halotools`, and it can be adopted for future imaging surveys such as LSST for studying galaxy-halo connection. There are several aspects where our methods can be further improved upon by adding more sophistication, and we discuss below.

First, the approximation of Gaussian photo-z errors is not always appropriate. In our case, the LRGs have prominent spectral features such as the 4000Å break and the 1.6 micron bump that results in unambiguous photo-z's. As a result, we are able to treat each PDF as a simple Gaussian distribution, assuming that the photo-z errors are dominated by photometric errors; this simplification is supported by spectroscopic validation. However, in many other cases, the Gaussian approximation is not sufficient, and one need to take the full photo-z PDFs as input in the fitting process; this can be important for galaxies that have skewed or multimodal PDFs or for datasets that have weak constraining power on redshifts.

Second, although in our case the uncertainty in the calibration of photo-z errors (quantified by S_z) is subdominant at lower redshift, at higher redshift it causes significant uncertainties in HOD parameters and galaxy bias. Therefore, in the presence of relatively large photo-z errors, better priors on the calibration of photo-z uncertainties would significantly reduce the uncertainties in the model parameters. This can be achieve using a small

spectroscopic subsample that is representative of full photometric sample.

Third, in this work we have assumed that the our galaxy sample have the same intrinsic photo-z error properties, and the distribution of actual photo-z errors are solely due to the variation in the S/N of the photometry; therefore we can randomly draw from the estimated photo-z errors and assign it to each mock galaxy. This assumption might not hold for a sample of galaxies that are more diverse than the LRGs; for example, in a pure luminosity threshold sample, the blue and red galaxies will have very different intrinsic photo-z errors/PDFs. Nevertheless, the method can account for such differences by treating differently halos with different properties when assigning photo-z errors to the corresponding galaxies.

Finally, since the correlation function is measured with relative distances, it is insensitive to an overall offsets in photo-z's so long as the offset is the same for all galaxies in the sample. Our model does not account for higher order offsets, and light-cone mocks would be required to simulate such effects.

With these improved methods and enlarged samples from future surveys, fully photometric HOD modeling will be a powerful tool for studying the galaxy-halo connection with future imaging surveys such as LSST.

4 CONCLUSION

In the first part of this thesis we described a new spectroscopic dataset that can be used as a photo-z testbed for LSST. The dataset provides realistic galaxy colors, which simulated galaxy catalogs cannot provide, that enable reliable tests of LSST photo-z algorithms. Perhaps the biggest limitation of this sample is that it is complete only to $R_{AB} < 24$ (although it does include redshifts for many fainter objects, allowing limited tests in other domains), roughly 3 magnitudes shallower than the final LSST depth. This is due to the general lack of spectroscopic redshifts for faint galaxies. To train and validate photo-z's down to LSST depth would require substantial efforts to obtain spectroscopic data in the near future. Another limitation of this dataset is that the DEEP2 sample with secure redshifts is significantly incomplete at $z > \sim 1.4$ ($z > \sim 1.6$ for DEEP3) due to the [O_{II}] $\lambda 3727$ doublet transitioning out of the wavelength coverage of DEEP2.

In the second part of this thesis we described the clustering analysis of DESI-like LRGs with improved methods that among other things make optimal use of photometric redshifts. We find that the LRGs only reside in massive dark matter halos, and they have near-constant intrinsic clustering amplitudes over the full redshift range (except at the highest redshifts where selection effects cause even stronger clustering). This confirms the presumption that the DESI LRG sample consists of highly biased tracers of matter, and the modeling results can be used to guide DESI analyses (e.g., high redshift LRGs should be treated separately) and for creating initial DESI mock catalogs. The results will soon be validated when spectroscopic data becomes available from DESI, and some of the improved methods can be easily adopted for the clustering analysis of this spectroscopic dataset. The results of the clustering analysis will also provide valuable information for the design of the LRG target selection. Beyond DESI, the methods that we have developed can be adopted for studying

the galaxy-halo connection in future imaging surveys such as LSST.

Besides maximizing BAO S/N, another important consideration for DESI is the potential systematic errors (from both astrophysical and instrumental sources) and how to design a target selection algorithm that minimizes them. This can be a limiting factor for certain sensitive measurements such as the measurement of primordial non-Gaussianity. Our efforts (within and beyond the LRG clustering analysis) to study and eliminate systematics (such as the development of improved bright star masks) has resulted in improvements in the DESI imaging pipelines and improved LRG target selections that are less sensitive to systematics.

Although we have learned a great deal about the DESI LRG sample, there are still many observational and astrophysical uncertainties for DESI, such as the efficiency of successfully measuring redshifts for these targets and the exact redshift distributions of the spectroscopic targets. The Survey Validation phase of the DESI survey will settle these uncertainties, and we will use the results to further improve target selection algorithms.

The next decade will see the start of many large cosmological surveys. It is hard to imagine what will be revealed by these surveys and the numerous other experiments in observational cosmology; it is truly an exciting time.

APPENDIX A

Y-BAND SEXTRACTOR PARAMETERS

Source catalogs in the *Y*-band were obtained by running SExtractor on the *Y*-band images. The SExtractor parameters used for the deep pointing are listed in section A.1. For the shallow pointing, only a few parameters were altered; these are listed at the end of the table. The "PHOT_APERTURES" parameters specify the aperture diameters of the MAG_APER photometry, which we use to compute the MAG_APERCOR photometry. Note that SExtractor (version 2.19.5) cannot produce more than 30 aperture magnitudes, so we had to separate the apertures into two parameter files (but with the same maximum aperture size to ensure the same set of detections) and run them separately.

A.1 SEXTRACTOR PARAMETERS

```
SExtractor parameters for the deep pointing

#----------------------------- Extraction --------------------------------

DETECT_TYPE     CCD              # CCD (linear) or PHOTO (with gamma correction)
DETECT_MINAREA  3                # min. # of pixels above threshold
DETECT_MAXAREA  6400

DETECT_THRESH   2.0              # <sigmas> or <threshold>,<ZP> in mag.arcsec-2
ANALYSIS_THRESH 2.0              # <sigmas> or <threshold>,<ZP> in mag.arcsec-2
THRESH_TYPE     RELATIVE

FILTER          Y                # apply filter for detection (Y or N)?
FILTER_NAME     gauss_2.5_5x5.conv   # name of the file containing the filter

DEBLEND_NTHRESH 64               # Number of deblending sub-thresholds
DEBLEND_MINCONT 0.001            # Minimum contrast parameter for deblending
```

```
CLEAN            Y                # Clean spurious detections? (Y or N)?
CLEAN_PARAM      1.0              # Cleaning efficiency


#----------------------------- WEIGHTing ----------------------------------

WEIGHT_GAIN      N                # If true, weight maps are considered as gain maps.
WEIGHT_TYPE      MAP_RMS          # type of WEIGHTing: NONE, BACKGROUND,
                                  # MAP_RMS, MAP_VAR or MAP_WEIGHT
WEIGHT_IMAGE     weight_maps/BACKGROUND_RMS_SIZE_16.FITS    # weight-map filename


#----------------------------- FLAGging -----------------------------------

FLAG_IMAGE       edge_flag.fits # filename for an input FLAG-image
FLAG_TYPE        MOST             # flag pixel combination: OR, AND, MIN, MAX
                                  # or MOST


#----------------------------- Photometry ---------------------------------

PHOT_APERTURES   9, 10, 11, 12, 13, 14, 15, 16, 17, 18, 19, 20, 21, 22, 23, 24,
25, 26, 27, 28, 29, 30, 31, 32, 33, 34, 35, 36, 37, 38, 39, 40, 41, 42, 43, 44,
45, 46, 47, 48, 49, 50, 51, 52, 53, 54, 55, 56
                                  # MAG_APER aperture diameter(s) in pixels
PHOT_AUTOPARAMS  2.5, 3.5         # MAG_AUTO parameters: <Kron_fact>,<min_radius>
PHOT_PETROPARAMS 2.0, 3.5         # MAG_PETRO parameters: <Petrosian_fact>,
                                  # <min_radius>
PHOT_AUTOAPERS   20.0,20.0        # <estimation>,<measurement> minimum apertures
                                  # for MAG_AUTO and MAG_PETRO
PHOT_FLUXFRAC    0.2, 0.5, 0.8 #Fraction of FLUX AUTO defining each element of
the FLUX RADIUS vector.

SATUR_LEVEL      36000.0          # level (in ADUs) at which arises saturation
SATUR_KEY        SATURATE         # keyword for saturation level (in ADUs)

MAG_ZEROPOINT    31.2             # magnitude zero-point
MAG_GAMMA        4.0              # gamma of emulsion (for photographic scans)
GAIN             1                # detector gain in e-/ADU
GAIN_KEY         GAIN             # keyword for detector gain in e-/ADU
PIXEL_SCALE      0                # size of pixel in arcsec (0=use FITS WCS info)

#----------------------- Star/Galaxy Separation ---------------------------

SEEING_FWHM      0.648            # stellar FWHM in arcsec
STARNNW_NAME     default.nnw      # Neural-Network_Weight table filename

#----------------------------- Background ---------------------------------

BACK_TYPE        AUTO             # AUTO or MANUAL
BACK_VALUE       0.0              # Default background value in MANUAL mode
BACK_SIZE        128              # Background mesh: <size> or <width>,<height>
BACK_FILTERSIZE  5                # Background filter: <size> or <width>,<height>
BACKPHOTO_TYPE   LOCAL
BACKPHOTO_THICK  24

#-------------------- Memory (change with caution!) -----------------------

MEMORY_OBJSTACK  3000             # number of objects in stack
MEMORY_PIXSTACK  9000000          # number of pixels in stack
MEMORY_BUFSIZE   1024             # number of lines in buffer


     The following parameters are for the shallow pointing:
DETECT_MINAREA   5
SATUR_LEVEL      280000.0
SEEING_FWHM      0.625
```

APPENDIX B

APERTURE CORRECTION PROCEDURES

Two assumptions are made in determining our aperture corrections. The first is that all objects have a circular symmetry and their light profiles can be described by a Moffat profile (described in more detail below). The second assumption is that in each band in each pointing, the parameters describing the Moffat profile only depend on the half-light radius and that they are smooth functions of this quantity. Under these assumptions, we can measure the flux in a small aperture and use the Moffat profile appropriate for a given object's half-light radius to extrapolate the total flux. We perform aperture corrections separately for each band in each pointing so that we can account for differences between seeing in each image.

The Moffat light profile is described by the equation

$$I(r; \alpha, \beta) = \frac{\beta - 1}{\pi \alpha^2} \left[1 + \left(\frac{r}{\alpha} \right)^2 \right]^{-\beta},$$ (B.1)

where I denotes the flux density and r is the angular distance from the center of the source. There are two free parameters: α determines the width of the profile and β determines its shape. If β is small, the light profile includes more flux at larger radii (larger "wings"), while $\beta \to \infty$ corresponds to a Gaussian profile. In this formula, the light profile is normalized so that the total flux is 1. The fraction of flux inside radius r is then

$$\text{frac}(r) = \int_0^r 2\pi x I(x) dx = 1 - \alpha^{2(\beta-1)} \left(\alpha^2 + x^2 \right)^{1-\beta}.$$ (B.2)

A measurement of the half-light radius from SExtractor is provided by CFHTLS. In

principle, we can determine α by solving equation B.2 for the case $I(R_{1/2}; \alpha, \beta) = 1/2$, where $R_{1/2}$ is the half-light radius, leaving only one free parameter, β. However, we found that the "half-light" radius measured by SExtractor does not capture exactly half of the total flux, so we treat α as a free parameter as well. In the rest of this section we use $R_{1/2}$ and the word radius to refer to the SExtractor-measured half-light radius rather than the value derived from the Moffat fit.

One set of α and β is enough to characterize the light profiles of stars since they have essentially the same light profile (i.e., the PSF). Galaxies have different light profiles, so we divide galaxies into radius bins and find the optimal α and β for each bin. The bin sizes are $0.0558''$ for u and z bands, $0.0372''$ for g, r, i bands and $0.03''$ for Y-band. The smallest bin is set by the PSF (stars) and the largest bin has a radius of $1.1''$–$1.2''$. We use the CFHTLS "flag" column for star-galaxy separation.

To avoid large radius errors in bands with low S/N, and also to reduce errors in colors (e.g., $u - g$) by ensuring consistent treatment of radii, we binned objects according to their r-band radii when determining the aperture correction for each CFHTLS passband. For the Y-band aperture correction the Y-band radius was used for binning as many objects are not detected in r. For each radius bin, we compute the average curve of growth of flux as a function of radius by simply averaging the curve of growth of the individual objects within that bin.

CFHTLS provides SExtractor aperture magnitudes (MAG_APER) for aperture radii ranging from 5 pixels to 30 pixels in 1 pixel spacing; we use these magnitudes for the curve of growth calculations. For the Y-band we also produced similar SExtractor aperture magnitudes; see Appendix A for details of the Y-band aperture magnitudes.

Only objects with relatively high S/N must be used for calculating the curve of growth to avoid background contamination, so we require the MAG_AUTO error be smaller than these limits: $[0.02, 0.01, 0.01, 0.01, 0.01, 0.01]$ for $u, g, r, i, i2, z$ in the CFHTLS Deep field, $[0.05, 0.05, 0.05, 0.04, 0.05]$ for u, g, r, i, z in CFHTLS Wide fields, 0.02 for the Y-band deep pointing and 0.05 for Y-band shallow pointing. We also exclude saturated, masked or blended objects by requiring the CFHTLS "flag" value to be ≤ 1 and the SExtractor flag (in r-band or Y-band) to be 0. Fig. 22 shows examples of the curve of growth fits.

We then obtain α and β by fitting equation B.2 to the measured curve of growth for a given radius bin by least squares. Once we know α and β, we can measure the flux of each object in a small aperture r_0, and extrapolate to infinity to obtain the total flux. Essentially, we have then determined the aperture correction factor for a given radius bin:

$$\text{ApCorr} = \text{frac}(\infty)/\text{frac}(r_0) = \left\{ \frac{\beta - 1}{\pi \alpha^2} \left[1 + \left(\frac{r_0}{\alpha} \right)^2 \right]^{-\beta} \right\}^{-1}, \tag{B.3}$$

where α and β are fit separately for each bin.

For the $ugriz$ bands, we choose the aperture radius $r_0 = 5$ pixels ($0.93''$), because among available apertures this choice yielded the highest S/N photometry for all but the brightest objects. For Y-band we choose a similar aperture radius of $r_0 = 4.5$ pixels ($0.9''$).

After obtaining ApCorr for each radius bin, we calculate ApCorr as a function of radius by linear interpolation to determine the correction for each individual object. To obtain the correction factor for objects larger than the largest radius bins, we must extrapolate $\text{ApCorr}(R_{1/2})$ to larger radii. To do this, we use the α and β from the largest radius bin to calculate the actual fraction of light within the SExtractor "half-light" radius, and assume that this fraction is the same for all objects of larger radii; we then keep β fixed and use the SExtractor "half-light" radius to estimate α and obtain ApCorr. Fig. 23 shows the correction factor ApCorr as a function of radius.

Finally, we use the function $\text{ApCorr}(R_{1/2})$ to obtain the total flux from the aperture flux within aperture radius r_0 for every object in the catalog.
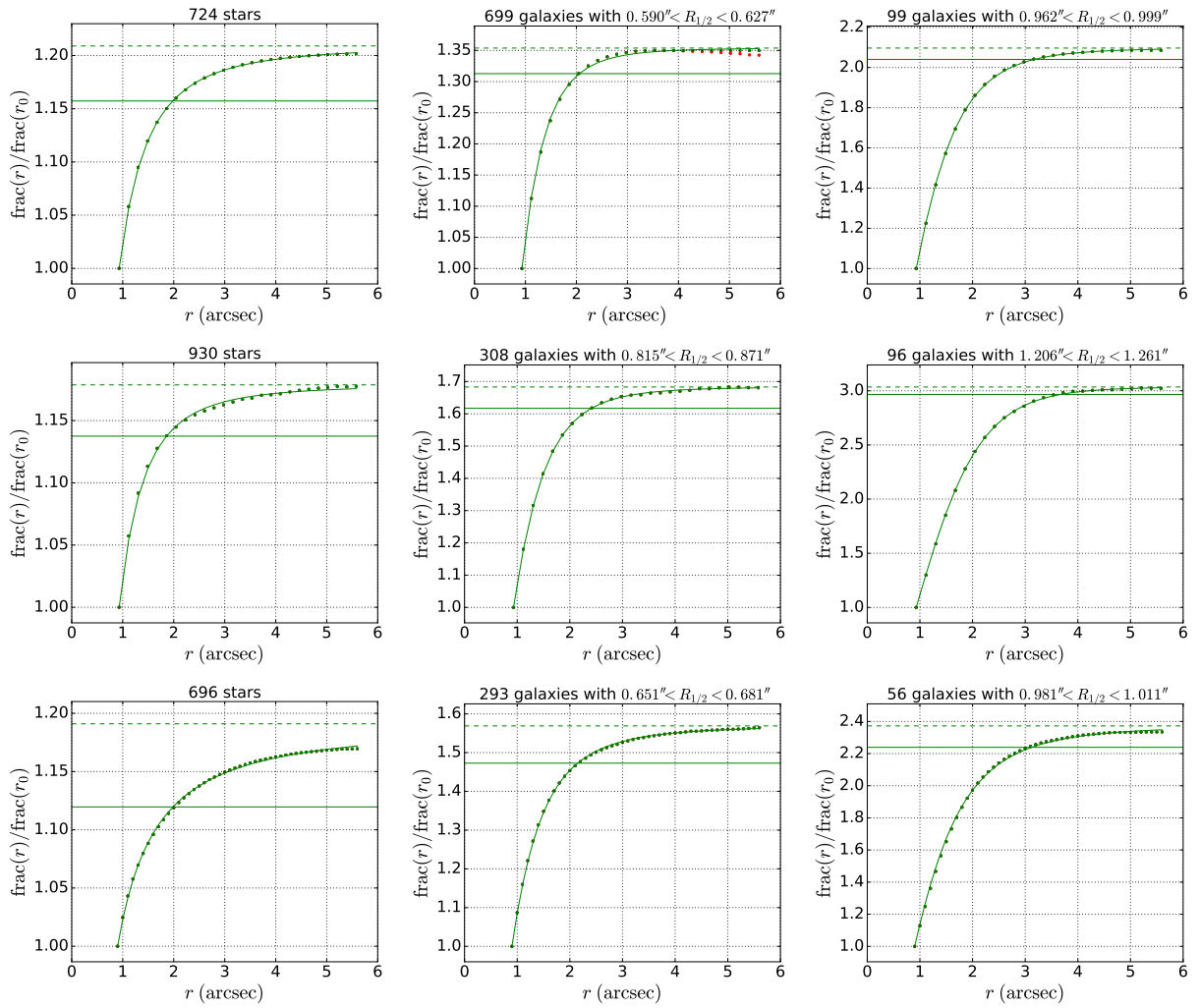
Figure 22: (Caption next page.)

Figure 22: (Previous page.) Examples of curve of growth and its Moffat fit. The Y-axis is the ratio of the flux in aperture radius r to the flux in the fixed aperture radius r_0. Points are the observed flux ratio for each radius bin. The solid curve is the Moffat fit. The solid horizontal line is the ratio of the flux in MAG_AUTO to the flux in the fixed aperture radius r_0, and the dashed horizontal line is the predicted flux ratio for an infinitely large aperture. (a), (b) and (c) show CFHTLS D3 i-band. (d), (e) and (f) show CFHTLS W3-0-2 u-band. (g), (h) and (i) show the Subaru Y-band deep pointing. In (b), the flux ratio decreases at large apertures (red points) due to non-zero background, and it is corrected by extrapolating using the maximum flux ratio (green points). Such non-zero background might carry a different sign, showing as large increase of flux ratio at large apertures, although in this case it is hard to distinguish between flux from the source and the flux from the background, and no correction is applied. We tried to minimize the effects of imperfect background subtraction by selecting bright objects (with smaller photometric error) for the fit.

B.1 ERROR ESTIMATION

Assuming that our model of the star and galaxy light profiles is correct, the corrected aperture magnitude MAG_APERCOR should have two sources of error: photometric errors in the aperture magnitude which were measured by SExtractor, and the error in the correction factor ApCorr which we multiplied by. In the catalog and in this paper, we label MAGERR_APER (uerr_aper, gerr_aper, etc.) as the photometric error from SExtractor, and MAGERR_APERCOR (uerr_apercor, gerr_apercor, etc.) as the statistical uncertainty in the correction factor.

Here we assume that the error in $\mathbf{ApCorr}(R_{1/2})$ is only due to the error in the radius $R_{1/2}$, and the correction factor itself has negligible error if the radius is accurate. SExtractor does not provide the error in the radius, so we can only estimate this quantity indirectly. For $ugriz$ bands where the r-band radius is used, we assume that the i-band radius error σ_{R_i} is the same as the r-band radius error σ_{R_r}, and since they are independent measurements, we
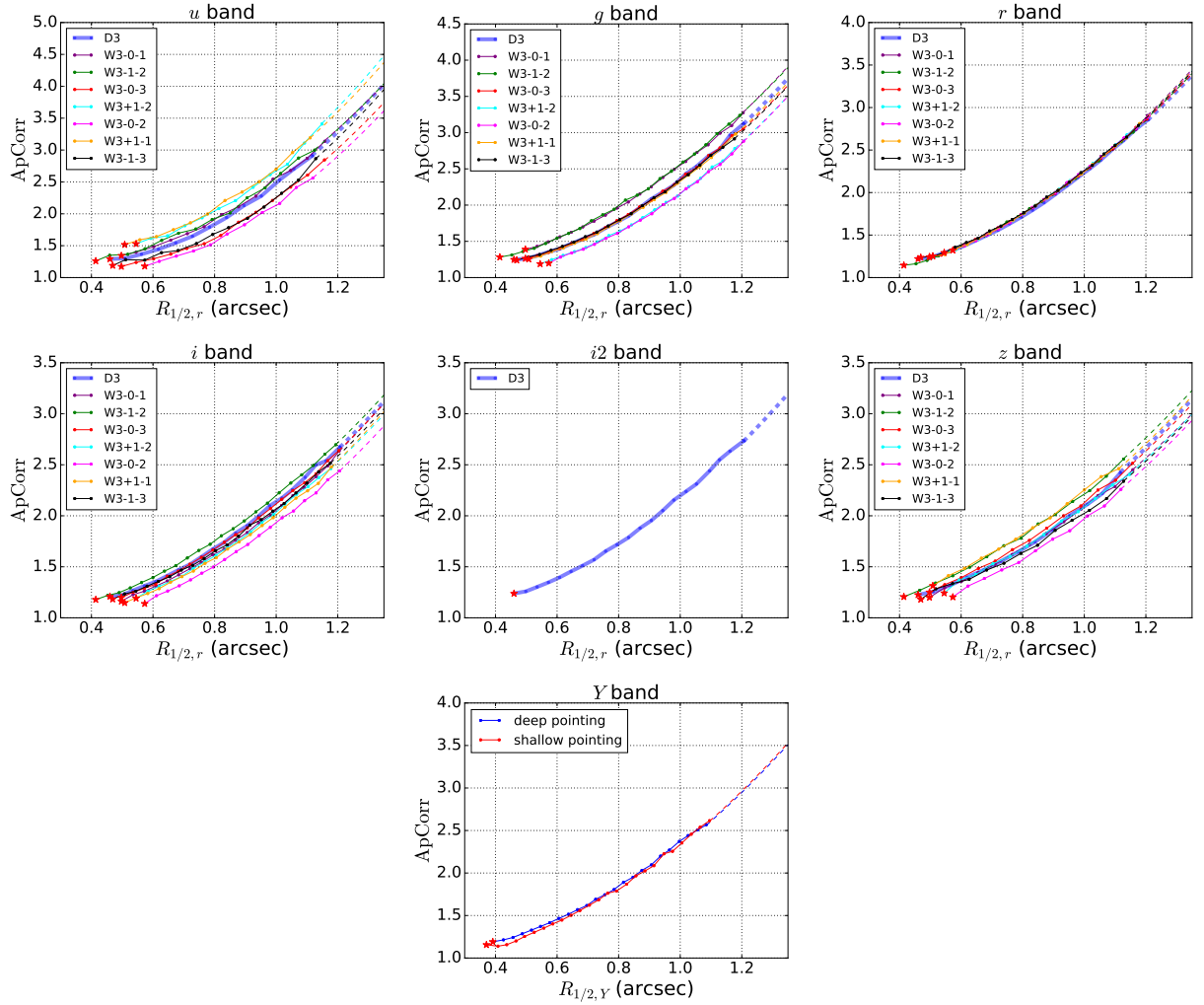
Figure 23: Each plot shows the correction factor ApCorr in one band as a function of half-light radius, over-plotting all pointings. In (a-f) the thick line is the Deep field D3 and the thin lines are the Wide field W3 pointings. (g) shows the *Y*-band. The correction factor and radius of stars are plotted as the star marker. The dashed line is the extrapolation for objects larger than the radius bins.

can estimate σ_{R_r} from the scatter of $f_{i,r} = R_i/R_r$ about its mean value, so that

$$\frac{\sigma_{R_r}}{R_r} = \frac{\sigma_{f_{i,r}}}{\sqrt{2}\bar{f}_{i,r}}. \tag{B.4}$$

Here $\bar{f}_{i,r}$ in the denominator is the average value of $f_{i,r}$. The radius error increases with decreasing S/N, so we calculate $\sigma_{f_{i,r}}$ for objects in r-band magnitude bins, and we obtained the fractional radius error σ_{R_r}/R_r as a function of magnitude. Similarly, we can assume that $\sigma_{R_g} = \sigma_{R_r}$, and calculate σ_{R_r}/R_r using $f_{g,r} = R_g/R_r$. We find that the fractional radius errors from g-band and i-band are consistent, and therefore we simply use the average of the two results as the final fractional radius error. Given the resulting estimate of the fractional radius error, we calculate MAGERR_APERCOR for each object via propagation of errors:

$$\text{MAGERR\_APERCOR} = \frac{\sigma_A}{A} = \frac{1}{A}\frac{dA}{dR_r}R_r\frac{\sigma_{R_r}}{R_r}, \tag{B.5}$$

where A is short for ApCorr. Similarly, in the Y-band, we match the objects to CFHTLS, and estimate σ_{R_Y} and MAGERR_APERCOR from the scatter of $f_{z,Y} = R_z/R_Y$.

In cases where one wishes to estimate the uncertainty in the total magnitude of an objects, the net error in MAG_APERCOR is

$$\sigma_{\text{MAG\_APERCOR}} = \sqrt{(\text{MAGERR\_APER})^2 + (\text{MAGERR\_APERCOR})^2}. \tag{B.6}$$

Since the r-band radius is used for aperture correction for all of $ugriz$, the correction error MAGERR_APERCOR is correlated and mostly cancels out when we calculate colors involving the $ugriz$ bands. For example, the error in $u - g$ color is

$$\sigma_{u-g} = \sqrt{\text{UERR\_APER}^2 + \text{GERR\_APER}^2 + (\text{UERR\_APERCOR} - \text{GERR\_APERCOR})^2}. \tag{B.7}$$

The Y-band aperture correction did not use r-band radius, and the error in $z - Y$ is

$$\sigma_{z-y} = \sqrt{\text{ZERR\_APER}^2 + \text{YERR\_APER}^2 + \text{ZERR\_APERCOR}^2 + \text{YERR\_APERCOR}^2}. \tag{B.8}$$

Similar formulae may be used to determine the net uncertainty in any color derived from these passbands.

APPENDIX C

WISE BRIGHT STAR MASKS

This appendix provides some technical details of the WISE bright star masks that we described in section 3.2.2. The WISE bright star masks are geometric masks around stars in the AllWISE catalog with $W1_{AB} < 16.0$. The masks consist of two components: circular masks for the "core" of a bright star, and rectangular masks for the diffraction spikes. The size of the masks vary with the $W1$ magnitude of the bright star, and the size-magnitude relation is shown in Fig. 24. To obtain the size-magnitude relation, we cross-correlate the positions on the sky between LRGs and bright stars in magnitude bins of $\Delta W1_{AB} = 0.5$, and locate (by hand) the distance where the LRG density starts to noticeably deviate from the densities further away from the stars. This way the majority of the contaminated objects in the LRG sample are masked. Fig. 25 shows the cross-correlation between the LRG sample and AllWISE stars with $6 < W1_{\mathrm{AB}} < 8$ with the masks overlaid.
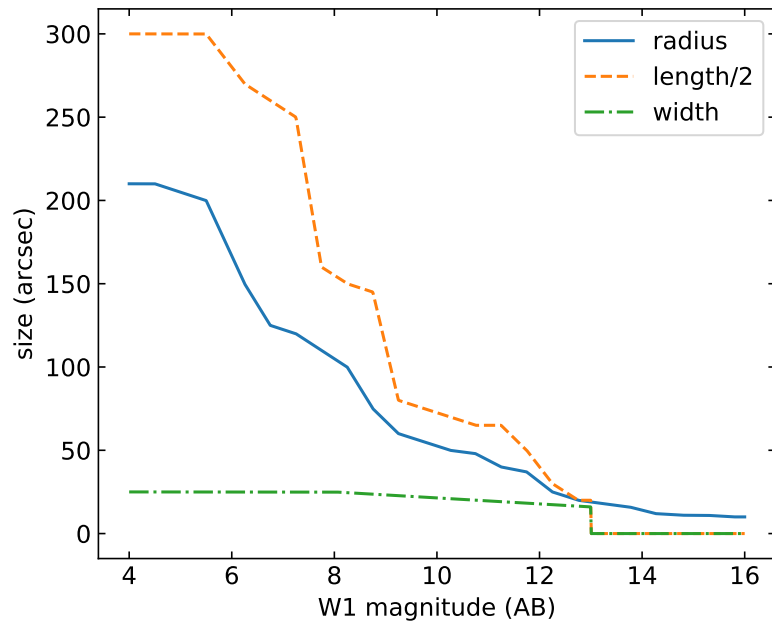
Figure 24: The circular mask radius and the length and width of the rectangular mask as a function of W1 magnitude of the bright star. No masking of diffraction spikes is performed for stars fainter than $W1_{\mathrm{AB}} = 13.0$.
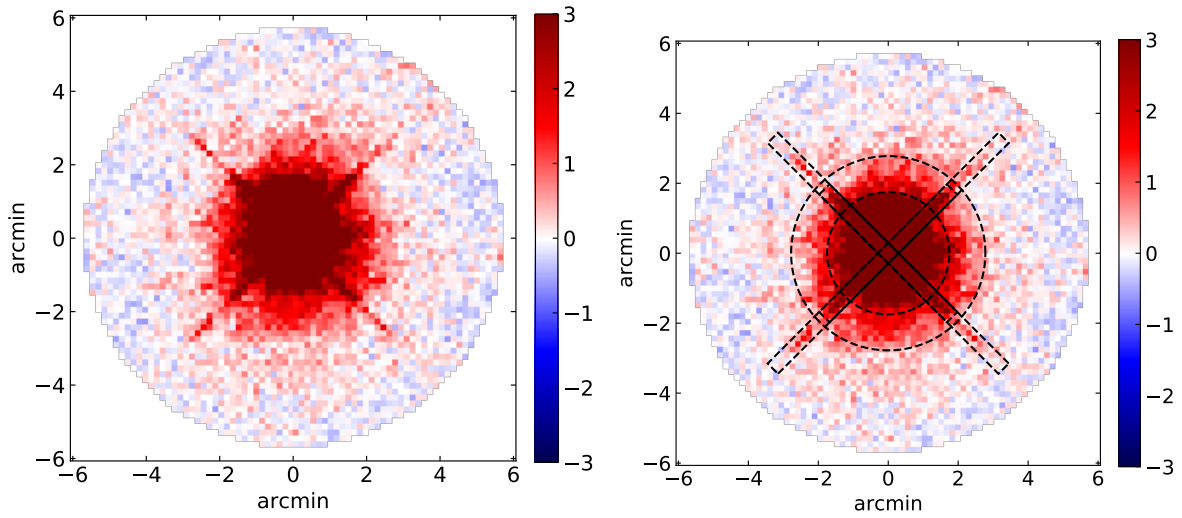
Figure 25: Left panel: Cross-correlation between LRGs and AllWISE bright stars with $6 < W1_{\mathrm{AB}} < 8$ in ecliptic coordinates. The colors represent the fractional over/under-density of LRGs compared to the overall average density (as a result the values cannot drop below -1). Right panel: the boundaries of the WISE masks at $W1_{\mathrm{AB}} = 6$ and $W1_{\mathrm{AB}} = 8$ are overplotted.

APPENDIX D

DECALS PHOTOMETRIC REDSHIFT PERFORMANCE FOR GENERAL SAMPLES

In this appendix, we assess the photo-z performance for the general galaxy samples that are not restricted to the LRGs.

The photo-z performance of the LRGs is discussed in section 3.3.5. To assess the photo-z accuracy for the spectroscopic training sample, we perform separate tests where we apply the K-fold cross-validation method: we randomly divide the dataset into 5 equal chunks, and each time we combine 4 chunks for training and evaluate the performance with the remaining chunk, and we repeat this until all 5 chunks have been used for testing. This way the entire truth dataset is utilized for testing without compromising the assessment of performance.

Fig. 26 shows the comparison between photo-z's and spec-z's for $z_{\mathrm{mag}} < 21.0$ objects in the truth catalog. For the (unweighted) objects in Fig. 26, the photo-z scatter is ~ 0.015 and outlier rate is 2%, although it is worth noting that this sample is dominated by bright galaxies from surveys like SDSS and BOSS and therefore the numbers do not represent the photo-z accuracy of the LRG sample.

Fig. 27 is the same plot but for $z_{\mathrm{mag}} > 21.0$ objects. Clearly the photo-z's start to systematically break down beyond $z_{\mathrm{mag}} \simeq 21$, and this is due to the limitations in our imaging data: $W1$ and $W2$ are too shallow to be useful for the fainter galaxies, so for these galaxies we are effectively limited to only three optical bands in grz which are not sufficient to constrain the photo-z's. The shallow $W1/W2$ imaging is particular problematic for galaxies with $z < \sim 0.5$, whose 1.6 micron bump is still far from the $W1$ band, causing their photo-z's

to fail catastrophically. Our LRG sample is brighter than $z = 20.41$, so we are not affected by this limitation.
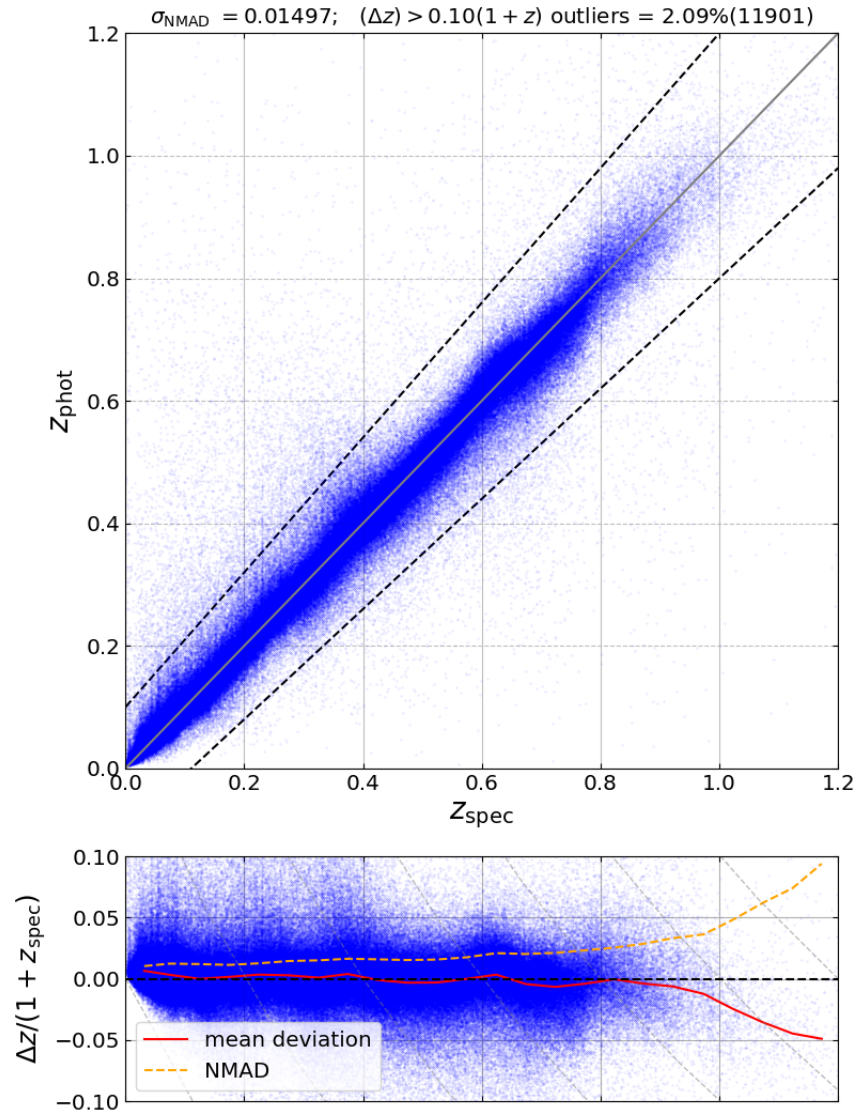
Figure 26: Photo-z vs. spec-z plot similar to 10, but for $z_{\text{mag}} < 21.0$ objects in the truth catalog and without any weighting. The photo-z's are mostly well-behaved in this regime with.
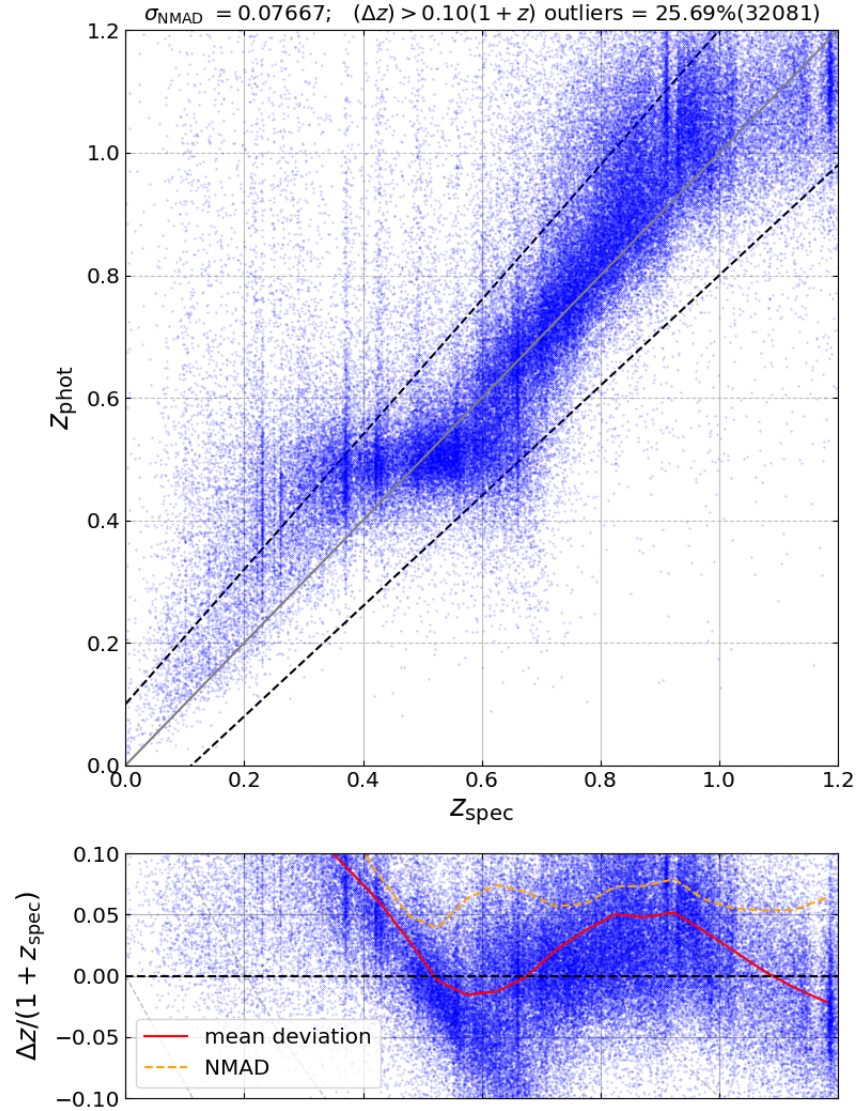
Figure 27: Same as 26 but for $z_{\mathrm{mag}} > 21.0$ objects in the truth catalog. In this regime the photo-z's are poorly constrained, especially for objects with $z < \sim 0.5$.

APPENDIX E

IDENTIFYING MAXIMUM-LIKELIHOOD VALUES IN NOISY MCMC

In this appendix we provide more details on the treatment of noisy MCMC that we discussed in the last part of section 3.6.

To demonstrate that the likelihoods (or, equivalently χ^2 since we use flat priors) at each step from the MCMC chain are biased, we randomly select 100 points from the chain, and for each point we obtain the average χ^2 value over 100 HOD realizations. Figure 28 shows the difference between χ^2 values from the MCMC chain (with no averaging) and the averaged χ^2 value for the 100 points; the same redshift bin is used for all other figures in this section. Clearly the χ^2 values are biased low compared to the averaged values. This bias is cased by noise in the MCMC likelihood function, and we discussed it in section 3.6.

To demonstrate the difficulty of using the likelihood from the MCMC chain for finding the best-fit parameters in the presence of realization noise, here we show that the points selected to have the highest likelihood values have a very wide distribution in the parameter space. In MCMC the chain positions are correlated, and sometimes a walker can get "stuck" at the same position for many steps; to reduce such effects, we divide the chain into 500 segments, and select the highest likelihood point in each segment, and plot their positions in parameter space in Figure 29. Even those these points have higher likelihoods in the chain than 99.95% of the sample, they span a large range in parameter space.

As selecting the best-fit parameters using the chain likelihoods does not yield good results, we adopt an alternative approach. The distribution of points in the chain should converge to follow the posterior. As a result, the density should be greatest where the posterior is
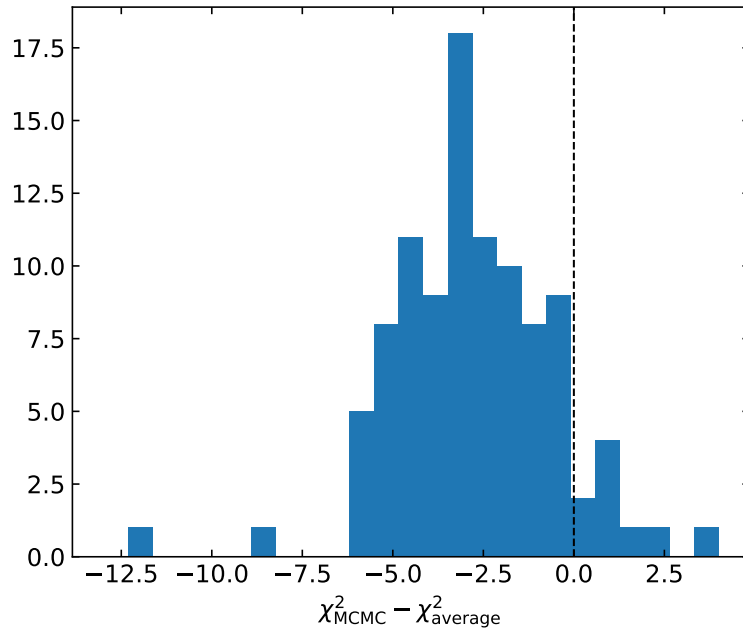
Figure 28: The histogram of the χ^2 difference between values in the MCMC chain and the average of 100 separate realizations at the same point in parameter space, for the redshift bin of $0.61 < z < 0.72$. The vertical line highlights the location of zero difference. The χ^2 difference is clearly non-zero on average, indicating that the χ^2 values from the MCMC chain are biased.
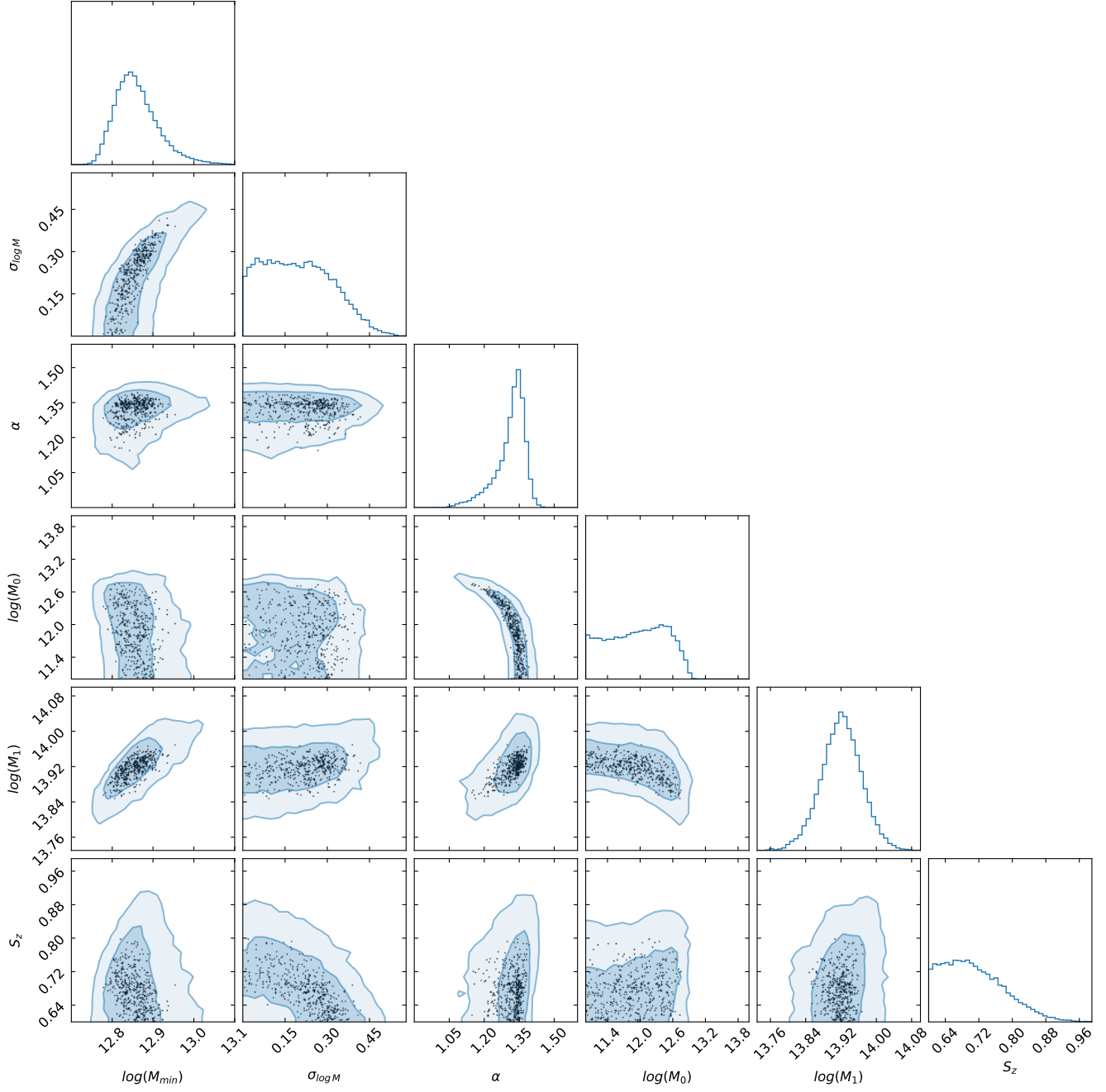
Figure 29: Points with the highest chain likelihood values selected from 500 segments in the chain for the redshift bin of $0.61 < z < 0.72$. The contours of the full MCMC chain are also shown. These points span a wide range in parameter space.

highest. We can therefore select points in the regions of highest density and they are likely to be near the likelihood peak. Below we describe the method in detail.

First we downsample the MCMC chain by selecting every 50th point from the chain to reduce the effects of correlations, and then for each point compute the distance to its 500th nearest neighbor (after downsampling). These distances should anti-correlate strongly with the local density. For the nearest neighbor search and distance calculation, the parameter space is normalized by the 16-84% percentile range along each dimension. We also perform "reflection" on $\sigma_{\log M}$ and S_z dimensions at their lower boundaries in their prior to remove the boundary effect: each point in the chain is duplicated with the same parameters except for $\sigma_{\log M}$ which adopts the value of $0 - \sigma_{\log M}$ where 0 is the lower boundary of $\sigma_{\log M}$; subsequently the same procedure is also performed for S_z, so in the end we have 4 times the original number of points.

We select the 500 points with the smallest neighbor distances. The distribution of these points are shown in Figure 30; note that these points have a much more compact distribution than those in Figure 29. For each of these points, we generate 100 HOD realizations and determine the χ^2 for each. We then compute the averaged χ^2 using the Hodges-Lehmann estimator (Hodges & Lehmann, 1963). Since there is still some scatter in the averaged χ^2, we again select the 10 points with the smallest averaged χ^2 and generate 1000 HOD realizations to get more accurate χ^2 values. The point with the smallest averaged χ^2 is selected as the set of best-fit parameters. In some redshift bins, the distributions of the 10 points are more compact than the 500 points; in other bins, the distributions are rather similar.
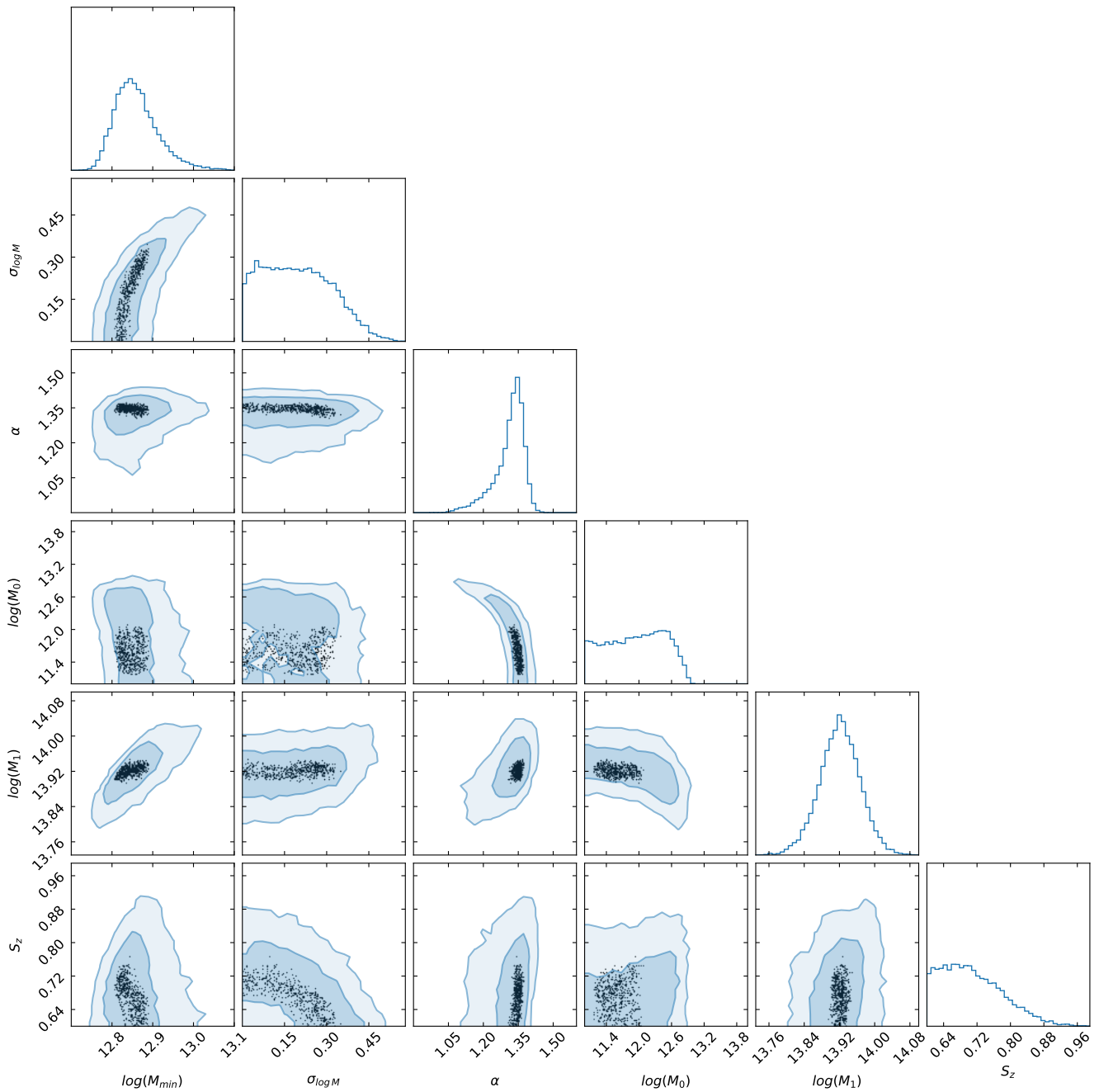
Figure 30: The distribution of 500 points that are in the highest density region in parameter space. The contours of the full MCMC chain are also shown. The distribution of these points is much more compact than the distribution of points selected directly from MCMC likelihoods which is shown in the previous plot.

BIBLIOGRAPHY

Abolfathi, B., Aguado, D. S., Aguilar, G., et al. 2018, The Astrophysical Journal Supplement Series, 235, 42

Aihara, H., Armstrong, R., Bickerton, S., et al. 2018, Publications of the Astronomical Society of Japan, 70, S8

Alam, S., Albareti, F. D., Prieto, C. A., et al. 2015, The Astrophysical Journal Supplement Series, 219, 12

Alam, S., Ata, M., Bailey, S., et al. 2017, Monthly Notices of the Royal Astronomical Society, 470, 2617

Albrecht, A., Bernstein, G., Cahn, R., et al. 2006, arXiv:astro-ph/0609591, arXiv:astro-ph/0609591

Baldry, I. K., Liske, J., Brown, M. J. I., et al. 2018, Monthly Notices of the Royal Astronomical Society, 474, 3875

Behroozi, P. S., Wechsler, R. H., & Wu, H.-Y. 2013, The Astrophysical Journal, 762, 109

Berlind, A. A., & Weinberg, D. H. 2002, The Astrophysical Journal, 575, 587

Bertin, E., & Arnouts, S. 1996, Astronomy and Astrophysics Supplement Series, 117, 393

Blake, C., Amon, A., Childress, M., et al. 2016, Monthly Notices of the Royal Astronomical Society, 462, 4240

Brammer, G. B., van Dokkum, P. G., Franx, M., et al. 2012, The Astrophysical Journal Supplement Series, 200, 13

Breiman, L. 2001, Machine Learning, 45, 5

Carbone, C., Verde, L., & Matarrese, S. 2008, The Astrophysical Journal, 684, L1

Carroll, S. M., Duvvuri, V., Trodden, M., & Turner, M. S. 2004, Physical Review D, 70, 043528

Chambers, K. C., Magnier, E. A., Metcalfe, N., et al. 2016, ArXiv e-prints

Childress, M. J., Lidman, C., Davis, T. M., et al. 2017, Monthly Notices of the Royal Astronomical Society, 472, 273

Cole, S., Percival, W. J., Peacock, J. A., et al. 2005, Monthly Notices of the Royal Astronomical Society, 362, 505

Collaboration, D., Abbott, T. M. C., Abdalla, F. B., et al. 2018a, Physical Review D, 98, arXiv:1708.01530

Collaboration, D. E. S., Abbott, T., Abdalla, F. B., et al. 2016, Monthly Notices of the Royal Astronomical Society, 460, 1270

Collaboration, T. L. D. E. S., Mandelbaum, R., Eifler, T., et al. 2018b, arXiv e-prints, arXiv:1809.01669

Colless, M., Peterson, B. A., Jackson, C., et al. 2003, arXiv:astro-ph/0306581, arXiv:astro-ph/0306581

Cooper, M. C., Aird, J. A., Coil, A. L., et al. 2011, The Astrophysical Journal Supplement Series, 193, 14

Cooper, M. C., Griffith, R. L., Newman, J. A., et al. 2012, Monthly Notices of the Royal Astronomical Society, 419, 3018

Cutri, R. M., Wright, E. L., Conrow, T., et al. 2013, Explanatory Supplement to the AllWISE Data Release Products, Tech. rep.

Dalal, N., Doré, O., Huterer, D., & Shirokov, A. 2008, Physical Review D, 77, doi:10.1103/PhysRevD.77.123514

Dawson, K. S., Schlegel, D. J., Ahn, C. P., et al. 2013, The Astronomical Journal, 145, 10

Dawson, K. S., Kneib, J.-P., Percival, W. J., et al. 2016, The Astronomical Journal, 151, 44

DESI Collaboration, Aghamousa, A., Aguilar, J., et al. 2016, arXiv:1611.00036 [astro-ph], arXiv:1611.00036

Dey, A., Schlegel, D. J., Lang, D., et al. 2019, The Astronomical Journal, 157, 168

Diemer, B. 2018, The Astrophysical Journal Supplement Series, 239, 35

Dvali, G., Gabadadze, G., & Porrati, M. 2000, Physics Letters B, 485, 208

Eisenstein, D. J., Zehavi, I., Hogg, D. W., et al. 2005, The Astrophysical Journal, 633, 560

Fitzpatrick, E. L. 1999, Publications of the Astronomical Society of the Pacific, 111, 63

Font-Ribera, A., McDonald, P., Mostek, N., et al. 2014, Journal of Cosmology and Astroparticle Physics, 2014, 023

Foreman-Mackey, D. 2016, The Journal of Open Source Software, 1, 24

Foreman-Mackey, D., Hogg, D. W., Lang, D., & Goodman, J. 2013, Publications of the Astronomical Society of the Pacific, 125, 306

Gawiser, E., van Dokkum, P. G., Herrera, D., et al. 2006, The Astrophysical Journal Supplement Series, 162, 1

Gunn, J. E., Carr, M., Rockosi, C., et al. 1998, The Astronomical Journal, 116, 3040

Hartigan, J. A., & Wong, M. A. 1979, Applied Statistics, 28, 100

Hearin, A., Campbell, D., Tollerud, E., et al. 2017, The Astronomical Journal, 154, 190

Hodges, J. L., & Lehmann, E. L. 1963, The Annals of Mathematical Statistics, 34, 598

Høg, E., Fabricius, C., Makarov, V. V., et al. 2000, 355, L27

Hudelot, P., Cuillandre, J.-C., Withington, K., et al. 2012, VizieR Online Data Catalog, 2317

Ivezic, Z., Tyson, J. A., Axelrod, T., et al. 2009, in Bulletin of the American Astronomical Society, Vol. 41, American Astronomical Society Meeting Abstracts #213, 366

Jarvis, M., Bernstein, G., & Jain, B. 2004, Monthly Notices of the Royal Astronomical Society, 352, 338

Kind, M. C., & Brunner, R. J. 2013, Monthly Notices of the Royal Astronomical Society, 432, 1483

Kitching, T. D., Heavens, A. F., Verde, L., Serra, P., & Melchiorri, A. 2008, Physical Review D, 77, doi:10.1103/PhysRevD.77.103008

Klypin, A., Yepes, G., Gottlober, S., Prada, F., & Hess, S. 2016, Monthly Notices of the Royal Astronomical Society, 457, 4340

Kochanek, C. S., Eisenstein, D. J., Cool, R. J., et al. 2012, The Astrophysical Journal Supplement Series, 200, 8

Laigle, C., McCracken, H. J., Ilbert, O., et al. 2016, The Astrophysical Journal Supplement Series, 224, 24

Landy, S. D., & Szalay, A. S. 1993, The Astrophysical Journal, 412, 64

Lang, D., Hogg, D. W., Mierle, K., Blanton, M., & Roweis, S. 2010, The Astronomical Journal, 139, 1782

Le Fevre, O., Cassata, P., Cucciati, O., et al. 2013, Astronomy & Astrophysics, 559, A14

LSST Science Collaboration, Abell, P. A., Allison, J., et al. 2009, ArXiv e-prints

Magnier, E. A., Schlafly, E. F., Finkbeiner, D. P., et al. 2016, ArXiv e-prints

Matarrese, S., & Verde, L. 2008, The Astrophysical Journal, 677, L77

Matthews, D. J., Newman, J. A., Coil, A. L., Cooper, M. C., & Gwyn, S. D. J. 2013, The Astrophysical Journal Supplement Series, 204, 21

Meisner, A. M., Lang, D., & Schlegel, D. J. 2017, The Astronomical Journal, 154, 161

Miyazaki, S., Komiyama, Y., Sekiguchi, M., et al. 2002, Publications of the Astronomical Society of Japan, 54, 833

Miyazaki, S., Komiyama, Y., Nakaya, H., et al. 2012, in SPIE Astronomical Telescopes + Instrumentation, ed. I. S. McLean, S. K. Ramsay, & H. Takami, Amsterdam, Netherlands, 84460Z

Momcheva, I. G., Brammer, G. B., van Dokkum, P. G., et al. 2016, The Astrophysical Journal Supplement Series, 225, 27

Navarro, J. F., Frenk, C. S., & White, S. D. M. 1997, The Astrophysical Journal, 490, 493

Newman, J. A., Cooper, M. C., Davis, M., et al. 2013, The Astrophysical Journal Supplement Series, 208, 5

Ouchi, M., Shimasaku, K., Okamura, S., et al. 2004, The Astrophysical Journal, 611, 660

Parkinson, D., Riemer-Sørensen, S., Blake, C., et al. 2012, Physical Review D, 86, arXiv:1210.2130

Pedregosa, F., Varoquaux, G., Gramfort, A., et al. 2011, Journal of Machine Learning Research, 12, 2825

Prakash, A., Licquia, T. C., Newman, J. A., et al. 2016, The Astrophysical Journal Supplement Series, 224, 34

Reyes, R., Mandelbaum, R., Seljak, U., et al. 2010, Nature, 464, 256

Schlafly, E. F., & Finkbeiner, D. P. 2011, The Astrophysical Journal, 737, 103

Schlegel, D. J., Finkbeiner, D. P., & Davis, M. 1998, The Astrophysical Journal, 500, 525

Scodeggio, M., Guzzo, L., Garilli, B., et al. 2018, Astronomy & Astrophysics, 609, A84

Scolnic, D., Casertano, S., Riess, A., et al. 2015, The Astrophysical Journal, 815, 117

Sinha, M., & Garrison, L. 2017, 1703.003

Skelton, R. E., Whitaker, K. E., Momcheva, I. G., et al. 2014, The Astrophysical Journal Supplement Series, 214, 24

Skrutskie, M. F., Cutri, R. M., Stiening, R., et al. 2006, The Astronomical Journal, 131, 1163

Soo, J. Y. H., Moraes, B., Joachimi, B., et al. 2018, Monthly Notices of the Royal Astronomical Society, 475, 3613

Strauss, M. A., Weinberg, D. H., Lupton, R. H., et al. 2002, The Astronomical Journal, 124, 1810

Tanaka, M., Coupon, J., Hsieh, B.-C., et al. 2018, Publications of the Astronomical Society of Japan, 70, arXiv:1704.05988

Tegmark, M., Eisenstein, D. J., Strauss, M. A., et al. 2006, Physical Review D, 74, doi:10.1103/PhysRevD.74.123507

Tinker, J. L., Robertson, B. E., Kravtsov, A. V., et al. 2010, The Astrophysical Journal, 724, 878

Wechsler, R. H., & Tinker, J. L. 2018, Annual Review of Astronomy and Astrophysics, 56, 435

White, M., Blanton, M., Bolton, A., et al. 2011, The Astrophysical Journal, 728, 126

York, D. G. 2000, The Astronomical Journal, 120, 1579

Zehavi, I., Zheng, Z., Weinberg, D. H., et al. 2011, The Astrophysical Journal, 736, 59

Zentner, A. R., Hearin, A., van den Bosch, F. C., Lange, J. U., & Villarreal, A. 2019, Monthly Notices of the Royal Astronomical Society, 485, 1196

Zhai, Z., Tinker, J. L., Hahn, C., et al. 2017, The Astrophysical Journal, 848, 76

Zheng, Z., Coil, A. L., & Zehavi, I. 2007, The Astrophysical Journal, 667, 760